

COIL FROSTING AND DEFROSTING IN INDUSTRIAL FREEZERS
OPERATING NEAR SATURATED CONDITIONS

By

PEDRO J. MAGO

A DISSERTATION PRESENTED TO THE GRADUATE SCHOOL
OF THE UNIVERSITY OF FLORIDA IN PARTIAL FULFILLMENT
OF THE REQUIREMENTS FOR THE DEGREE OF
DOCTOR OF PHILOSOPHY

UNIVERSITY OF FLORIDA

2003

This dissertation is dedicated to my wife and family.

ACKNOWLEDGMENTS

I thank my advisor Dr. Sherif for giving me the opportunity to work with him; and for all the good advice he gave me throughout my Ph.D. program. I also thank the professors on my committee for their advice and help in completing this dissertation. I express my gratitude to Randy Theen, who helped me set up the experimental facility and overcome all the problems I found in the laboratory.

I especially thank my wife for her love and understanding. She gave me all of the support that I needed to complete this big challenge in my life. I know that without her love and understanding this would not have been possible. I love her with all my heart.

I also want to thank my family, who are far away. They have always given me their love; and encourage me continue my education. I always have them in my heart.

Last but not least, I would like to thank the Universidad de Oriente, the institution in Venezuela that gave me the opportunity to increase my knowledge through this Ph.D. program.

TABLE OF CONTENTS

	<u>Page</u>
ACKNOWLEDGMENTS	iii
LIST OF TABLES	vii
LIST OF FIGURES	viii
NOMENCLATURE	xiii
ABSTRACT	xx
 CHAPTER	
1 INTRODUCTION	1
Literature Review	1
Objectives and Scope	7
2 EXPERIMENTAL FACILITIES, INSTRUMENTATION AND DATA ACQUISITION	10
Experimental Facilities	10
Instrumentation	15
Data Acquisition System	16
3 ISSUES PERTAINING TO DEMARCATION LINE IN THE FROST ZONE	18
Objectives	18
Establishing the Existence of the Demarcation Line	18
Modeling the Cooling Process Path through a Frosted Coil	25
Analysis	26
Results and Discussion	35
Conclusions	43
4 ISSUES PERTAINING TO HOT-GAS COIL DEFROSTING	45
Objectives	45
Analysis	46
Results and Discussion	51
Conclusions	64

5	ALTERNATIVE ENERGY CONSERVATION TECHNOLOGIES IN INDUSTRIAL FREEZERS OPERATING UNDER FROSTING CONDITIONS ...65	
	Objective.....65	
	Feasibility of Heat Pipes.....65	
	Heat Pipes for Dehumidification.....66	
	Calculation Software.....67	
	Analysis of the Dehumidification Process.....69	
	Analysis of the Energy Requirements.....71	
	Feasibility of Using Dampened Coils during the Defrosting Process.....72	
	Operating Freezer Coils at High Face Velocities.....83	
	Conclusions.....94	
6	FORMULATIONS OF THERMODYNAMIC PROPERTIES OF SUPERSATURATED AIR96	
	Objectives.....96	
	Properties of Supersaturated Moist Air.....97	
	Thermodynamic Properties.....100	
	Psychrometric Formulations.....109	
	Results.....113	
	Conclusions.....114	
7	HEAT AND MASS TRANSFER ON A CYLINDER SURFACE IN CROSS FLOW UNDER SUPERSATURATED FROSTING CONDITIONS120	
	Objectives.....120	
	Analysis.....122	
	Results and Discussion.....130	
	Conclusions.....137	
8	THEORY OF FROST-FORMATION MECHANISMS.....138	
	Formation Mechanism in the Subsaturated Zone.....138	
	Formation Mechanism in the Supersaturated Zone.....141	
9	SOFTWARE FOR THE DESIGN AND OPERATIONAL PHASES OF REFRIGERATED FACILITIES.....145	
	Objective.....145	
	Software for Predicting the Onset of Frost Formation.....145	
	Software for Simulating Freezer Operation.....150	
10	CONCLUSIONS154	

APPENDIX UNCERTAINTY ANALYSIS.....	157
LIST OF REFERENCES	162
BIOGRAPHICAL SKETCH	168

LIST OF TABLES

<u>Table</u>	<u>page</u>
3-1. Constants C_1 and j for a staggered arrangement (Equation 3-4) for air flow over a tube bank of 10 or more rows	28
3-2. Correction factor C_2 for a staggered arrangement as provided for in Equation 3-5	28
3-3. Geometrical data of the finned coil	36
3-4. Parameter values employed in the model	36
3-5. Heat transfer coefficients using Equations 3-6, 3-11, 3-21, and 3-27	36
3-6. Calculated cooling process path through the coil	37
3-7. Amount of cooling and percentage of the total cooling for each row	39
5-1. Defrost efficiency and melt collected in the defrosting process for different coil-face velocities	91
5-2. Fan-defrost contribution for coil-face velocities of 1.6 m/s, 3.7 m/s, and 6.5 m/s	94
5-3. Average coil performance load rate for coil-face velocities of 1.6 m/s, 3.7 m/s, and 6.5 m/s	94
6-1. Value of the virial coefficients	99
6-2. Temperature derivatives of the virial coefficients	100
6-3. Enhancement factor obtained numerically solving Equation 6-49	112
6-4. Thermodynamic properties of moist supersaturated air	115
A-1. Uncertainty of experimental measurements	158
A-2. Uncertainty of the refrigerant and water properties	158
A-3. Uncertainty of the results	158
A-4. Function and partial derivative for the calculated quantities	159

LIST OF FIGURES

<u>Figure</u>	<u>page</u>
2-1. Experimental facility used in this investigation.....	11
2-2. Schematic of the Psychrometric Freezer Room showing the test and auxiliary coils, the artificial load generator, and the location of thermocouples for temperature measurements.....	13
2-3. Photograph showing the front face of the Test Fan-Coil Unit (FCU-T).....	13
2-4. Schematic of the Test Fan-Coil Unit (FCU-T).	14
2-5. Schematic of the artificial sensible and latent load generator.....	17
3-1. Psychrometric depiction of air-cooling processes as measured inside the freezer	20
3-2. Visualization of freezer conditions during Scenario 1 as measured inside the freezer	22
3-3. Visualization of freezer conditions during Scenario 2 as measured inside the freezer	22
3-4. Visualization of freezer conditions during Scenario 3 as measured inside the freezer	23
3-5. Visualization of freezer conditions during Scenario 4 as measured inside the freezer	23
3-6. Frosted coil after severe supersaturated conditions have existed in the freezer for a while	24
3-7. Frosted coil due to sublimation of the frost after subsaturated conditions have been restored in the freezer after severe supersaturation of freezer air	25
3-8. Staggered array of a coil	27
3-9. Physical model of pipe.....	30
3-10. Representation of the actual and theoretical air paths through the dehumidifying coil	38

3-11.	Representation of the actual air-cooling path through the dehumidifying coil showing the calculated leaving air conditions from each row as well as the measured coil inlet and outlet states	39
3-12.	Percentage of the total cooling for each coil row	41
3-13.	Representation of processes on the psychrometric chart showing where the transition to a supersaturated state occurs by keeping the same entering air temperature (-8.3°C) and gradually increasing the entering air relative humidity	42
4-1.	Refrigerant temperatures at the inlet and outlet of the coil during defrosting for both Stoecker et al. (1983) and present work	53
4-2.	Mass flow rate of refrigerant during defrosting for both Stoecker et al. (1983) and present work	53
4-3.	Refrigerant pressures at the inlet and outlet of the coil during defrosting for both Stoecker et al. (1983) and present work	54
4-4.	Freezer air and coil surface temperatures during refrigeration and defrosting	56
4-5.	Coil condition after 5 hours of refrigeration under supersaturated conditions in the refrigeration mode.....	56
4-6.	Coil after 5 minutes into the defrosting process	57
4-7.	Coil after 10 minutes into the defrosting process	57
4-8.	Coil after 15 minutes into the defrosting process	58
4-9.	Freezer and coil surface temperatures during refrigeration	59
4-10.	Coil after 5 hours of operation under subsaturated conditions during the refrigeration process.....	59
4-11.	Frost surface temperature before the beginning of the defrosting process	61
4-12.	Frost surface temperature after 1 minute into defrosting.....	61
4-13.	Frost surface temperature after 3 minutes into defrosting	62
4-14.	Frost surface temperature after 8 minutes into defrosting	62
4-15.	Frost surface temperature vs. time during defrosting	63
4-16.	Frost and pipe surface temperatures vs. time during defrosting	63
5-1.	Heat pipe technology used in dehumidification processes	67

5-2.	Representation of the dehumidification process using heat pipes	68
5-3.	Main screen of the HeatpipePRO v1.0 software.....	68
5-4.	Coil and dehumidification processes with and without heat pipes	69
5-5.	Energy required for cooling and dehumidification with and without heat pipes for two different relative humidities.....	72
5-6.	Coil suction covered with plexiglass and supported by Velcro material.....	74
5-7.	Coil discharge covered with plexiglass and supported by Velcro material	74
5-8.	Coil suction being covered by plexiglass.....	75
5-9.	Coil discharge being covered by plexiglass.....	75
5-10.	Conditions of the coil at the beginning of the defrosting process.....	76
5-11.	Conditions of the coil at the beginning of the defrosting process (suction side)...	77
5-12.	Conditions of the coil at the beginning of the defrosting process (discharge side).....	78
5-13.	Conditions of the coil after 8 minutes into the defrosting process (suction side).....	78
5-14.	Conditions of the coil after 8 minutes into the defrosting process (discharge side).....	79
5-15.	Conditions of the coil after 15 minutes into the defrosting process (suction side).....	79
5-16.	Conditions of the coil after 15 minutes into the defrosting process (discharge side).....	80
5-17.	Conditions of the coil at the beginning of the defrosting process (suction side).....	80
5-18.	Conditions of the coil after 8 minutes into the defrosting process (suction side).....	81
5-19.	Conditions of the coil after 15 minutes into the defrosting process (suction side).....	81
5-20.	Defrost efficiency for the three scenarios analyzed	82
5-21.	Freezer and coil temperatures during both refrigeration and defrosting (Case a).....	84

5-22.	Freezer and coil temperatures during both refrigeration and defrosting (Case b).....	85
5-23.	Comparison of the coil condition after 5 hours of refrigeration (same as the beginning of defrosting) for different coil-face velocities.	87
5-24.	Comparison of coil condition 5 minutes into defrosting for different coil-face velocities.	88
5-25.	Comparison of coil condition 10 minutes into defrosting for different coil-face velocities.	89
5-26.	Comparison of coil condition 15 minutes into defrosting for different coil-face velocities.	90
5-27.	Defrost efficiency vs. coil-face velocity	92
6-1.	Psychrometric chart in the supersaturated zone for a temperature range from -40 to 0 °C	118
6-2.	Psychrometric chart in the supersaturated zone for a temperature range from 0 to 40 °C	118
6-3.	Psychrometric chart in the supersaturated zone for a temperature range from -40 to 0 °C, showing two sample points	119
6-4.	Psychrometric chart in the supersaturated zone for a temperature range from 0 to 40 °C, showing two sample points	119
7-1.	Small area segment on the cylinder surface in the vicinity of the angular position (θ)	123
7-2.	Flow chart of the numerical procedure used.....	129
7-3.	Effect of the time step on the stability of the solution	130
7-4.	Variation of the frost thickness with time at the stagnation point	131
7-5.	Variation of the frost thickness with time at the separation point	132
7-6.	Variation of the frost surface temperature with the angle (θ) for different times.....	133
7-7.	Variation of the frost thickness with the angle (θ) for different times:	133
7-8.	Effect of the Reynolds number on the frost thickness	134

7-9.	Variation of the frost surface temperature with time for different Reynolds numbers.....	136
7-10.	Variation of the mass of frost with time for different Reynolds numbers	137
9-1.	Main Menu of the software.....	146
9-2.	Screen to input the simulation data.....	147
9-3.	Screen showing the numerical results.....	148
9-4.	Graph menu to see the graphical results	148
9-5.	Screen showing graphical results.....	149
9-6.	Screen showing air properties.....	150
9-7.	Main Menu of the software.....	151
9-8.	Simulation data screen	152
9-9.	Some results screen of the software.....	153

NOMENCLATURE

Latin symbols

a_0 - a_7	Constants defined by Equation 6-15
A	Surface area; A_o total outside surface area including the finned surface, $A_{orifice}$ inside cross sectional area upstream of the orifice, $A_{p,i}$ total area of the inside surface of the pipe; $A_{p,o}$ total area of the outside surface of the pipe, m^2
$ACPLR$	Average coil performance load rate, kW
ADP	Apparatus dew-point, °C
b	Slope of the saturated enthalpy-temperature curve ($b = \Delta i_s / \Delta t_s$); evaluated at frost surface temperature; $b_{f,p}$ evaluated at the frost surface temperature for the part of the frost collecting on the pipe; $b_{f,m}$ evaluated at the mean frost surface temperature for the part of the frost collecting on the fin; b_R evaluated at the refrigerant temperature, kJ/(kg°C)
b_0 - b_3	Constants defined by Equation 6-24
B_{aa}	Second virial coefficient for dry air, cm^2/mol
B_{aw}	Cross virial coefficient for moist air, cm^2/mol
B_{ww}	Second virial coefficient for moist air, cm^2/mol
C_{aaa}	Third virial coefficient for dry air, cm^6/mol^2
C_{aaw}	Cross virial coefficient for moist air, cm^6/mol^2
C_{aww}	Cross virial coefficient for moist air, cm^6/mol^2
$CBPF$	Coil bypass factor, dimensionless

C_d	Discharge coefficient of the orifice meter, dimensionless
C_p	Specific heat at constant pressure, kJ/(kg K)
C_{www}	Third virial coefficient for moist air, cm ⁶ /mol ²
C_1, C_2	Constants define by Table 3-1 and Table 3-2, respectively
D_{diff}	Mass diffusion coefficient of water vapor in air, m ² /s
D	Diameter, m
DBT	Dry-bulb temperature, °C
e_0-e_5	Constants defined by Equation 6-25
f_0-f_5	Constants defined by Equation 6-25
FDC	Fan-defrost contribution, percentage
g_0-g_4	Constants defined by Equation 6-27
h_c	Convection heat transfer coefficient, $h_{c,i}$ for inside of tube, $h_{c,o}$ for outside surface, $h_{c,o,f}$ for a frosted surface, W/(m ² K)
h_{mass}	Mass transfer coefficient, kg/(m ² s)
i	Specific enthalpy, kJ/kg
\bar{i}	Molar enthalpy, kJ/kmol
i_{drop}	Enthalpy of the water suspended in the air, kJ/kg
i_F	Enthalpy of moist air in the vicinity of the fin surface; $i_{F,m}$ evaluated at mean fin temperature; $i_{F,b}$ evaluated at the fin base temperature, kJ/kg

i_s	Enthalpy of saturated moist air; $i_{s,a}$ evaluated at air temperature t_a , $i_{s,p}$ is evaluated at pipe surface temperature t_p , $i_{s,R}$ evaluated at refrigerant temperature t_R , $i_{s,f,m}$ evaluated at the mean frost surface temperature, kJ/kg
j	Constant defined in Table 3-1
j_0-j_4	Constants defined by Equation 6-29
k	Thermal conductivity, W/(m K)
$K_{orifice}$	Flow coefficient of the orifice meter, dimensionless
l_0-l_6	Constants defined by Equation 6-30
Le	Lewis number, dimensionless
L_s	Latent heat of sublimation of the frost, J/kg
\dot{m}	Mass flow rate, kg/s
\dot{m}_f	Frost deposition rate per unit area, kg/(m ² s)
m	Mass, m_{drop} mass of water suspended in the air, m_{melt} mass of the melt during the defrosting process, m_{ws} mass of saturated water vapor mixed with the air, kg
M_a	Molecular weight of dry air (28.9)
M_w	Molecular weight of water vapor (18)
n_0-n_5	Constants defined by Equation 6-31
Nu	Nusselt number, dimensionless
N_L	Number of tube rows, dimensionless
o_0-o_5	Constants defined by Equation 6-38

P	Total pressure, Pa
P_{atm}	Ambient pressure (101325 Pa)
P_s	Saturation pressure, Pa
Pr	Prandtl number, dimensionless
P_w	Partial pressure of water vapor, Pa
\dot{Q}	Heat transfer rate, $\dot{Q}_{Coil,T}$ total refrigeration load, $\dot{Q}_{def,in}$ defrosting heat input rate, \dot{Q}_{fan} fan power, \dot{Q}_{melt} rate of heat removed with the FCU-T melt, $\dot{Q}_{Room,S}$ room sensible heat rate, $\dot{Q}_{Room,T}$ room total heat rate, kW
Q	Heat transfer, $Q_{def,in}$ defrosting heat input, $Q_{def,load}$ total defrosting heat load, Q_{fan} fan heat, Q_{melt} heat removed with the FCU-T melt, Q_{net} net refrigeration load, $Q_{total,s}$ total sensible heat gain, $Q_{total,l}$ total latent heat gain, Q_{total} total refrigeration load, kJ
r_1, r_2	Internal and external radius of the fin, respectively, m
\bar{R}	Universal gas constant (8.31441 kPa m ³ /(kmol K))
Re	Reynolds number, $Re_{Df,super}$ Reynolds number for supersaturated air based on the frost diameter, dimensionless
S_L, S_T	Longitudinal and transverse pitch, respectively, m
t	Temperature, °C
T	Absolute temperature, K
u	Velocity, m/s
u_0-u_5	Constants defined by Equation 6-39
$U_{o,f}$	Overall heat transfer coefficient for a frosted finned tube coil based on an enthalpy driving force, (kW kg)/(m ² kJ)
v	Specific volume, m ³ /kg

\bar{v}	Molar volume, m ³ /kmol
\dot{V}	Volumetric flow rate, m ³ /s
∇_a	Molar volume of dry air (29.9)
∇_v	Molar volume of water vapor (18.8)
W	Humidity ratio, kg _w /kg _a
w_0 - w_6	Constants defined by Equation 6-39
X_f	Frost thickness, m
y_f	Half of fin thickness, m
z_0 - z_6	Constants defined by Equation 6-42

Greek symbols

α	Thermal diffusivity of air, m ² /s
β	Henry's Law constant, 1/Pa
ΔP	Differential pressure across the orifice meter, in inches of water column differential (inches WCD)
$\Delta \tau$	Time increment, s
ΔX_f	Increment in frost thickness, m
ε	Enhancement factor defined by Equation 6-37
ψ	Ratio of the orifice throat diameter to the pipe inside diameter, dimensionless
η	Efficiency, η_{def} defrost efficiency, η_f fin efficiency, dimensionless
λ	Length, m
μ	Dynamic viscosity, kg/(m s)
μ_t	Degree of saturation, percentage

ρ	Density, kg/m ³
τ	Time, τ_{ref} duration of the FCU-T refrigeration mode, τ_{def} duration of the FCU-T hot-gas defrosting mode, τ_{total} duration for a complete FCU-T refrigeration and defrosting cycle, s
θ	Angular position on the cylinder circumference

Subscripts

a	Air
atm	Atmospheric
av	Average
B	Fin base
def	Defrost or defrosting
F	Fin
f	Frost
$f\theta$	Frost at angular position, θ
i	Inside of tube
ice	Ice
in	Inlet
$liquid$	Liquid water
$load$	Load
m	Moist or mean
max	Maximum
o	Outside of tube
out	Outlet
P	Pipe or pipe surface

<i>p</i>	Constant pressure
<i>R</i>	Refrigerant
<i>ref</i>	Refrigeration
<i>s</i>	Saturated
<i>super</i>	Supersaturated
<i>t</i>	Total
<i>vap</i>	Vapor
<i>w</i>	Water vapor

Abstract of Dissertation Presented to the Graduate School
of the University of Florida in Partial Fulfillment of the
Requirements for the Degree of Doctor of Philosophy

COIL FROSTING AND DEFROSTING IN INDUSTRIAL FREEZERS
OPERATING NEAR SATURATED CONDITIONS

By

Pedro J. Mago

August 2003

Chair: S.A. Sherif

Major Department: Mechanical and Aerospace Engineering

Whenever moist air exists in the vicinity of a surface whose temperature is both below the dew-point temperature of water vapor in air and below the freezing point, frost will form. This frost contributes to coil heat-transfer performance degradation due to both the insulating effect of the frost layer and the resulting coil blockage. While the frosting problem has been extensively researched, no study has investigated the problem when the freezer is operating near saturated conditions. Field observations of industrial freezer operation indicate that this mode of operation is much more common than originally thought; and that the transition to supersaturated operation can easily occur if proper care is not exercised by either the refrigeration system designer or the freezer operator. Field observations also reveal that operating freezers in supersaturated conditions can significantly accelerate the occurrence of the negative aspects of frost formation vis-à-vis coil heat transfer performance. For this and other reasons, the study presented in this dissertation focused on that aspect of freezer operation with the hope of

developing tools and protocols that may help guide refrigeration-system designers and freezer operators avoid the conditions that contribute to this mode of operation; and thus help improve the performance of freezer coils that are particularly prone to the frosting problem.

CHAPTER 1 INTRODUCTION

Literature Review

Commercial freezers of the type found commonly in food distribution warehouses and supermarkets are prone to frost formation inside and around the freezer door, especially if the freezer has a high volume of traffic. The problem is the exchange of warm and cold air that takes place when the freezer door is opened to deliver or retrieve goods. Basically, cold air from the freezer rushes out along the floor of the vestibule or anteroom, while warm and humid outside air rushes inside the freezer near the ceiling. The moisture introduced into the freezer space is likely to cause the air to become supersaturated¹ at the prevailing air temperature. If that temperature is above the freezing point of water, moisture in the air would exist in the form of tiny liquid droplets suspended in the air stream—a familiar condition known as fog. If the same scenario exists, but with the air temperature below the freezing point, ice fog forms. Air-borne ice crystals that normally constitute ice fog have great affinity for cold surfaces; and thus tend to deposit on any surface they can find inside the freezer.

While frost formation on cooling coils in domestic refrigeration, air conditioning, and heat pump applications has been recognized as a problem that contributes to heat transfer coil performance degradation (Sherif 1991), the problem in industrial walk-in freezers is much more significant and potentially more expensive to deal with.

¹ In this investigation the term supersaturated air is defined as a mixture of saturated air and suspended liquid water droplets or ice crystals depending on whether the prevailing air temperature is larger or smaller than the freezing point temperature of water, respectively.

Reasons that contribute to this fact are many and include the following:

- The temperature difference between the freezer and the anteroom is larger than in air conditioning applications.
- The temperature of the freezer is significantly lower than those temperatures encountered in air conditioning and heat pump applications.
- The magnitude of potential energy waste in industrial walk-in freezers is significantly larger than the corresponding problem in either domestic refrigeration or heat pump and air conditioning applications.

The combination of the first two facts, coupled with the manner in which the saturation curve on the psychrometric chart is shaped in the low temperature region, contribute to increasing the likelihood that the freezer would operate under supersaturated conditions and that airborne ice crystals would form.

While literature dealing with the frosting problem on different geometries is abundant, our review is confined to finned coils, cylindrical geometries, and studies dealing with frost property formulations. Among the investigators who reported frost formation on cylinders are Andrichak (1962), Chung and Algren (1958a, 1958b), Padki et al. (1989), Parish and Sepsy (1972), Raju and Sherif (1993), and Sengupta et al. (1998). Chung and Algren (1958a, 1958b) reported experimental mass transfer results for cylinders in cross flow of humid air for a host of environmental and surface conditions, represented by the free stream Reynolds number, the ambient dry-bulb temperature, the humidity ratio, and the cylinder surface temperature. The results presented were in terms of the frost total mass accumulated on the cylinder as a function of time for a range of Reynolds numbers from 2592 to 9965, ambient dry-bulb temperatures of 15°C to 21.4°C,

and cylinder surface temperatures of -11.9°C to -23°C . In a similar manner, Andrichak (1962) experimentally studied the frost formation on a cylinder in cross flow for different angular positions from the stagnation point to the separation point, which was considered to be 80° for laminar flow over a cylinder. He found that the frost thickness decreases with the angular position on the cylinder. Sengupta et al. (1998) performed an experimental investigation in which the emphasis was placed on obtaining correlations for the thickness-time history and the heat transfer-time history for a cylinder in cross flow of humid air. They used a low-velocity wind tunnel comprising a rectangular test section, a transition section, and a honeycomb placed at the tunnel entrance. Humid air was forced over the coil using a suction fan located at the downstream end of the tunnel. They derived correlations in terms of nondimensional parameters representing the free-stream velocity, humidity ratio, and temperature, as well as time. They found these correlations to agree well with the experimental data. On the other hand, Parish and Sepsy (1972) and Raju and Sherif (1993) derived a transient model to predict the frosting problem over the same geometry as Andrichak (1962). They used a numerical solution for the momentum, energy, and diffusion boundary-layer equations along with the continuity equation, using a finite difference scheme. Both groups of researchers reported the variation of frost thickness with time at two specific locations on the cylinder: the stagnation point and the separation point (that was considered to be 80°C). Raju and Sherif (1993) also reported the variation of the frost surface temperature with the angular position along the circumference of the cylinder for the same range mentioned above (0°C to 80°C).

Among the investigators who studied finned coils are Chen et al. (2000a, b) Kondepudi and O'Neal (1988, 1989, 1991), and Tao et al. (1994). Kondepudi and O'Neal (1988, 1989, 1991) studied the effects of frost growth on the thermal performance of finned tube heat exchangers with triangular spine fins, with flat fins, and with louvered fins, respectively. In their results the frost accumulation, pressure drop across the coils, and energy transfer coefficient were quantified with respect to air humidity, refrigerant temperature, and fin geometry. They found that higher air humidities, lower refrigerant temperatures, and higher fin densities lead to increased frost accumulation, higher pressure drops, and higher energy transfer. They also found that the louvered fins had more frost accumulation and air-side pressure drop across the coils compared to the flat fins.

Tao et al. (1994) summarized some of the studies performed in this field and, in particular, reported on measurements for frost growth during the initial stage on the surfaces of different materials. They also reported on new numerical results of frost formation in the freezer temperature range.

Chen et al. (2000a, b) presented a numerical model for predicting frost growth on plate-fin heat exchangers. The model they presented treats the frost growth as a porous media problem that is transient and one-dimensional and includes transient, two-dimensional heat conduction in the fins. They found that, for a constant air flow rate through the heat exchanger, the blockage of air flow resulting from the frost growth increases the pressure drop across the heat exchanger by up to a factor of 8, while the heat transfer rate decreases by 20%. In another investigation, the same authors compared the numerical model results with experimental data for frost height, frost density, airflow

pressure drop through the finned section, and heat transfer rate through the cold base, finding that the simulation results and experimental data agree within the experimental uncertainty with few exceptions.

Studies emphasizing empirical or theoretical frost property formulations were reported by Biguria and Wenzel (1970), Brian et al. (1969), Hayashi et al. (1977a, 1977b), Marinyuk (1980), Yonko and Sepsy (1967), among others. Yonko and Sepsy (1967) performed an experimental investigation and proposed an empirical correlation for the frost thermal conductivity based on the frost density. Their correlation is valid for frost densities less than 573 kg/m^3 . In a similar manner, Brian et al. (1969) proposed an empirical correlation for the frost thermal conductivity as a function of the frost density and average frost temperature. His correlation was developed for a small range of frost densities (25 to 130 kg/m^3), which limited its applicability. On the other hand, Biguria and Wenzel (1970) presented equations to determine the frost density and frost thermal conductivity based on the humidity of the free stream, the velocity of the air, and the temperatures of the frost and the plate surface. Their correlation provided results for frost density and thermal conductivity with an error of $\pm 7\%$ and $\pm 25\%$, respectively. Hayashi et al. (1977a, 1977b) classified the frost-formation process into three discrete periods: crystal growth, frost layer development, and frost layer full growth. They studied the frost crystal growth, density, and thermal conductivity in each of the periods. From their studies, they proposed an empirical correlation for the frost density as a function of the frost surface temperature, for airstream velocities between 2 m/s and 6 m/s, frost surface temperature between -25°C and 0°C , and an airstream humidity ratio equal to $0.0075 \text{ kg}_w/\text{kg}_a$.

Marinyuk (1980) performed an experimental investigation from which a correlation for the frost thermal conductivity was proposed, based on frost density, frost surface temperature, and the wall temperature. His correlation was limited to frost densities up to 300 kg/m^3 .

Despite the large effort expended on investigating the problem of frost formation, very few studies looked into the formation mechanism under supersaturated conditions while accounting for psychrometric effects. Thus, it appears that any new effort to study the frosting problem should try to address the aforementioned aspect of the issue.

While there is a significant amount of information pertaining to coil frosting, studies dealing with coil defrosting are relatively few. Among the investigators who examined defrosting of freezer coils are Coley (1983), Kerschbaumer (1971), Niederer (1976), and Stoecker et al. (1983). Kerschbaumer (1971) defined the defrost efficiency as the ratio of the total heat required to melt the frost alone to the total amount of defrost heat input. Niederer (1976) attempted to determine the amount of heat required for defrost by measuring the amount of hot-gas condensing and the power input during the defrost cycle. He found that only 15 to 25% of the total heat went to melt the frost. He observed that the remaining 75 to 85% of the heat went to heat the surrounding environment and the coil surfaces. Stoecker et al. (1983) performed a study to analyze hot-gas defrosting of coils in industrial refrigeration systems. Coley (1983) suggested that during a defrost cycle in freezers, at least 15% of the frost sublimates into the surrounding refrigerated air space. He noted that this represented an additional amount of load to be subsequently removed during the refrigeration portion of the refrigeration/defrost (R/D) cycle.

While there is a reasonable amount of interest in coil defrosting studies, it is obvious that there are areas that can benefit from additional research. For example, there seems to be no quantitative information on the performance of freezer coils at low temperatures during the defrosting process near saturated freezer air conditions. Developing a reliable and extensive body of data for those types of scenarios should therefore prove a worthy cause.

Objectives and Scope

The main objective of this investigation is to develop tools and protocols that may help refrigeration system designers and freezer operators minimize the negative impact of the coil frosting problem in industrial refrigeration applications. Since the frosting problem has been extensively researched, our emphasis was on freezer operation near saturated conditions (a mode of operation that has never been studied before in the freezer temperature range). To achieve this objective, the following milestones had to be accomplished:

- Establish if there is a demarcation line between the type of frost that forms under subsaturated conditions, and the type that forms under supersaturated conditions. Once the existence of the demarcation line was established, its location was determined. This is important since we need to know where the transition from one condition to the other occurs since the nature of frost forming under both modes is different as suggested by field observations.
- Investigate the issues pertaining to the coil defrosting process using the hot-gas refrigerant method. This method of defrosting was selected because it is the most widely used defrosting technique in industrial freezers. This part of our study included both physical and infrared analysis of a coil being defrosted. The infrared

portion of the analysis provided the spatial and temporal distributions of temperature on the coil surface, a key variable in understanding the defrosting dynamics. Throughout this study, we also attempted to compare the performance of the defrosted coil with the performance of similar coils operating under subsaturated conditions.

- Study alternative energy conservation technologies in industrial freezers that are prone to coil frosting problems. The feasibility of three distinct technologies was explored both experimentally and analytically. These techniques are: the use of heat-pipe assisted heat exchangers, use of damped coils, and operating freezer coils at high coil-face velocities. These technologies were selected while pursuing the experimental investigation described in this dissertation. Their selection was primarily based on observations made while exploring how freezer coils perform near saturated conditions. While these techniques were not initially identified as potentially beneficial technologies, experimental observations suggested a potential benefit, and hence it was decided to explore their merit.
- Demonstrate the development and use of a calculation procedure for coil surfaces exposed to supersaturated air. While every effort should be made to avoid this mode of operation, it may be advantageous to develop a computational capability to predict frost formation and heat transfer rates on such a coil. For demonstration purposes, a cylinder in humid air cross flow was used. The cylinder surface was selected because it could represent the tube in a freezer coil. While this is not identical to a finned-tube freezer coil per se, it shows how the techniques developed in this study can be used to predict the performance of a real freezer coil in the supersaturated zone of the psychrometric chart. This geometry has also been selected so that results of the

supersaturated model could be compared to other published works in the subsaturated zone of the psychrometric chart. To do this, psychrometric formulations and thermodynamic properties for supersaturated air were developed. Achieving this objective could potentially break new ground in the area of coil frosting as the lack of psychrometric data in the supersaturated zone of the psychrometric chart has historically prevented such a capability from being developed. These properties will expand the available psychrometric data as well as allow us to develop new psychrometric charts incorporating moist air properties in the supersaturated zone.

- The final objective is geared toward practicing refrigeration engineers and freezer operators. The intent here is to develop two pieces of software that can be used in the design and operational phases of refrigerated facilities. The first piece of software was based on the analytical model described in the previous objective. This software was used to determine the frost-formation and heat-transfer rates on a cylinder surface under forced convection. It is important to point out that although the results obtained using the software are for a cylinder, they are a good first approximation for tubes in a freezer coil. This software will perform analysis under both subsaturated and supersaturated freezer conditions. The other piece of software can be used as a tool to prevent freezers from operating under supersaturated conditions. This would allow operators to modify any parameter in the system to avoid operating the freezer in the supersaturated zone.

CHAPTER 2 EXPERIMENTAL FACILITIES, INSTRUMENTATION AND DATA ACQUISITION

Experimental Facilities

The experimental facility utilized in this investigation is shown in Figure 2-1. A schematic of the psychrometric freezer room is shown in Figure 2-2. The figure shows a laboratory-size freezer with an industrial-size freezer coil (having four fins per inch) located at the center; and a water-vapor generator (WVG) facing the coil. Each of the freezer doors has good rubber seals to protect the freezer and the test results from the effect of air infiltration. The heat transfer rate of the test enclosure was determined experimentally while it was clean, dry, and empty.

The finned-tube freezer coil is a liquid overfeed recirculating evaporator with an overfeed ratio of three. This coil has a refrigerating capacity of about 2 tons at a coil suction temperature of -40°C and is part of a complete refrigeration system discussed in detail by Al-Mutawa et al. (1998a, b, c). A photograph of the coil front surface is shown in Figure 2-3, while coil details are provided in Figure 2-4. The coil finned tubes are arranged in eight rows in the direction of airflow and in a staggered pattern of 38 mm x 33 mm, where the tube material is copper having 15.9 mm outside diameter and 0.46 mm thickness. The fins are made of aluminum and have a flat pattern with flat edges. The fins have a thickness of 0.25 mm; and their spacing is four fins per inch. The coil has a finned height of 533 mm and a finned length of 737 mm; its outside dimensions are 1016 mm L x 610 mm W x 627 mm H.



Figure 2-1. Experimental facility used in this investigation

The hot-gas defrosting method is used with this coil when the coil is operating in the defrosting mode. The finned-tube freezer coil is classified as a draw-through unit since the fan draws the air against the refrigerant in a crossflow direction where each fluid flows at right angle to the other. However, the tubes are circuiting such that the two fluids will approach in a counterflow-type heat-exchanger arrangement. The freezer coil is employed with one fan which has a diameter of 508 mm and a speed of 18 rev/s (1075 rpm) and is operated by a 186-W motor. The unit has a face area of 0.39 m^2 and a capability to change the coil face velocity from 1.02 m/s to 7.62 m/s. The fan material is aluminum, while its hub is steel. The full-load amperage (FLA) of the fan motor is 1.7 Amps, while the maximum circuit amperage capacity of the motor is 15 Amps. A

demand defrost system was used to measure the frost thickness. This system consists of a commercial frost detector head to accommodate 15.9 mm OD tubes; and a defrost control unit switch. The detector head is a U-shaped infrared sensor with optics on the inside of the open end. An infrared light beam crosses the open end of the sensor to detect the frost thickness. The detector head is mounted vertically on a front freezer-coil tube after cutting a portion of the coil fins (Figure 2-3). The detector head is employed with an adjusting screw to set the head to the desired frost thickness. The detector senses the thickness of 0.78 mm when the adjusting screw is turned all the way in, and senses the thickness of 9.5 mm when the adjusting screw is turned all the way out. For the other frost thickness ranging from 0.78 mm to 9.5 mm, the detector's operating manual provides a table showing the number of adjusting screw turns needed for each thickness. The defrost control unit switch is enclosed in a junction box and mounted on the outside of the freezer, where it is connected to the detector head through a 4.5 m polarized plug cable. The unit switch is a normally-opened contact that closes when the frost build-up on the detector head reaches the desired adjusted frost thickness, at which point the infrared light beam is interrupted by the frost build-up. The closing of the unit switch causes a small red light located on the junction box to signal the beam crossing (i.e., the desired frost thickness); and also sends a 5-Volt DC analog signal to the computer used in this investigation.

The artificial load generation system is probably one of the most critical systems in the experimental program (Figure 2-5). It was designed to provide the freezer with the required latent heat load in order to be able to manipulate the moisture content inside the freezer during the testing period.

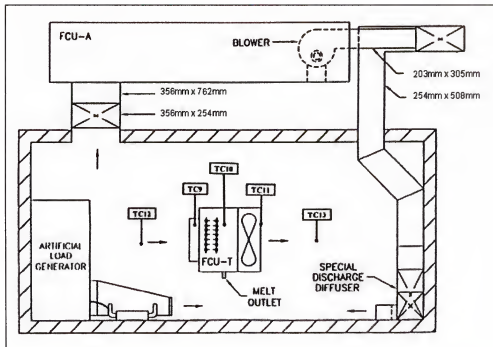


Figure 2-2. Schematic of the Psychometric Freezer Room showing the test and auxiliary coils, the artificial load generator, and the location of thermocouples for temperature measurements

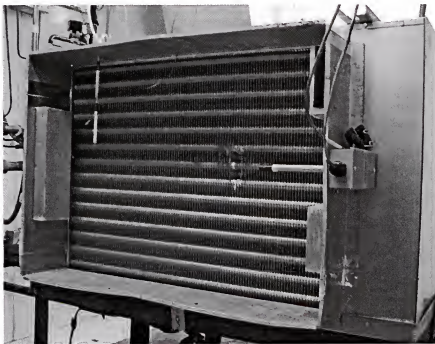


Figure 2-3. Photograph showing the front face of the Test Fan-Coil Unit (FCU-T)

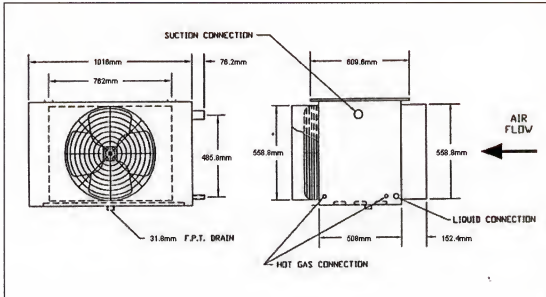


Figure 2-4. Schematic of the Test Fan-Coil Unit (FCU-T).

This latent heat load is generated by the water-vapor generator (WVG) located outside the freezer. City water is allowed to flow into the WVG through an electronic diaphragm metering pump in order to control the mass flow rate of the steam to be injected inside the freezer. The metering pump capacity ranges from 0.011 to 1.1 mm/s (maximum capacity per day is 0.091 m³). The pump's maximum injection pressure is 758 kPa. This metering pump has an adjustable speed, which ranges from 5 to 100 strokes per minute, while it also has an adjustable stroke length that ranges from 0 to 100%. The metering pump can be operated manually and by a computer.

The WVG is a liquid-injection type water-vapor generator equipped with three heating elements strapped to its side and bottom. The vaporizer is insulated with 25.4 mm thick high-temperature insulation enclosed in a galvanized steel housing. The WVG is also equipped with a thermometer, a thermostat, and a pressure-relief valve. The bimetal dial thermometer is accurate to within 0.5°C and has a reading range of 10°C to 288°C. The thermostat adjusting screw was used to obtain the desired set point. The

pressure relief valve has a cracking pressure range of 0 to 138 kPa. The cracking pressure can be adjusted to the desired set point using the valve's adjustment screw. The water injected into the WVG is heated to the desired temperature inside the vaporizer and is allowed to leave the WVG as steam through a copper tube that passes through the freezer wall to the steam outlet inside the artificial load generator. To prevent steam from freezing inside the copper tube, an electric heating cable is wrapped around the copper tube inside the freezer. The copper tube and the heating cable are both covered by a 19 mm thick Armaflex insulation. A clean-up strip heater of 150-W is also attached to the bottom of the steam outlet in order to prevent the steam from freezing at the outlet that will then stop the flow of steam to the freezer. The artificial load generation system uses direct-drive blower which distributes the steam inside the freezer. The blower has a capacity of $0.73 \text{ m}^3/\text{s}$ at 0.025 m static pressure when its motor is operating at a speed of 17.5 rev/s (1050 rpm).

Instrumentation

Temperatures have been measured at twenty locations using copper-constantan (type-T) thermocouples having an uncertainty of $\pm 0.2^\circ\text{C}$. This type is suitable for low temperature applications as well as up to 370°C . All thermocouples have been calibrated using a constant-temperature water bath (model Polyscience-80). Locations of some of the thermocouples used are shown in Figure 2-2. Temperature measurement using thermocouple TC9 is identified as coil entering air temperature, while temperature measurement using thermocouple TC10 is identified as coil leaving air temperature. Infrared images were recorded employing a Thermacam PM 695, manufactured by FLIR

systems. This camera can make accurate non-contact measurements from -40°C to 2000°C with an uncertainty of $\pm 2^{\circ}\text{C}$.

The relative humidity (RH) of the air inside the freezer was measured both upstream and downstream of the test coil. Relative humidity was measured using two Mamac humidity transducers (HU-224) connected to a remote probe hung inside the freezer. The two transducers have a humidity range of 0 to 100% and are accurate to $\pm 2\%$ of the full-scale. They use a DC power supply of 12 to 28 Volts to operate, sending output signals of 4-20 mA.

The differential pressure of the air across the coil was measured using a low-pressure transducer (Mamac-PR-274) with two static pressure probes (Mamac-A-520). Both of the 203-mm-long aluminum probes have two orifices opposing each other on a vertical position. Each probe is attached to a 50.8 mm OD flange (used to mount the probe on the coil sheet metal frame) by drilling a 6.4 mm hole on the latter and inserting the probe into that hole. The probes are inserted at right angles to the airflow, but with the orifices parallel to the airflow so that static (not stagnation) pressure is recorded. Each probe is connected to the low-pressure transducer by a 6.4 mm OD copper pilot line having PVC end connections. The probes are capable of operating under a maximum pressure of 69 kPa and a maximum temperature of 121°C .

Data Acquisition System

All measurements were recorded using a computer equipped with a state-of-the-art data acquisition system. The data-acquisition software called LabVIEW for Windows was used in this project. This software is a graphical programming language that has been widely adopted throughout industry, academia and research labs as the standard for

data acquisition and instrumentation control. Figure 2-6 shows the screen used to monitor the data during the experiments.

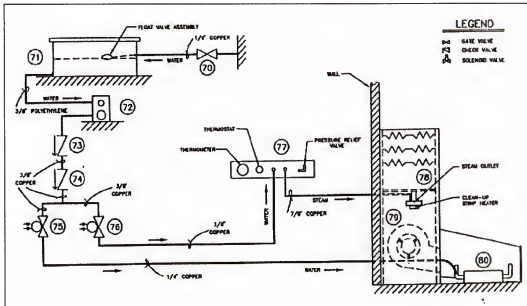


Figure 2-5. Schematic of the artificial sensible and latent load generator

ON

Temperatures (°C), Pressure (kPa), Sensible heat (kW)

TC1: FCU-T melt line upstream of the valve	<input type="text"/>	TC11: FCU-T blower outlet	<input type="text"/>
TC2: FCU-T melt line downstream of the valve	<input type="text"/>	TC12: Upstream of the FCU-T coil	<input type="text"/>
TC3: FCU-T wet return/hot-gas line	<input type="text"/>	TC13: Downstream of the FCU-T blower	<input type="text"/>
TC4: FCU-T pan hot-gas inlet line	<input type="text"/>	TC14: Inside the freezer next to the right wall	<input type="text"/>
TC5: FCU-T pan hot-gas outlet line	<input type="text"/>	TC15: Inside the freezer next to the front wall	<input type="text"/>
TC6: FCU-T refrigerant liquid/defrost refrigerant line	<input type="text"/>	TC16: FCU-A melt line upstream of the valve	<input type="text"/>
TC7: FCU-T wet return/hot-gas line	<input type="text"/>	TC17: FCU-A melt line downstream of the valve	<input type="text"/>
TC8: FCU-T refrigerant liquid/defrost refrigerant line	<input type="text"/>	TC18: FCU-A refrigerant liquid line	<input type="text"/>
TC9: FCU-T coil entrance	<input type="text"/>	TC19: FCU-A wet return line	<input type="text"/>
TC10: FCU-T coil exit	<input type="text"/>	TC20: Outside the psychrometric freezer room	<input type="text"/>

P1: Defrost refrigerant line downstream of the O/M	<input type="text"/>	P5: Main liquid line downstream of the liquid pump	<input type="text"/>
P2: FCU-T wet return/hot-gas line	<input type="text"/>	P6: Main suction line upstream of the LCU PRV	<input type="text"/>
P3: FCU-T refrigerant liquid/defrost refrigerant line	<input type="text"/>	P7: Main suction line downstream of the LCU PRV	<input type="text"/>
P4: FCU-T pan hot-gas inlet line upstream of the O/M	<input type="text"/>	P8: Main liquid line downstream of the main LSV	<input type="text"/>

Sensible heat

Figure 2-6. Screen for monitoring the data during the experiment

CHAPTER 3

ISSUES PERTAINING TO DEMARCATION LINE IN THE FROST ZONE

Objectives

One of the objectives of our study was to experimentally investigate frost formation on freezer coils under supersaturated conditions; and to relate the findings to psychrometric theory. The object was to determine if there is a demarcation line between the type of frost that forms under subsaturated conditions and the frost that forms under supersaturated conditions. Other objectives included providing a critical evaluation of the current state of knowledge of the frosting problem in general; and discussing the differences and similarities as they pertain to freezer entryways in particular. Frost formation in freezer entryways usually occurs under supersaturated conditions because of peculiar infiltration and air cooling processes (discussed later). Thus we analyzed the frost formation under both subsaturated and supersaturated conditions. In cases where the current state of knowledge is sketchy, an attempt was made to hypothesize the phenomenon in question. The hypotheses presented in this dissertation were partially based on preliminary results of this experimental investigation.

Establishing the Existence of the Demarcation Line

As mentioned above, one of the objectives of this experimental program was to demonstrate the existence of a demarcation line between the frost that forms under subsaturated conditions to that that forms under supersaturated conditions. This was achieved by starting with a predetermined coil entering air temperature, a predetermined room (freezer) sensible heat ratio (*SHR*), and a predetermined coil surface temperature,

and then steadily decreasing the coil sensible heat ratio until the cooling process line has crossed the saturation curve on the psychrometric chart into the supersaturated zone. Decreasing the coil sensible heat ratio was achieved by injecting known amounts of steam into the freezer while keeping the coil entering air temperature, and the coil surface temperature constant. In this experiment, steam injection was conducted at a rate of 1.5 kg/h. This resulted in increasing the relative humidity of the air inside the freezer (decreasing the coil sensible heat ratio), while keeping constant the coil entering air temperature at -8.3°C . Freezer temperature and sensible heat ratio were controlled by either adding an artificial sensible load to the freezer or by increasing the cooling rate inside the freezer employing the refrigeration system (without changing the coil surface temperature). The starting relative humidity of the coil entering air was 64%, while the coil surface temperature was kept constant at -18.3°C . As steam injection continued, the relative humidity of the coil entering air was increased until it reached 99%. Four different scenarios were tried employing the same entering air temperature, and coil surface temperature (see Figure 3-1).

In Scenario 1, the inlet dry-bulb temperature (DBT) was kept at -8.3°C and the inlet relative humidity (RH) was 64%, while the leaving air DBT was -16.2°C and the leaving air RH was 92%. The degree of saturation (μ_d) for this scenario was 91.9%. In Scenario 2, the inlet DBT was -8.3°C and the RH was 84%, while the leaving DBT was -16.2°C and the degree of saturation ($\mu_{d,super}$) was 102%. In Scenario 3, the inlet DBT was -8.3°C and RH 92%, while the leaving DBT was -16.1°C and $\mu_{d,super}$ was 105%. In Scenario 4, the inlet DBT was -8.3°C and RH was 99%, while the outlet DBT was

-16.1°C and $\mu_{d,super}$ was 109%. It is important to observe that the relative humidity is not defined in the supersaturated zone of the psychrometric chart. An alternative term that is equally representative of the amount of moisture present in the air in that zone is the degree of saturation ($\mu_{d,super}$). This is the ratio between the supersaturated humidity ratio (W_{super}) and the saturated humidity ratio (W_s) at the prevailing dry-bulb temperature.

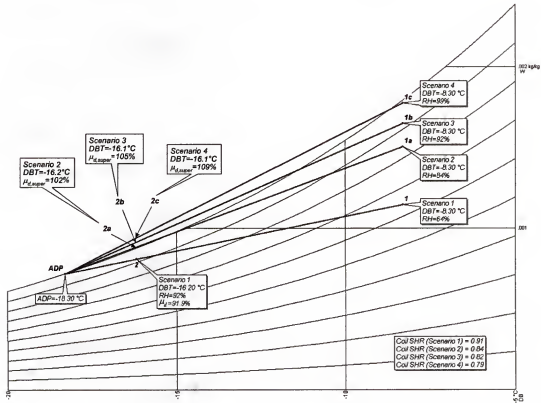


Figure 3-1. Psychrometric depiction of air-cooling processes as measured inside the freezer

While psychrometric depictions of all four processes are shown in Figure 3-1, actual freezer conditions corresponding to the four scenarios in question are shown in Figures 3-2 through 3-5, respectively. For Scenario 1, where the cooling process line (Line 1-ADP) is completely located in the subsaturated zone, clear conditions (no fog) can be observed inside the freezer. For Scenario 2, where a small part of the cooling

process line (Line *1a-ADP*) is located in the supersaturated zone on the psychrometric chart, a slight amount of fog can be detected (Figure 3-3). For Scenario 3, where a bigger portion of the cooling process line (Line *1b-ADP*) is located in the supersaturated zone, a significant amount of fog can be detected in the freezer (Figure 3-4). Finally, for Scenario 4, where the cooling process line (Line *1c-ADP*) is fully located in the supersaturated zone, fog inside the freezer is so heavy that visibility is impaired (Figure 3-5).

A close examination of the nature of frost forming under the aforementioned scenarios reveals an interesting phenomenon. Frost forming under subsaturated conditions was found to be more fluffy and dryer than that which deposited under supersaturated conditions. Frost forming under subsaturated conditions originated as a result of a transformation of the water vapor in air from a vapor phase to a solid phase bypassing the liquid phase. It is a diffusion-dominated phenomenon. Frost forming under severe supersaturated conditions continued until the coil was completely clogged (Figure 3-6). Frost formation under those conditions is thought to be a combination of two processes: a deposition process (dominated by convection) in which air-borne ice crystals deposit on the freezer coil surface, and a diffusion-dominated process similar to the one observed under subsaturated conditions. The wetter and denser nature of this type of frost is partly due to the fact that frozen water droplets (or ice crystals) exhibit wetter and denser characteristics than the more traditional frost. Frost forming under these conditions is thought to be more snow-like and is not as favorable from a heat transfer performance standpoint.

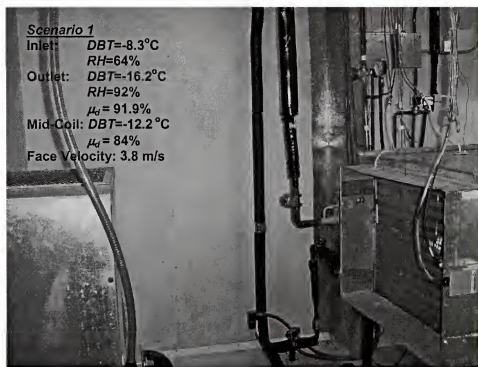


Figure 3-2. Visualization of freezer conditions during Scenario 1 as measured inside the freezer

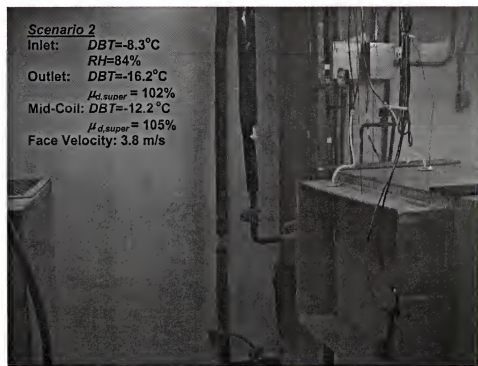


Figure 3-3. Visualization of freezer conditions during Scenario 2 as measured inside the freezer

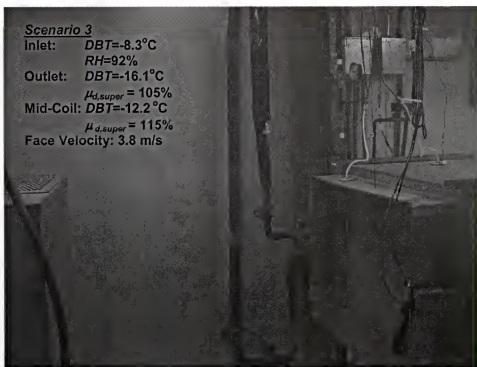


Figure 3-4. Visualization of freezer conditions during Scenario 3 as measured inside the freezer

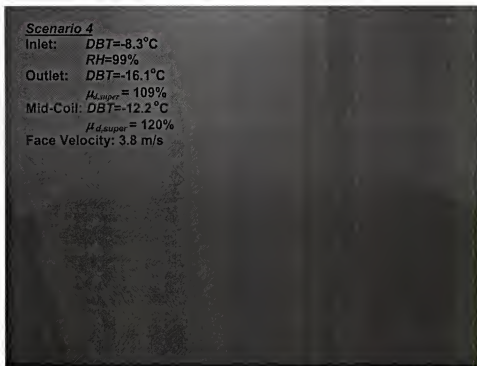


Figure 3-5. Visualization of freezer conditions during Scenario 4 as measured inside the freezer

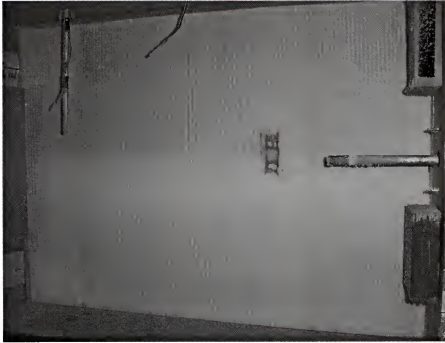


Figure 3-6. Frosted coil after severe supersaturated conditions have existed in the freezer for a while

In order to demonstrate the significance of the existence of supersaturated conditions during the deposition process, both steam injection and the refrigeration process were abruptly stopped after the coil has been completely blocked. Freezer air was shortly restored to subsaturated conditions and, after a relatively short time period, the coil started to become unclogged again (Figure 3-7). What was actually happening was that the frost on the coil was beginning a sublimation process (transformation from solid to vapor bypassing the liquid phase).

This was primarily a reflection of the fact that the vapor pressure of the air in the vicinity of the frost surface was getting higher than that in the bulk freezer air. Sublimation is a diffusion-dominated phenomenon not unlike the transformation of water vapor to frost. Keeping freezer air subsaturated is essential if frequent defrosting of coils is to be avoided. Based on the above, a frost formation theory will be articulated for the

formation mechanisms in both the subsaturated and the supersaturated zones. This will be introduced after a model that describes the cooling process through a frosted coil has been developed.

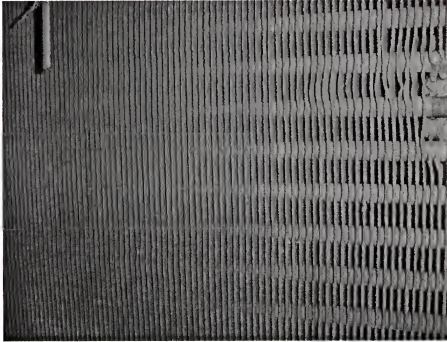


Figure 3-7. Frosted coil due to sublimation of the frost after subsaturated conditions have been restored in the freezer after severe supersaturation of freezer air

Modeling the Cooling Process Path through a Frosted Coil

In our continuing effort to provide more insight into the frost-formation mechanism and how it relates to the prevailing psychrometric conditions, we will attempt to calculate the path on an actual industrial-size finned-tube, multi-row freezer coil. This will be done employing basic heat and mass transfer principles. The model will then be validated employing measured data on the same coil. Development of a systematic mechanism for calculating the cooling process path on a finned freezer coil will prove very significant towards enhancing our understanding of the frost-formation process and its relationship to the psychrometric theory of moist air. Determining the actual

conditions leaving a given row in a multi-row freezer coil is a crucial step in identifying the coil location in the vicinity of which the transformation from subsaturated conditions to supersaturated conditions occurs. This is a key step in identifying a demarcation line between the unfavorable snow-like frost and the more traditional (and more favorable) frost-formation patterns. Thus, the objective of this effort is to calculate the air path on an actual industrial-size finned-tube, multi-row coil utilizing experimentally derived data and correlate the shape of the path with the prevailing psychrometric conditions in the freezer in the hope of identifying the demarcation line in question.

Analysis

The primary purpose of the analysis described in this section is calculating the shape of the cooling process line as the air passes through a finned-tube, multi-row dehumidifying coil under frosting conditions. In order to achieve this goal, the slope of the enthalpy-humidity ratio curve on the psychrometric chart must be determined. In order to calculate this slope, several other quantities such as the overall heat transfer coefficient and the frost-air interface temperature have to first be computed. These quantities are determined according to what follows.

External heat transfer coefficient. To determine the external heat transfer coefficient a staggered array is considered as shown in Figure 3-8. For this configuration, the maximum velocity may occur at either the transverse plane (A_1) or the diagonal plane (A_2) of Figure 3-8. Here we use the diameter of the frosted tube (D_f) instead of the outside tube diameter. The maximum velocity occurs at the diagonal plane A_2 if $S_D < 0.5(S_T + D_f)$.

In this case, the maximum velocity is given by

$$u_{\max} = \frac{S_r}{2(S_D - D_f)} u_a \quad (3-1)$$

If the maximum velocity occurs at the transverse plane A_1 , it can be expressed as

$$u_{\max} = \frac{S_r}{S_r - D_f} u_a \quad (3-2)$$

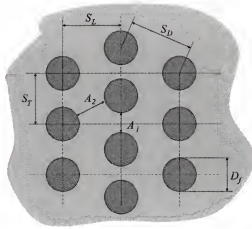


Figure 3-8. Staggered array of a coil

The Reynolds number based on the fluid velocity occurring within the tube bank is given by

$$Re_o = \frac{u_{\max} D_f}{\nu_a} \quad (3-3)$$

The Nusselt number for a tube bank composed of 10 or more rows ($N_L \geq 10$) can be determined using the correlation proposed by Grimson (1937)

$$Nu_o = 1.13 C_1 Re_o^j Pr_a^{1/3} \quad (3-4)$$

$$\left[\begin{array}{l} N_L \geq 10 \\ 2000 < Re_o < 40000 \\ Pr_a > 0.7 \end{array} \right]$$

If the number of rows (N_L) is less than 10 a correction factor may be applied such that

$$Nu_o|_{(N_L < 10)} = C_2 Nu_o|_{(N_L > 10)} \quad (3-5)$$

where C_1 and j are listed in Table 3-1 while C_2 is listed in Table 3-2.

Table 3-1. Constants C_1 and j for a staggered arrangement (Equation 3-4) for air flow over a tube bank of 10 or more rows.

S_L/D_f	$S_T/D_f = 1.25$		$S_T/D_f = 1.50$		$S_T/D_f = 2.00$		$S_T/D_f = 3.00$	
	C_1	j	C_1	j	C_1	j	C_1	j
0.60	-	-	-	-	-	-	0.213	0.636
0.90	-	-	-	-	0.446	0.571	0.401	0.581
1.00	-	-	0.497	0.558	-	-	-	-
1.25	0.518	0.556	0.505	0.554	0.519	0.556	0.552	0.562
1.50	0.451	0.568	0.460	0.562	0.452	0.568	0.488	0.568
2.00	0.404	0.572	0.416	0.568	0.482	0.556	0.449	0.570
3.00	0.310	0.592	0.356	0.580	0.440	0.562	0.428	0.574

Table 3-2. Correction factor C_2 for a staggered arrangement as provided for in Equation 3-5.

Number of rows (N_L)	Correction factor (C_2)
1	0.68
2	0.75
3	0.83
4	0.89
5	0.92
6	0.95
7	0.97
8	0.98
9	0.99

The external heat transfer coefficient is then expressed by

$$h_{c,o} = Nu_o \frac{k_a}{D_f} \quad (3-6)$$

Internal heat transfer coefficient. The properties are evaluated at the mean refrigerant temperature between the tube inlet and outlet $T_{R,m} = (T_{R,i} + T_{R,o})/2$

The Reynolds number for a flow in a circular tube is given by

$$Re_i = \frac{\rho_R u_{m,i} D_i}{\mu_R} \quad (3-7)$$

where $u_{m,i}$ is the mean velocity inside the tube and D_i is the inside tube diameter. The mean velocity is defined by

$$u_{m,i} = \frac{\dot{m}_R}{\rho_R A_c} \quad (3-8)$$

where A_c is the cross-sectional area of the tube and \dot{m}_R is the mass flow rate. The Reynolds number can be reduced to

$$Re_i = \frac{4\dot{m}_R}{\pi D_i \mu_R} \quad (3-9)$$

For turbulent flow, the Nusselt number can be calculated using the Dittus-Boelter correlation (1930)

$$Nu_i = 0.023 Re_i^{0.8} Pr_R^{0.4} \quad (3-10)$$

The internal heat transfer coefficient is then given by

$$h_{c,i} = Nu_i \frac{k_R}{D_i} \quad (3-11)$$

Frost surface temperature. Referring to Figure 3-9, the heat transfer rate can be expressed by

$$\dot{Q} = h_{c,o} (\pi D_f \lambda (T_a - T_f)) \quad (3-12)$$

as well as by

$$\dot{Q} = \frac{2\pi k_f \lambda (T_f - T_p)}{\text{Log}_e(D_f/D_o)} \quad (3-13)$$

which if combined can give the following expression for the frost surface temperature:

$$T_f = \frac{h_{c,o} D_f \text{Log}_e(D_f/D_o) T_a + 2k_f T_p}{h_{c,o} D_f \text{Log}_e(D_f/D_o) + 2k_f} \quad (3-14)$$

where k_f is the thermal conductivity of the frost in W/(m K).

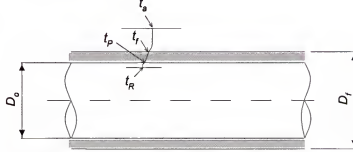


Figure 3-9. Physical model of pipe

Several empirical and theoretical correlations, relating the frost thermal conductivity and density to the frost surface temperature, exist. In this analysis, the correlation by Yonko and Sepsy (1967) will be used to calculate the frost thermal conductivity, while that by Hayashi et al. (1977a,b) will be used to compute the frost density. This gives the following equations, respectively:

$$k_f = 0.024248 + 0.00072311\rho_f + 0.000001183\rho_f^2 \quad (3-15)$$

$$\rho_f = 650 \exp(0.227t_f) \quad (3-16)$$

Equation 3-16 is valid for a frost surface temperature in the range $-25^\circ\text{C} < t_f < 0^\circ\text{C}$ and for an air stream velocity between 2 and 6 m/s. In this analysis, the temperature of the frost is calculated twice for the purpose of calculating the overall heat transfer coefficient, one time at the entrance and another time at the exit of the coil.

Overall heat transfer coefficient for a frosted finned-tube coil. In this section we will determine the overall heat transfer coefficient for the case when the fins and tubes are frosted. To achieve this we assume that the thermal resistance of the tube is

negligible, that the tube mean-surface temperature is t_p , and that the refrigerant mean temperature is t_R . It will also be assumed that a thin layer of frost having an average thickness equal to X_f covers the fins and tubes. The local rate of heat transfer inside the tube can be written as

$$\dot{Q} = h_{c,d} A_{p,d} (t_p - t_R) \quad (3-17)$$

The enthalpy of saturated moist air can, in general, be expressed as $i_s = a + bt_s$ for a small temperature range, such as 5°C. The term b is the slope of the saturated enthalpy-temperature curve (i.e., $b = \Delta i_s / \Delta t_s$). Thus, a quantity b'_R can be defined according to the equation

$$b'_R = \frac{i_{s,p} - i_{s,R}}{t_p - t_R} \quad (3-18)$$

In Equation 3-18, the subscripts P and R indicate conditions pertaining to the pipe surface and refrigerant mean temperatures, respectively.

From Equations 3-17 and 3-18 we get

$$\dot{Q} = h_{c,d} A_{p,d} \frac{(i_{s,p} - i_{s,R})}{b'_R} \quad (3-19)$$

The rate of heat transfer from the tube and fins to the air can be expressed by

$$\dot{Q} = \frac{h_{c,o,f}}{b_{f,p}} A_{p,o} (i - i_{s,p}) + \frac{h_{c,o,f}}{b_{f,m}} A_F (i - i_{F,m}) \quad (3-20)$$

where $b_{f,p}$ and $b_{f,m}$ are the slopes of the saturated enthalpy-temperature curve evaluated at the frost temperature on the tube surface and on the fin, respectively. Both of these quantities can be evaluated employing moist air tables. The quantity $i_{F,m}$ is the enthalpy

of saturated air at the mean fin temperature. The term $h_{o,f}$ is the external heat transfer coefficient for a frosted surface and is given by

$$h_{c,o,f} = \frac{1}{\left(\frac{C_{p,a}}{b_f h_{c,o}} \right) + \left(\frac{X_f}{k_f} \right)} \quad (3-21)$$

where k_f is calculated by Equation 3-15.

The overall heat transfer coefficient can be expressed in terms of the fin efficiency. The efficiency of a frosted fin is defined as

$$\eta_F = \frac{i - i_{F,m}}{i - i_{F,B}} \quad (3-22)$$

where $i_{F,m}$ and $i_{F,B}$ are the enthalpies of saturated air evaluated at the mean fin temperature and fin base temperature, respectively.

Assuming that the temperature of the frost surface for the part of the frost on the tube to be approximately the same as the surface temperature of the frost for the part of the frost on the fin base, the term $b_{f,p}$ can be made equal to the term $b_{f,m}$. Furthermore, the temperature of the pipe surface can be assumed equal to the temperature of the fin base, thus resulting in the following two enthalpy terms being equal: $i_{s,p} = i_{F,B}$. This simplifies Equation 3-20 to the following form after incorporating Equation 3-22:

$$\dot{Q} = \frac{h_{c,o,f}}{b_{f,m}} (A_{P,o} + \eta_F A_F) (i - i_{s,p}) \quad (3-23)$$

By definition, the overall heat transfer coefficient based on the enthalpy difference, $U_{o,f}$, may be expressed as

$$\dot{Q} = U_{o,f} A_o (i - i_{s,R}) \quad (3-24)$$

Employing Equations 3-19, 3-23, and 3-24 we get

$$U_{o,f} = \frac{1}{\frac{b'_R A_o}{A_{P,i} h_{c,i}} + \frac{b_{f,m}(1-\eta_F)}{h_{c,o,f}(A_{P,o}/A_F + \eta_F)} + \frac{b_{f,m}}{h_{c,o,f}}} \quad (3-25)$$

The overall heat transfer coefficient for a frosted finned tube coil based on the enthalpy difference is calculated using the above procedure at two locations, one at the entrance and the other at the exit of the coil. An average value is then computed.

Calculated path of the cooling and dehumidifying process. As has been explained earlier, when simultaneous cooling and dehumidification occurs, the overall heat transfer coefficient, $U_{o,f}$, is defined in terms of an enthalpy (and not a temperature) driving force. Furthermore, the enthalpy “ t ” is the true air enthalpy. This is to be contrasted with the quantity $i_{s,R}$ which can be thought of as a fictitious saturated air enthalpy evaluated at the refrigerant temperature. The mean enthalpy difference Δi_m is defined by the equation

$$\dot{Q} = U_{o,f} A_o \Delta i_m \quad (3-26)$$

The mean enthalpy difference Δi_m is defined by [modified from Incropera and Dewitt (1996)]

$$\Delta i_m = \frac{(i_1 - i_{s,R,2}) - (i_2 - i_{s,R,1})}{\text{Log}_e \left(\frac{i_1 - i_{s,R,2}}{i_2 - i_{s,R,1}} \right)} \quad (3-27)$$

where i_1 and i_2 are the true enthalpy values of the entering and leaving air conditions, respectively, and $i_{s,R,1}$ and $i_{s,R,2}$ are the fictitious enthalpies of saturated air calculated at the refrigerant entering and leaving conditions, respectively.

After calculating the inlet air conditions, the inlet refrigerant state, the various heat transfer coefficients, and the cooling coil surface data, the path of the cooling process can be determined. To get the enthalpy of saturated air at the mean frost surface temperature, we use the following equation:

$$i - i_{F,m} = \eta_F (i - i_{s,p}) = \frac{b_{f,m} h_{c,\rho}}{h_{c,\rho,f} C_{p,a}} (i - i_{s,f,m}) \quad (3-28)$$

And from Equations 3-19 and 3-24,

$$i - i_{s,p} = \left(1 - \frac{b'_R U_{o,f} A_o}{h_{c,l} A_{p,l}} \right) (i - i_{s,R}) \quad (3-29)$$

Using Equations 3-28 and 3-29, the enthalpy of saturated air evaluated at the mean frost surface temperature can be expressed by

$$i_{s,f,m} = i - \frac{C_{p,a} h_{c,\rho,f} \eta_F}{b_{f,m} h_{c,\rho}} \left(1 - \frac{b'_R U_{o,f} A_o}{h_{c,l} A_{p,l}} \right) (i - i_{s,R}) \quad (3-30)$$

For a given coil entering air condition, the quantity $i_{s,f,m,1}$ can be calculated. This determines State “s,f,m,1” on the psychrometric chart. This allows us to compute the quantity $i_1 - i_{s,f,m,1} / W_1 - W_{s,f,m,1}$. The slope at the coil entering air state, $(di/dW)_1$, can then be calculated according to the equation (Kuehn et al. 1998)

$$\left(\frac{di}{dW} \right)_1 = Le \frac{i_1 - i_{s,f,m,1}}{W_1 - W_{s,f,m,1}} + (i_{g,1} - i_g^o Le) \quad (3-31)$$

where Le is the Lewis number, $i_{g,1}$ is the enthalpy of saturated water vapor at the air dry-bulb temperature, and i_g^o is the enthalpy of saturated water vapor at a reference temperature (0°C). With the aid of the chart, we draw a short segment of direction $(di/dW)_1$ through State 1. With an arbitrary value of enthalpy we can locate a new point

on this segment. Then the procedure is repeated until the condition line meets with the state of saturated air at the coil apparatus dew-point temperature (approximately equal to the coil refrigerant temperature). Having determined the path of the cooling process, we can predict the condition downstream of any row using the following equation (Kuehn et al. 1998):

$$i_2 = \frac{i_{s,R,1}(1 - e^{-(1-C_3)C_4}) + i_1(1 - C_3)e^{-(1-C_3)C_4}}{1 - C_3e^{-(1-C_3)C_4}} \quad (3-32)$$

where $C_3 = \dot{m}_a b_R / \dot{m}_R C_{p,R}$ and $C_4 = U_{o,f} A_o / \dot{m}_a$. In computing the quantity C_4 , it should be kept in mind that the numerical value of A_o encompasses the areas of the row being calculated as well as all rows upstream of that row.

Results and Discussion

As was reported earlier, the objective of this section was to calculate the path the air would take as it passes through an industrial-size, finned-tube, multi-row freezer coil. The calculated path is to be then compared to the path obtained from the straight-line principle of applied psychrometrics in order to assess the goodness of the theoretical model. Table 3-3 provides a summary of the geometrical data of the coil under study, whereas the values of the parameters employed in the model are given in Table 3-4. Table 3-5 gives a summary of the numerical results obtained by applying the equations used to compute the overall heat transfer coefficient.

Table 3-3. Geometrical data of the finned coil

Tube outside diameter, mm	15.88
Tube inside diameter, mm	14.97
Tube spacing between rows, mm	38.10
Tube spacing across coil-face, mm	32.80
Thickness of fins, mm	0.25
Net outside surface area, m ²	6.23
Inside surface area, m ²	6.09
Fin surface area, m ²	43.37
Total outside surface area, m ²	49.60

Table 3-4. Parameter values employed in the model

Air inlet temperature, °C	0
Air inlet relative humidity, %	65
Air face velocity, m/s	3.8
Pipe surface temperature at the inlet, °C	-10
Pipe surface temperature at the outlet, °C	-2.2
Pipe mean surface temperature, °C	-6.1
Frost thickness, mm	1
Frost temperature at the coil inlet, °C	-6.1
Frost temperature at the coil outlet, °C	-1.8
Frost mean temperature, °C	-3.9
Fins efficiency, %	85

Table 3-5. Heat transfer coefficients using Equations 3-6, 3-11, 3-21, and 3-27

Internal heat transfer coefficient, W/(m ² K)	13471
External heat transfer coefficient, W/(m ² K)	107.8
Heat transfer coefficient for a frosted surface, W/(m ² K)	71.5
Overall heat transfer coefficient for a frosted finned-tube coil based on an enthalpy driving force, (kW kg)/(m ² . kJ)	0.075

In order to determine the calculated path for the conditions in Table 3-4, the surface area of the coil analyzed is arbitrarily divided into nine segments, thus producing ten state points through the coil. A summary of the conditions of these ten points is provided in Table 3-6. Figure 3-10 compares both the calculated and the straight-line dehumidifying paths. It is obvious that a path based on a straight-line process is in error to varying degrees, depending on the location of the point of interest relative to the coil. This can be easily demonstrated by comparing the relative humidity values of both the straight-line and calculated paths at a specific dry-bulb temperature.

Figure 3-11 displays both the calculated path showing the outlet conditions from successive rows in the coil as well as the entering and leaving air conditions based on experimental measurements. For example, experimental results for the leaving air conditions are: $DBT = -8.2^{\circ}\text{C}$ and $RH = 97\%$, while calculated leaving conditions are: $DBT = -8.4^{\circ}\text{C}$ and $RH = 97.4\%$, as is evident from examining Figure 3-11. Thus, there is a slight difference of 0.2°C in the dry-bulb temperature and 0.4% in the relative humidity. The differences in both temperature and humidity are insignificant and lie within the uncertainty bounds of both variables. As can be observed, the outlet conditions become more closely spaced towards the last rows of the coil, implying that more cooling is performed in the first half of the coil. This is because the enthalpy driving force assumes smaller values as the air passes through the coil rows.

Table 3-6. Calculated cooling process path through the coil

Point	$t (^{\circ}\text{C})$	$RH (\%)$	$W (\text{kg}_w/\text{kg}_a)$	$i (\text{kJ/kg})$	$i_{s,f,m} (\text{kJ/kg})$	(di/dW)
1	0	65.0	0.00240	6.04	-1.35	21310.36
2	1	70.0	0.00235	4.92	-1.79	19340.68
3	2	74.2	0.00229	3.76	-2.24	16783.44
4	3	78.5	0.00223	2.60	-2.69	14823.96
5	4	82.6	0.00216	1.40	-3.16	14094.55
6	5	86.2	0.00206	0.18	-3.63	13675.00
7	6	89.8	0.00198	-1.06	-4.11	11942.40
8	7	92.8	0.00188	-2.32	-4.61	11427.26
9	8	95.8	0.00178	-3.58	-5.10	9790.76
10	9	97.5	0.00163	-4.88	-5.60	-

Now that the cooling process path has been found, the coil location in the vicinity of which the transformation from a subsaturated state to a supersaturated state occurs, can be determined. In order to achieve this goal, we will assume that the percentage of energy removed by a given row of the coil relative to the total amount of energy that the coil can remove remains the same whether the air exists in a subsaturated state or a supersaturated state. Employing Figure 3-11, it is relatively easy to observe that the total

amount of cooling per unit mass performed by the coil is 10.1 kJ/kg. In Table 3-7, the amount of cooling per unit mass performed by each row and the percentage that that amount represents relative to the total amount of cooling are provided. As reported earlier, more cooling is performed in the first row relative to subsequent rows as shown in Figure 3-12. Carrying these cooling percentages to the supersaturated zone, the coil location in the vicinity of which transformation from a subsaturated condition to a supersaturated condition occurs can be calculated.

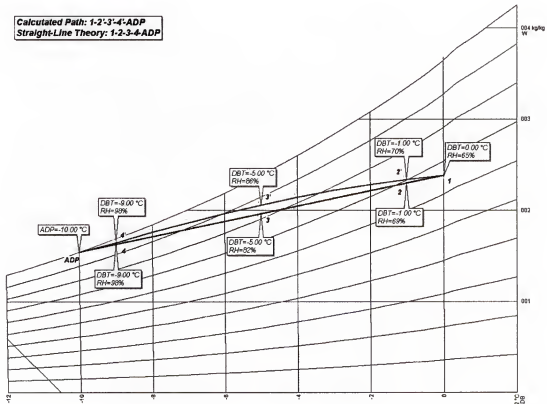


Figure 3-10. Representation of the actual and theoretical air paths through the dehumidifying coil (points on the chart are arbitrarily chosen for purposes of calculating the path)

Table 3-7. Amount of cooling and percentage of the total cooling for each row

Row	Δi (kJ/kg)	Percentage of total cooling (%)
R1	2.64	26.14
R2	2.00	19.80
R3	1.61	15.94
R4	1.23	12.18
R5	1.02	10.10
R6	0.74	7.33
R7	0.49	4.85
R8	0.37	3.66

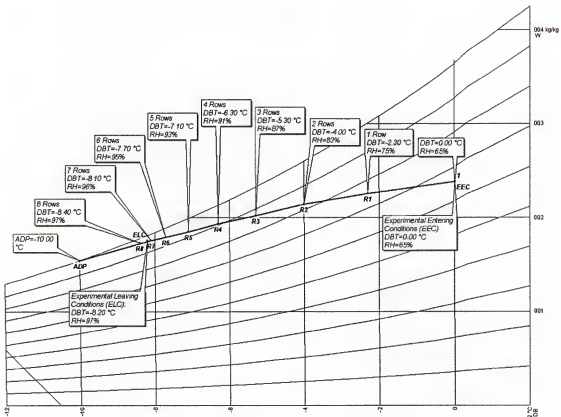


Figure 3-11. Representation of the actual air-cooling path through the dehumidifying coil showing the calculated leaving air conditions from each row as well as the measured coil inlet and outlet states

An experiment has been performed to verify the validity of the aforementioned assumption. In the experiment, the entering air temperature was kept constant at -8.3°C , while the relative humidity was steadily increased from 64% to 99%. The apparatus

dew-point was kept constant at -18.3°C throughout the experiment. The apparatus dew-point is the lowest temperature that the air can achieve during the cooling and dehumidifying process and is, thus, approximately equal to the coil refrigerant temperature. Results of this experiment are shown on the psychrometric chart of Figure 3-13 for both the straight-line theory and the calculated path. As can be seen, four scenarios were examined. For Scenario 1, the cooling process line falls completely in the subsaturated zone. For Scenario 2, transformation to the supersaturated zone using the straight-line theory occurs at Point $3a$ ($DBT=-15.1^{\circ}\text{C}$), while it occurs at Point $3a'$ ($DBT=-12.3^{\circ}\text{C}$) using the calculated path. For this scenario, the amount of cooling achieved using the straight-line theory represents 84% of the total cooling performed by the coil. This means that at Point $3a$ the air was leaving the fifth row supersaturated. However, the amount of cooling achieved using the calculated path represents only 50% of the total cooling performed by the coil. This means that at Point $3a'$ the air was leaving the third row supersaturated (as opposed to the fifth row for the straight-line theory). For Scenario 3, supersaturated conditions using the straight-line theory began at Point $3b$ ($DBT=-11.3^{\circ}\text{C}$) and using the calculated path at Point $3b'$ ($DBT=-10.3^{\circ}\text{C}$). For this scenario, the amount of cooling achieved using the straight-line theory represents 37% of the total cooling performed. This means that transformation to the supersaturated zone occurred between the second and third rows (Point $3b$). However, the amount of cooling achieved using the calculated path represents only 24% of the total cooling performed. This means that at Point $3b'$ the air was leaving the first row supersaturated. For Scenario 4, supersaturated conditions started at Point $3c$ ($DBT=-8.7^{\circ}\text{C}$) for both the straight-line theory and the calculated path. For this scenario, the amount of cooling

achieved from Points $1c$ to $3c$ or from Points $1c$ to $3c'$ represents 5% of the total cooling performed. This means that transition to the supersaturated state occurred in the vicinity of the first row. Obviously, as the relative humidity of the entering air increases, transition to a supersaturated state occurs quicker and at a more upstream location of the coil. This phenomenon has also been confirmed by other investigations performed by the authors (see Sherif et al. 2001).

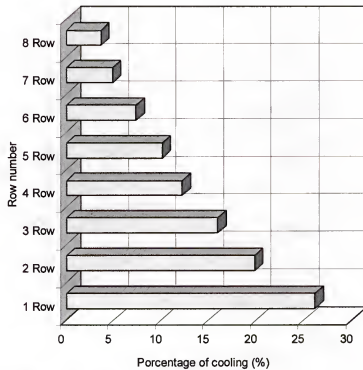


Figure 3-12. Percentage of the total cooling for each coil row

As was pointed out before, the procedure employed in this section is based on the premise that the percentage of cooling achieved between two consecutive rows of the coil will remain the same whether the air exists in the subsaturated or the supersaturated zone. In order to determine the percentage of cooling referred to above, the state of the air in the vicinity of two consecutive rows has to be known. The procedure described for determining the enthalpy at the exit of a given row is thus necessary for computing the

percentage of cooling. Employing this procedure necessarily produces a curved path for the air passing through the coil. While the bulk of the air paths lie in the subsaturated zone for all four processes shown, the procedure outlined is inherently capable of handling both supersaturated and subsaturated conditions. Using the straight-line theory to determine the air enthalpy in the vicinity of a given row produces results that are significantly less accurate than the ones produced using the curved-path. Figure 3-13 illustrates this point.

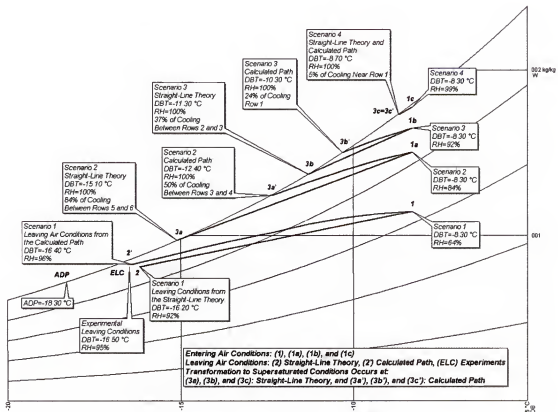


Figure 3-13. Representation of processes on the psychrometric chart showing where the transition to a supersaturated state occurs by keeping the same entering air temperature (-8.3°C) and gradually increasing the entering air relative humidity

While the straight-line theory and the calculated path approach agree reasonably well at the entrance and exit of the coil, significant differences between the two methods exist in the middle section of the coil. For example, Figure 3-13 shows a 34% deviation in the percentage of cooling calculated for Scenario 2 employing both methods. This is manifested in the differences between paths *1a-3a* and *1a-3a'*, where, in the former, the straight-line theory predicts 84% cooling achieved between Rows 5 and 6, whereas the corresponding value for Path *1a-3a'* is only 50%.

Conclusions

This chapter described a calculation procedure as well as an experiment for determining the air path on an actual industrial-size finned-tube, multi-row coil operating under frosting conditions. A calculated path based on the analysis presented and a path based on the straight-line theory of applied psychrometrics were correlated with the prevailing psychrometric conditions in the freezer. Determining the calculated path enabled accurate calculation of the conditions leaving a given row in a multi-row coil. This, in turn, helped identify the coil location in the vicinity of which the transformation from the subsaturated zone to the supersaturated zone occurred. This is crucial in identifying a demarcation line between the unfavorable snow-like frost and the more traditional frost-formation patterns. Calculated results were verified against experimental results at the entrance and exit of the coil with typical differences falling well within the uncertainty ranges of both temperature and humidity. In the middle section of the coil, on the other hand, significant deviations (up to 34%) between the calculated and the straight-line path were observed. This underscores the significance of using the method outlined in this chapter if reasonably accurate prediction of the location of the demarcation line between snow-like and conventional frost is to be determined.

According to results pertaining to the location of the demarcation line, transition to a supersaturated state occurs quicker and at a more upstream location of the coil as the relative humidity of the entering air increases.

CHAPTER 4 ISSUES PERTAINING TO HOT-GAS COIL DEFROSTING

Objectives

Previous coil defrosting studies have largely neglected the distinctions between two types of frost-formation patterns. As was mentioned before, the frost forming near saturated entering-air conditions is more snow-like in appearance and contributes more adversely to coil heat transfer performance than frost forming under predominantly subsaturated conditions. While the mechanisms of formation of both types of frost are similar in some aspects and different in others, the implications on the defrosting process are markedly different. It is thus the objective of this chapter to investigate the issues pertaining to the coil defrosting process using the hot-gas refrigerant method in order to provide a deeper insight and a better understanding of the problem in question. This method of defrosting was selected because it is the most widely used defrosting technique in industrial freezers.

Since available coil defrosting studies lack data on coils operating near saturated entering-air conditions, and since this seems to be a prevalent (but undesirable) mode of operation in industrial refrigeration applications, it was natural to investigate this mechanism further. This part of the study includes both physical and infrared analysis of a coil being defrosted. The infrared portion of the analysis will provide the spatial and temporal distributions of temperature on the coil surface, a key variable in understanding the defrosting dynamics. Throughout the study, an attempt will also be made to compare

the performance of the defrosted coil with those of similar coils operating under subsaturated conditions (e.g. Stoecker et al., 1983).

Analysis

A procedure used to calculate the defrost efficiency is described in this section.

Defrosting heat input rate.

$$\dot{Q}_{def,in} = \dot{m}_{R,vap} (i_{in} - i_{out}) \quad (4-1)$$

where $\dot{Q}_{def,in}$ is the defrosting heat input rate (kW), $\dot{m}_{R,vap}$ is the refrigerant mass flow rate (kg/s), i_{in} is the refrigerant inlet enthalpy (kJ/kg), and i_{out} is the refrigerant outlet enthalpy (kJ/kg). Defrosting heat input rates computed employing Equation 4-1 have a maximum uncertainty of $\pm 4\%$.

Defrosting heat input.

$$Q_{def,in} = \dot{m}_{R,vap} (i_{in} - i_{out}) \tau_{def} \quad (4-2)$$

where $Q_{def,in}$ is the defrosting heat input (kJ) and τ_{def} is the defrosting time (s). Defrosting heat inputs computed employing Equation 4-2 have a maximum uncertainty of $\pm 4\%$.

Refrigerant vapor mass flow rate. To calculate the defrosting heat input it is necessary to determine the mass flow rate of the refrigerant. The following procedure is used to calculate the vapor mass flow rate of the refrigerant:

- a. Calculate the volumetric flow rate (\dot{V}_R) from the measured value of the differential pressure across an orifice meter located on the hot-gas defrosting line. Detailed information regarding the shape, dimensions, and performance of the

orifice meter is provided by Sherif et al. (1997). To get the volumetric flow rate a fifth order polynomial equation is used

$$\dot{V}_R = 4.187657 \times 10^{-5} + (6.37861 \times 10^{-4} \Delta P) - (2.65091 \times 10^{-4} \Delta P^2) + (7.27778 \times 10^{-5} \Delta P^3) - (1.0033 \times 10^{-5} \Delta P^4) + (5.3196 \times 10^{-7} \Delta P^5) \quad (4-3)$$

where \dot{V}_R is the volumetric flow rate (m^3/s), and ΔP is the differential pressure across the orifice meter in inches of water column differential (inches WCD)

- b. Calculate the local average velocity ($u_{m,R}$) of the refrigerant vapor upstream of the orifice using the following equation:

$$u_{m,R} = \frac{\dot{V}_R}{A_{\text{orifice}}} \quad (4-4)$$

where A_{orifice} is the inside cross sectional area upstream of the orifice (m^2), and

where the inside diameter (D_1) of the pipe is 13.39 mm.

- c. From the properties of R-22 refrigerant vapor, calculate the Reynolds number (Re) as follows:

$$Re = \frac{\rho_R u_{m,R} D_1}{\mu_R} \quad (4-5)$$

where ρ_R is the density of the refrigerant vapor (kg/m^3) and μ_R is the dynamic viscosity of the refrigerant vapor [$\text{kg}/(\text{m s})$].

- d. Calculate the dimensionless discharge coefficient (C_d) of the orifice meter using the following equation (ASME 1991, Miller 1981):

$$C_d = 0.5959 + 0.0312\psi^{2.1} - 0.184\psi^8 + 0.039 \frac{\psi^4}{1-\psi^4} - 0.0158\psi^3 + \frac{91.71\psi^{2.5}}{\text{Re}^{0.75}} \quad (4-6)$$

where ψ is the ratio of the orifice throat diameter to the pipe inside diameter and is equal to 0.5.

- e. Calculate the dimensionless flow coefficient ($K_{orifice}$) of the orifice meter using the following equation (Fox and McDonald 1992, Miller 1981):

$$K_{orifice} = \frac{C_d}{\sqrt{1-\psi^4}} \quad (4-7)$$

- f. Calculate the mass flow rate ($\dot{m}_{R,vap}$) of the refrigerant vapor using the following equation (ASHRAE 2001 and Fox and McDonald 1992):

$$\dot{m}_{R,vap} = K_{orifice} A_{orifice} \beta^2 \sqrt{2g\rho_R\rho_{water}\Delta P} \quad (4-8)$$

where $\dot{m}_{R,vap}$ is the mass flow rate (kg/s), ρ_{water} and ρ_R are the density of water and refrigerant in (kg/m³), respectively, ΔP is the differential pressure across the orifice meter in meters of water column differential, and g is the acceleration of gravity (9.81 m/s²).

The uncertainties of the volumetric flow rate (\dot{V}_R), the local average velocity ($u_{m,R}$), the Reynolds number (Re), the discharge coefficient (C_d), the flow coefficient ($K_{orifice}$) of the orifice meter, and the refrigerant vapor mass flow rate ($\dot{m}_{R,vap}$) are, respectively, $\pm 2\%$, $\pm 2\%$, $\pm 3.5\%$, $\pm 1\%$, $\pm 1\%$, and $\pm 2.5\%$.

Rate of Heat Removed with the FCU-T Melt.

$$\dot{Q}_{melt} = \frac{m_{melt}(i_{llq} - i_{ice})}{\tau_{def}} \quad (4-9)$$

where \dot{Q}_{melt} is the rate of heat removed with the FCU-T melt (kW), m_{melt} is the mass of the melt during the defrosting process (kg), i_{llq} is the enthalpy of liquid water at the leaving

melt temperature (kJ/kg), and i_{ice} is the enthalpy of ice at the coil surface temperature (which is equal to the temperature of the frost at the beginning of the defrosting process) (kJ/kg). The rates of heat removed with the FCU-T melt computed employing Equation 4-9 have a maximum uncertainty of $\pm 4\%$.

Defrost efficiency.

The defrost efficiency is defined as the ratio between the rate of heat removed with the FCU-T melt and the total heat input rate for the defrosting process

$$\eta_{def} = \frac{\dot{Q}_{melt}}{\dot{Q}_{def,in}} \quad (4-10)$$

Defrost efficiencies computed using Equation 4-10 have a maximum uncertainty of $\pm 4\%$

There are two parameters of relevance to this defrosting problem; the average coil performance load rate, and the fan-defrost contribution. A procedure used to calculate, the average coil performance load rate, and the fan-defrost contribution is described in this section.

Average coil performance load rate. The average coil performance load rate (ACPLR) is defined as the ratio of the sum of the total refrigeration load and the defrost heat load divided by the total combined time of the FCU-T refrigeration and defrosting modes. The following procedure is used to calculate the average coil performance load rate, which has a maximum uncertainty of $\pm 4\%$:

- a. Calculate the total refrigeration load (Q_{total}) in kJ using the following equation:

$$Q_{total} = (\dot{Q}_{total,s} + \dot{Q}_{total,d})\tau_{ref} \quad (4-11)$$

where $\dot{Q}_{total,s}$ is the total sensible heat rate gain (kW), $\dot{Q}_{total,l}$ is the total latent heat rate gain (kW), and τ_{ref} is the duration of the FCU-T refrigeration mode (s).

b. Calculate the defrost heat load ($Q_{def,load}$) in kJ using the following equation:

$$Q_{def,load} = (\dot{Q}_{def,in} - \dot{Q}_{melt})\tau_{def} \quad (4-12)$$

where τ_{def} is the duration of the FCU-T hot-gas defrosting mode (s).

c. Calculate the total time duration (τ_{total}) for a complete FCU-T refrigeration and defrosting cycle using the following equation:

$$\tau_{total} = \tau_{def} + \tau_{ref} \quad (4-13)$$

d. Calculate the average coil performance load rate (ACPLR) in kW using the following equation:

$$ACPLR = \frac{Q_{total} + Q_{def,load}}{\tau_{total}} \quad (4-14)$$

Fan defrost contribution (FDC). In many refrigeration systems, the theoretical contribution of the fan and defrost heat loads to the net refrigeration load exceeds 15% of the net refrigeration load (ASHRAE 1998), where the net refrigeration load equals the total refrigeration load less the fan heat. Considering this idea, the ratio of the fan and defrost heat loads to the net refrigeration load has been utilized here in this investigation for comparative analysis among the various FCU-T refrigeration/defrost cycles. The following procedure is used to calculate the Fan-Defrost Contribution, which has a maximum uncertainty of $\pm 4\%$:

a. Calculate the fan heat (Q_{fan}) using the following equation:

$$Q_{fan} = \dot{Q}_{fan} \tau_{ref} \quad (4-15)$$

where \dot{Q}_{fan} is the fan power (kW) and τ_{ref} is the duration of the FCU-T refrigeration mode (s).

b. Calculate the net refrigeration load (Q_{net}) in kJ using the following equation:

$$Q_{net} = Q_{total} - Q_{fan} \quad (4-16)$$

where Q_{total} is the total refrigeration load calculated (kJ).

c. Calculate the fan-defrost contribution (FDC) in (%) using the following equation:

$$FDC = \frac{(Q_{fan} + Q_{def,load})}{Q_{net}} 100 \quad (4-17)$$

Results and Discussion

As was stated earlier, one of the objectives of this section was to examine the dynamics of defrosting freezer coils using the hot-gas refrigerant method for cases in which the coil entering-air conditions are in the vicinity of the saturation curve of the psychrometric chart. In order to achieve this objective, both infrared and physical images of the coil being defrosted are recorded at successive time increments. In order to provide some confidence in the authenticity of the data collected, a series of qualifications tests have been performed. In these tests, key defrost variables have been measured and compared with corresponding variables found in the open literature of similar coils. These tests are described and discussed below. It should be noted here, however, that existing data on coil defrosting in the open literature are available only for conventionally-frosted coils operating under subsaturated conditions. So, while the

comparison is not an exact one, analysis of the general trends could still prove useful and insightful.

Comparisons with and verification of existing defrosting data. Figure 4-1 shows the temperature-time history of the coil refrigerant temperatures at the inlet and outlet for the present experiment along with the experiments reported by Stoecker et al. (1983). As can be seen in the figure, the hot gas leaving the FCU-T pan then enters the FCU-T coil at a lower temperature due to the loss of heat when the hot gas mixes with the liquid refrigerant at and inside the FCU-T coil. The defrost refrigerant leaves the FCU-T coil at a lower temperature due to the mixing with the liquid refrigerant inside the FCU-T and also due to the refrigerant heat lost to melt the frost accumulated in the FCU-T coil. As can be seen, the trends are the same for both Stoecker's data and the present data, however the numerical values are different since the conditions used for the experiment are not the same as those of Stoecker et al. (1983).

A similar comparison has also been conducted with Stoecker's mass flow rate data as shown in Figure 4-2 and with Stoecker's pressure data as shown in Figure 4-3. The mass flow rate is high at the beginning of the defrosting process, but it falls off sharply during the first two minutes. Shortly afterward, the mass flow rate remains almost constant until the conclusion of the defrosting process. The trends observed in the mass flow rate data agree with those trends presented by Stoecker et al. (1983).

In Figure 4-3, the refrigerant pressures at the inlet and outlet of the coil during defrosting have been measured. From the trends observed, the inlet pressure increases at the beginning of the defrosting process until it reaches the value of the inlet pressure regulator. The difference between the inlet and outlet pressures is due to the pressure

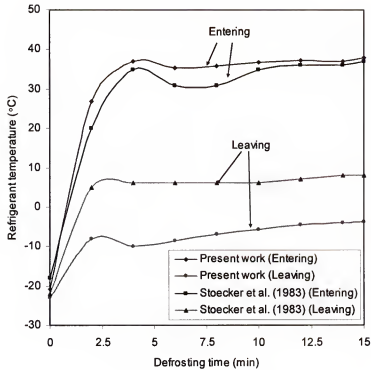


Figure 4-1. Refrigerant temperatures at the inlet and outlet of the coil during defrosting for both Stoecker et al. (1983) and present work

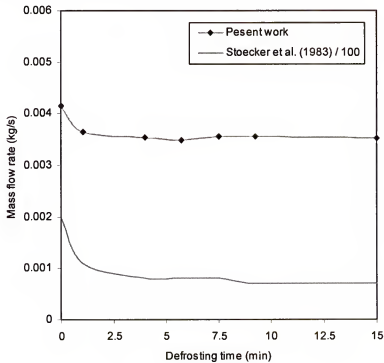


Figure 4-2. Mass flow rate of refrigerant during defrosting for both Stoecker et al. (1983) and present work

drop across the coil. Again, the trends are the same as those of Stoecker et al. (1983) even though the numerical values of pressures are different.

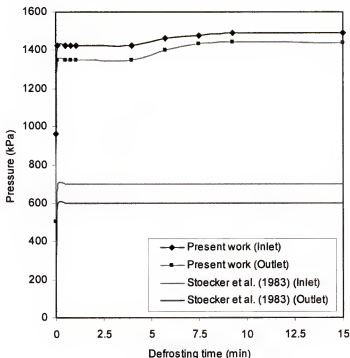


Figure 4-3. Refrigerant pressures at the inlet and outlet of the coil during defrosting for both Stoecker et al. (1983) and present work

Defrosting snow-like frost versus conventional frost. In order to experimentally investigate the complete refrigeration-defrost (R/D) cycle when the freezer operates under subsaturated and near saturated entering-air conditions, two tests were performed under the same initial freezer conditions, for 5 hours during refrigeration and 15 minutes during defrosting. Initial freezer air conditions were $DBT=-15^{\circ}\text{C}$ and $RH=75\%$, with an apparatus dew-point of -22°C . The coil face velocity for both tests was kept constant at 3.7 m/s.

Case a. In this case refrigeration was performed near saturated entering-air conditions. During the five hours of refrigeration 0.4 kg/h of steam were injected. Figure 4-4 shows the room and coil surface temperatures for a complete R/D cycle. The room temperature during the refrigeration process was between -12°C and -14°C for approximately four hours. As frost started to block the coil, the room temperature started to increase as the capacity of the coil to refrigerate was beginning to decline. At that point, the freezer air temperature has risen to 5°C . A visual image of the frosted coil at this stage is shown in Figure 4-5. The frost thickness before starting the defrosting process was 5 mm. Figure 4-6 shows an image of the coil five minutes into the defrosting process. In this figure, chunks of frost can be seen falling from the top instead of melting and collecting into the pan located at the bottom of the coil. Figure 4-7 shows an image of the coil ten minutes into the defrosting process. In this figure, chunks of frost continue to fall down from the top of the coil. It is noteworthy to observe how difficult the frost is to remove. Fifteen minutes into defrosting, the coil can still be seen with about half the amount of frost present (Figure 4-8). The amount of melt collected after performing the defrosting process was 0.36 kg. The total heat input into the defrosting process was 649.5 kJ and the total heat used in the melting process was 141.7 kJ, yielding a defrost efficiency of 21.8%. This is a rather poor defrost efficiency, which can be blamed on the small amount of melt collected and the corresponding large amount of evaporated melt and sublimated frost.

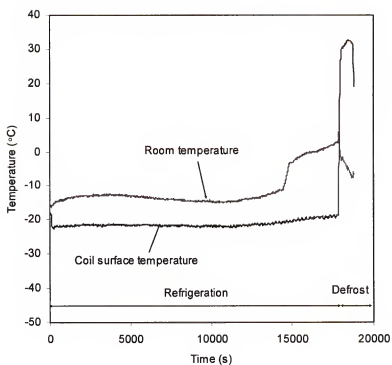


Figure 4-4. Freezer air and coil surface temperatures during refrigeration and defrosting

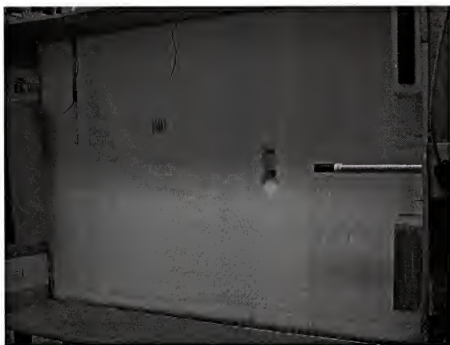


Figure 4-5. Coil condition after 5 hours of refrigeration under supersaturated conditions in the refrigeration mode (same as beginning of defrosting)



Figure 4-6. Coil after 5 minutes into the defrosting process

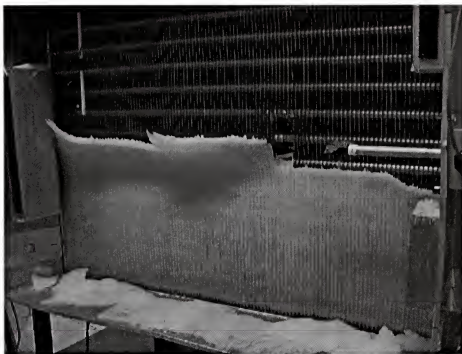


Figure 4-7. Coil after 10 minutes into the defrosting process

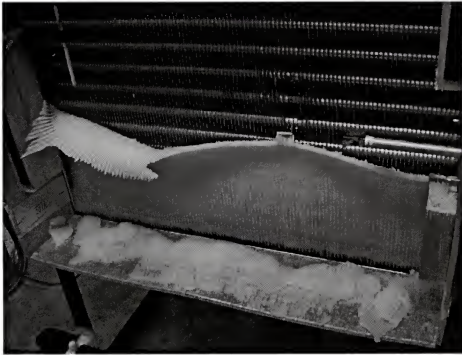


Figure 4-8. Coil after 15 minutes into the defrosting process

Case b. In this case the refrigeration process was conducted under subsaturated conditions for the same length of time as the previous experiment. Figure 4-9 displays both the freezer air and coil surface temperatures during the refrigeration portion of the R/D cycle. Freezer air temperature was approximately constant at -15°C , while the coil surface temperature was approximately constant at -22°C . Defrosting was not conducted in this case as very little frost could be detected after the lapse of five hours in the refrigeration mode (see Figure 4-10). This is in stark contrast to *Case a* and highlights the need to keep freezer air in a subsaturated condition.

As can be seen from Figures 4-5 and 4-10, operating freezers near saturated coil entering-air conditions produces a more dense, snow-like frost capable of blocking the coil in relatively short time periods and contributing adversely to the coil heat transfer performance.

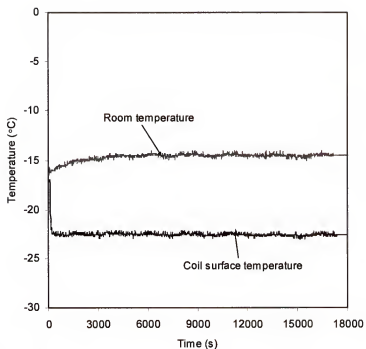


Figure 4-9. Freezer and coil surface temperatures during refrigeration

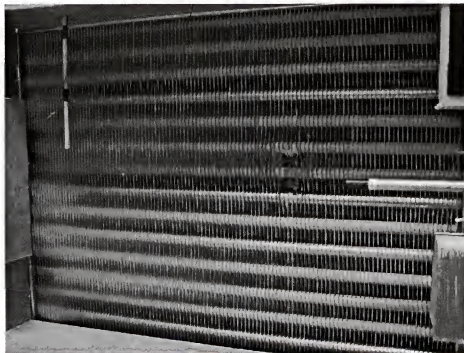


Figure 4-10. Coil after 5 hours of operation under subsaturated conditions during the refrigeration process

Infrared analysis of the defrosting process. In order to provide another insight of the changes taking place during defrosting, infrared images are shown as well (see Figures 4-11 through 4-15). These images are intended to show how the frost surface temperature changes with time as the defrost heat penetrates the frost layer on the coil. In order to get the numerical values of the frost surface temperature at key locations, five spots (T1, T2, T3, T4 and T5) were identified.

The average frost surface temperature before the beginning of the defrosting process was -13.3°C (Figure 4-11). One minute into defrosting (Figure 4-12), the temperature of the frost surface at the top left corner increases to -2.9°C . Three minutes into defrosting (Figure 4-13), the top of the coil is seen to have an average temperature of -2.5°C , while the rest of the frost has an average temperature of 8.6°C . After eight minutes (Figure 4-14), frost at the top part of the coil had already melted. In this figure one can observe the temperature of the metal surface of the coil. This temperature changes from 26.4°C at the top left corner to 11.7°C at the top right corner, while the average frost surface temperature for the remainder of the surface is only -2.1°C .

In order to create a more comprehensive picture of the quantitative variation in the frost surface temperature during defrosting, the temperature-time history of all five spots selected is plotted in Figure 4-15. In this figure one can observe that the spots located at the top of the coil (T1 and T2) reach higher temperatures faster than the others. Obviously, this thermal picture is consistent with the images of the physical coil while being defrosted shown earlier in this investigation. Five minutes into defrosting (Figure 4-16), one can observe that Spots T1 and T2 now represent the temperatures of the bare coil surface.



Figure 4-11. Frost surface temperature before the beginning of the defrosting process

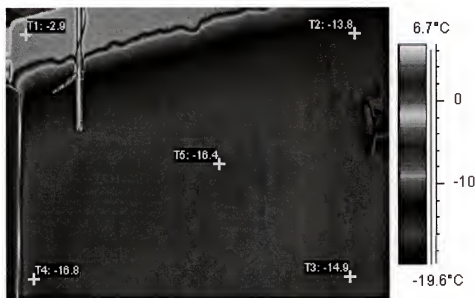


Figure 4-12. Frost surface temperature after 1 minute into defrosting

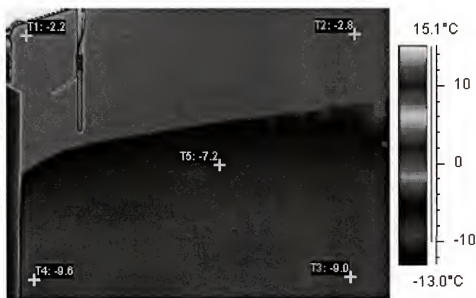


Figure 4-13. Frost surface temperature after 3 minutes into defrosting

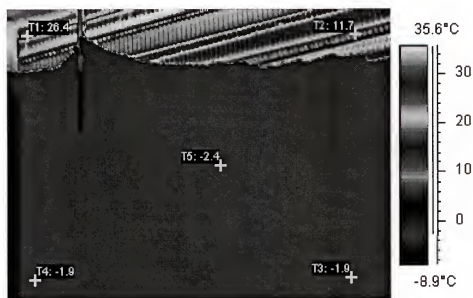


Figure 4-14. Frost surface temperature after 8 minutes into defrosting

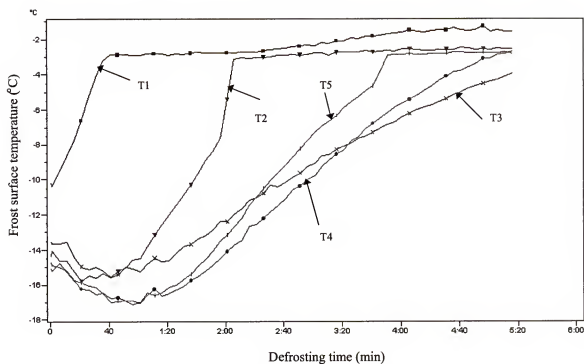


Figure 4-15. Frost surface temperature vs. time during defrosting

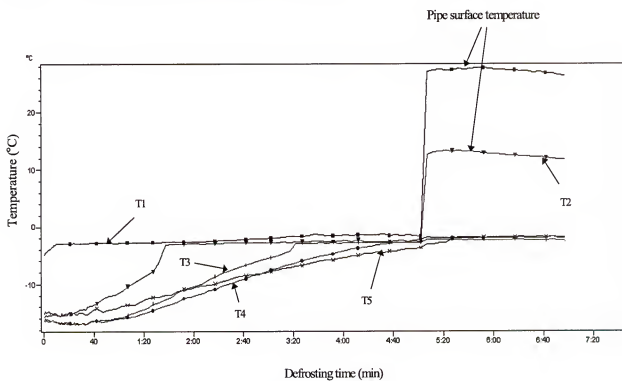


Figure 4-16. Frost and pipe surface temperatures vs. time during defrosting

Conclusions

An experimental study of a finned-tube freezer coil during hot-gas defrosting was conducted. The study included quantitative comparisons with similar coils as well as both quantitative and qualitative evaluations of the spatial and temporal distributions of both the frost surface temperature and the frost mass. Throughout the study, comparisons between two distinct types of frost were made both in the formation pattern and in the manner with which they melt during the defrosting process. Thermal images taken of the coil while being defrosted are consistent with the physical images of the defrosted coil. Comparisons with existing defrosting data were presented in order to provide some confidence in the experimental results presented.

CHAPTER 5

ALTERNATIVE ENERGY CONSERVATION TECHNOLOGIES IN INDUSTRIAL FREEZERS OPERATING UNDER FROSTING CONDITIONS

Objective

Operating freezers near saturated coil entering-air conditions produce a more dense, snow-like frost capable of blocking the coil in relatively short time periods and contributing adversely to the coil heat transfer performance. While every effort should be made to avoid operating the freezers and refrigerated facilities under these adverse conditions, some technologies may be available to lessen the negative impact of such conditions once operating in this mode becomes inevitable. This chapter will particularly target three distinct techniques; namely, the use of heat-pipe assisted heat exchangers, employing dampered coils, and operating freezer coils at high face velocities. The feasibility of these technologies will be explored both experimentally and analytically. The results will be supported by visual observations and images taken inside the laboratory freezer under study.

Feasibility of Heat Pipes

One of the technologies is the use of heat-pipe assisted freezer coils as a way to reduce the amount of energy required during the refrigeration portion of the refrigeration/defrost (R/D) cycle of operation. The main idea here is to let the sensible cooling be performed by one leg of a heat-pipe heat exchanger while letting the dehumidification part of the refrigeration process be performed by the actual freezer coil. This may provide some energy savings potential. In this section a discussion of the use

of heat pipes for dehumidification will be presented, followed by performing a comparative analysis with and without heat pipes.

Heat Pipes for Dehumidification

A heat pipe consists of a sealed container (made of aluminum or copper) whose internal surfaces have a capillary wicking material. This container has liquid inside (under its own pressure) that enters the pores of the capillary material, wetting all internal surfaces. When heat is applied at any point of the heat pipe the liquid at that point boils and changes to vapor. Then, the liquid picks up the latent heat of vaporization. The gas having a higher pressure, moves inside the sealed container to a colder location where it condenses. Thus, the gas gives up the latent heat of vaporization and moves heat from the input to the output end of the heat pipe. The difference between heat pipes and conventional heat exchangers is the capacity to transfer energy. For example, a heat pipe is capable of transferring 1000 times more energy than a solid copper bar, the best-known commercial conductor, without moving parts, external fans, connections to a fluid supply, noise, and external power.

In its in-line (wrap around) configuration, the heat pipe wraps around the dehumidification coil, with one section of the heat pipe coil upstream and one section downstream (Figure 5-1). Hot and humid air enters through the first heat pipe coil section where it is precooled prior to entering the dehumidification coil. This shifts the burden of sensible cooling to the upstream leg of the heat pipe coil instead of the dehumidification coil. Dehumidified air emerges from the cooling coil, passes through the second section of the heat pipe coil, where it is reheated to a temperature with a more comfortable relative humidity. Precooling and reheating by the heat pipe are performed

without any expenditure of external energy. The two sections of the heat pipe coil simply exchange precooling energy in the first section for reheating energy in the second section. A psychrometric depiction of dehumidification processes using heat pipes is shown in Figure 5-2.

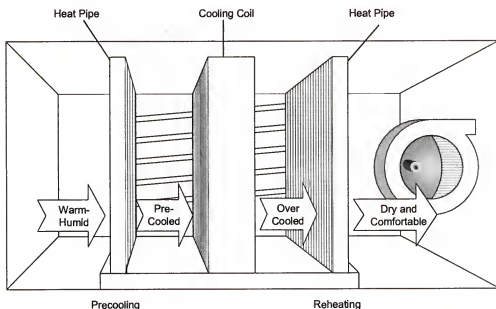


Figure 5-1. Heat pipe technology used in dehumidification processes

Calculation Software

In order to simulate the performance of the heat pipe-assisted coil, a calculation software, called HeatpipePRO, was used (Nelson 1999 private communications). This software was developed by Colmac Coil Manufacturing, Inc. Figure 5-3 shows the main screen of the software.

The data needed to operate this software are the inlet air dry-bulb temperature and either the wet-bulb temperature or the relative humidity, the altitude, the volumetric supply air flow rate in cfm (also, either scfm for standard conditions or acfm for altitude effects can be used), exhaust air dry-bulb temperature and either the wet-bulb temperature or the relative humidity, and the volumetric exhaust airflow rate in cfm.

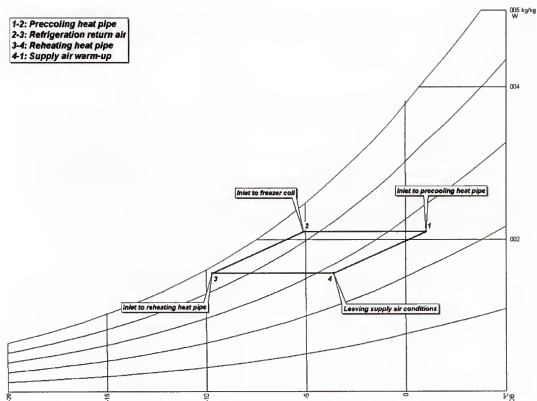


Figure 5-2. Representation of the dehumidification process using heat pipes

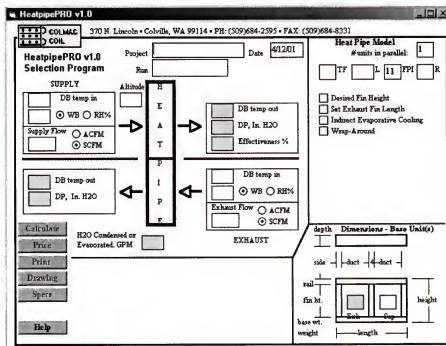


Figure 5-3. Main screen of the HeatpipePRO v1.0 software

Analysis of the Dehumidification Process

In order to demonstrate the advantages of using heat pipes, data from an experimental test are utilized in a computer code that simulates the performance of wrap-around heat pipe heat exchangers. The entering air conditions for the test were $DBT = 3^\circ\text{C}$ and $RH = 50\%$, while the apparatus dew-point temperature was $ADP = -11^\circ\text{C}$. The volumetric airflow rate was $90\text{ m}^3/\text{min}$ and the room sensible heat ratio 0.81 . The leaving air conditions, on the other hand, were $DBT = -8.2^\circ\text{C}$ and $RH = 88\%$. The cooling and dehumidification processes with and without heat pipes are shown in Figure 5-4.

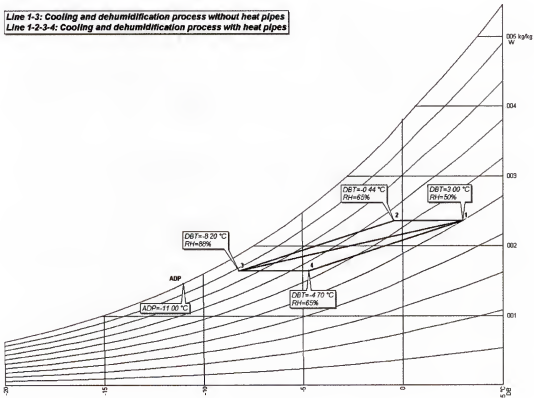


Figure 5-4. Coil and dehumidification processes with and without heat pipes

Line 1-3 represents the cooling and dehumidification process without heat pipes and Lines 1-2-3-4 represent the processes using heat pipes. For the cooling and dehumidification process using heat pipes, Line 1-2 represents the precooling heat pipe, Line 2-3 represents the cooling process through the coil, Line 3-4 represents the reheating heat pipe, and Line 4-1 represents the supply air warm-up path.

The total energy required for the cooling and dehumidification process without a heat pipe (Line 1-3) is 24.94 kW. However, the total energy required for the cooling and dehumidification process with a wrap-around heat pipe (Line 2-3) is 18.71 kW. The energy savings using a wrap-around heat pipe are represented by the energy associated with Line 1-2 (precooling process). This energy has a value of 6.23 kW. The total energy required for the cooling and dehumidification process decreases by 25% when a wrap-around heat pipe is used.

The same analysis can be conducted if two or more heat-pipes of the same model are used in parallel. This arrangement corresponds to stacked heat pipes, where the supply/exhaust air flow rates are distributed over the total amount of heat pipe surface area. In this case, the energy associated with Line 2-3 (cooling process through the coil) will be 16.8 kW, while that associated with Line 1-2 (precooling process) will be 8.14 kW and that associated with Line 3-4 (reheating process) will be 8.2 kW. Furthermore, the room sensible heat ratio will be 0.79 and the heat pipe effectiveness will be 39.1%. If three wrap-around heat pipe units are used in parallel, on the other hand, the energy associated with Line 2-3 (cooling process through the coil) becomes 15.92 kW, while that associated with Line 1-2 (precooling process) will be 9.02 kW. Also, the energy

associated with Line 3-4 (reheating process) will be 9.1 kW, with a room sensible heat ratio of 0.78 and a heat pipe effectiveness of 43.2%.

According to the above results, the heat pipe effectiveness increases and the energy required for cooling and dehumidification decreases when two or more wrap-around heat pipes are used in parallel. However, an important parameter to consider here is cost. The cost of two units in parallel is approximately 1.8 times the cost of a single heat pipe unit; while, the cost of three units in parallel is approximately 2.5 times the cost of a single unit.

When wrap-around heat pipes have to be selected for any application, the savings in energy as well as the financial savings have to be taken into consideration in order to make the best selection for the required application.

Analysis of the Energy Requirements

The total energy required for the cooling and dehumidification processes with and without heat pipes as a function of the entering air temperature is shown in Figure 5-5, for two relative humidity values. For the results shown in this figure, the following conditions apply: $ADP = -11^{\circ}\text{C}$, volumetric airflow rate = $90 \text{ m}^3/\text{min}$. The wrap-around heat pipe used was the same model employed before. The advantage of using heat pipes in terms of the energy required for cooling and dehumidification is illustrated in Figure 5-5. From this figure it can be seen that the energy required for cooling and dehumidification (with or without heat pipes) increases when the relative humidity increases.

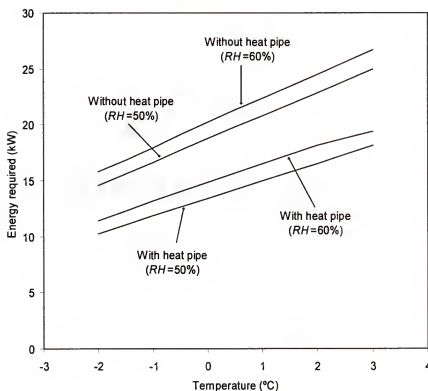


Figure 5-5. Energy required for cooling and dehumidification with and without heat pipes for two different relative humidities

Feasibility of Using Dampered Coils during the Defrosting Process

As was stated earlier, this study is concerned with the feasibility of using dampered fan-coil units and their potential in energy conservation by reducing the defrosting frequency. In order to achieve this goal, the defrost efficiency and the amount of melt collected at the end of the defrosting process were computed for a given set of freezer conditions. Typically, when an undampered coil is defrosted, part of the defrosting heat input goes into the freezer space in the form of evaporated water and sublimated frost instead of being used to melt the frost. However, if dampered coils are used, the heat that goes into the freezer space can be minimized and more heat can be applied to the actual melting of the frost. This will necessarily result in an increase in the defrost efficiency and the subsequent reduction in the frequency of coil defrosting.

The results presented in this section are significant for freezers with more than one cooling coil. This is because when one coil is in the defrosting mode; all others are usually in the refrigeration mode. Thus, a defrosting process with high efficiency, as manifested by a larger amount of melt and a smaller amount of evaporation and sublimation, will result in a smaller burden on all other coils, which may be simultaneously operating in the refrigeration mode inside the freezer. Any additional moisture generated by the coil being defrosted will immediately deposit on the remaining coils as undesirable frost and will necessarily increase the frequency of their defrosting cycle. If dampered coils are used, on the other hand, the additional moisture generated from the coil being defrosted will be trapped by the dampers and will eventually collect into the melt pan and be discharged outside the freezer. Also, when a significant amount of moisture is introduced into the freezer space due to improper defrosting practices, it is likely that freezer air may become supersaturated. Formations resulting from exposure to supersaturated air have been shown by Sherif et al. (2001) to be snow-like in crystal structure and much more extensive in amount than traditional formations when the air is subsaturated.

Results and discussion. In order to analyze the performance of dampered coils, either or both the coil suction and discharge were covered with plexiglass and supported by Velcro material as shown in Figures 5-6 and 5-7. The way the Plexiglass was installed in the coil suction and discharge is shown in Figures 5-8 and 5-9. Experiments were performed for three different scenarios: undampered coils, fully-dampered coils, and partially-dampered coils (at the coil suction only).

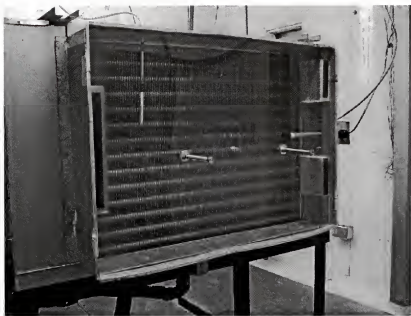


Figure 5-6. Coil suction covered with plexiglass and supported by Velcro material

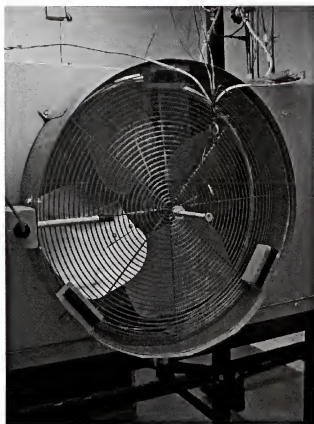


Figure 5-7. Coil discharge covered with plexiglass and supported by Velcro material

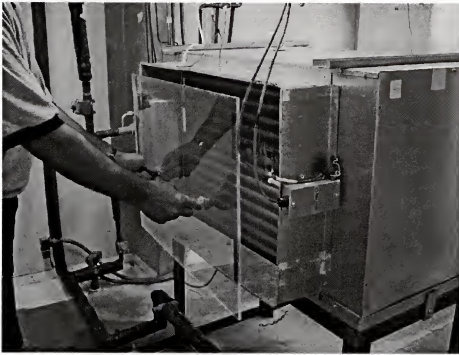


Figure 5-8. Coil suction being covered by plexiglass

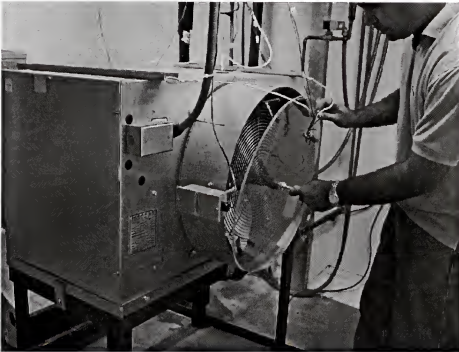


Figure 5-9. Coil discharge being covered by plexiglass

The initial conditions of the freezer air were held between -14.4°C and -13.3°C dry-bulb temperature and between 78% and 80% relative humidity for all tests in this

category. The coil-face velocity was 3.8 m/s. The length of the experiments was 6 hours under refrigeration and 15 minutes under defrosting. After each experiment was completed, the melt from the defrosting process was collected in order to determine the defrost efficiency.

For the undamped coil scenario, steady state conditions of freezer air at the beginning were $DBT=-14^{\circ}\text{C}$ and $RH=78\%$. Figure 5-10 shows an image of the coil before starting the defrosting process. The amount of melt collected after completing the defrosting process was 1.27 kg. The total heat input for the defrosting process was 730 kJ and the total heat used for melting the frost was 470.9 kJ, thus yielding a defrost efficiency of 64.5%.

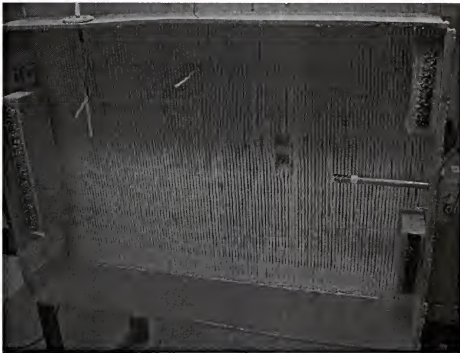


Figure 5-10. Conditions of the coil at the beginning of the defrosting process

For the fully-damped coil scenario, steady state conditions of freezer air at the beginning were $DBT=-14.4^{\circ}\text{C}$ and $RH=80\%$. Again, a visual image of the coil before starting the defrosting process is shown in Figures 5-11 and 5-12. Figures 5-13 and 5-14

show the appearance of the coil eight minutes into the defrosting process, while the appearance of the coil after the defrosting process has been completed can be seen in Figures 5-15 and 5-16. The amount of melt collected after completing the defrosting process was 1.81 kg, while the total heat input was 730 kJ. The total heat used for melting the frost was 671.6 kJ, thus giving a defrost efficiency of 92%.

For the partially-dampered coil scenario, steady state conditions of freezer air at the beginning were $DBT=-14.4^{\circ}\text{C}$ and $RH=80\%$. A visual image of the coil before starting the defrosting process is shown in Figure 5-17. Figure 5-18 shows the appearance of the coil eight minutes into the defrosting process, while Figure 5-19 shows the appearance after the defrosting process has been completed. The amount of melt collected after completing the defrosting process was 1.50 kg. The total heat input during the defrosting process was 729.1 kJ, while the total heat used for melting the frost was 552.6 kJ, thus yielding a defrost efficiency of 75.8%.

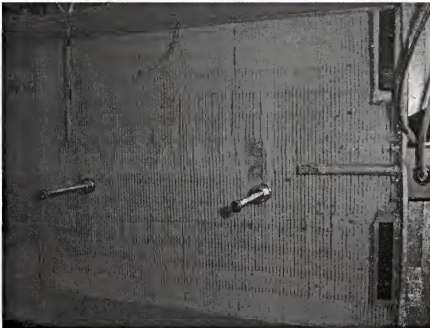


Figure 5-11. Conditions of the coil at the beginning of the defrosting process (suction side)



Figure 5-12. Conditions of the coil at the beginning of the defrosting process (discharge side)

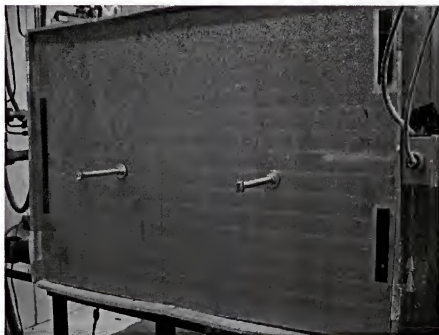


Figure 5-13. Conditions of the coil after 8 minutes into the defrosting process (suction side)

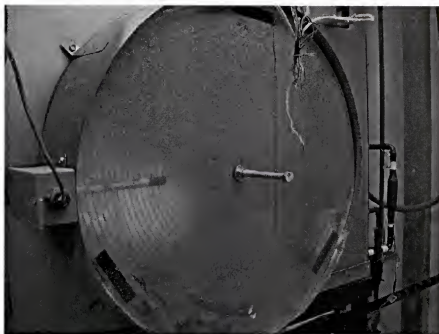


Figure 5-14. Conditions of the coil after 8 minutes into the defrosting process (discharge side)

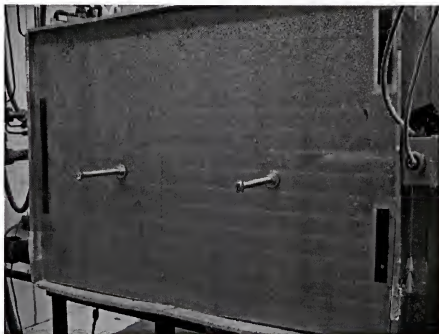


Figure 5-15. Conditions of the coil after 15 minutes into the defrosting process (suction side)

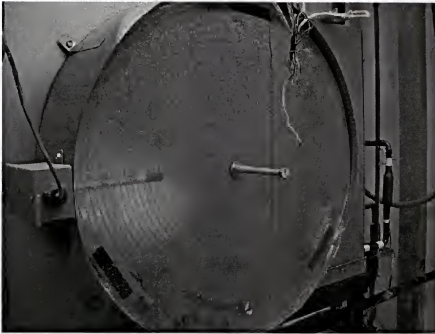


Figure 5-16. Conditions of the coil after 15 minutes into the defrosting process (discharge side)

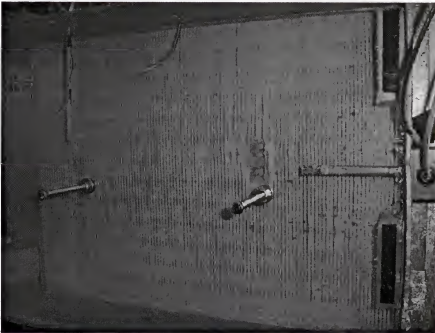


Figure 5-17. Conditions of the coil at the beginning of the defrosting process (suction side)

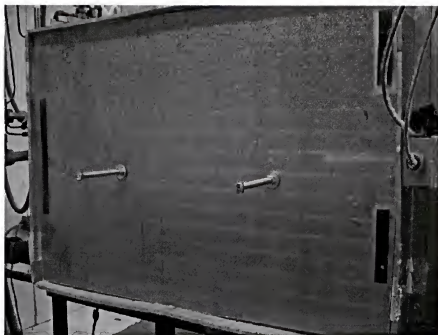


Figure 5-18. Conditions of the coil after 8 minutes into the defrosting process (suction side)

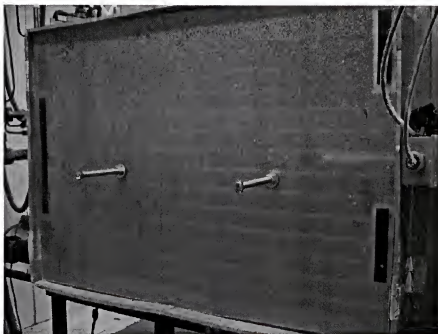


Figure 5-19. Conditions of the coil after 15 minutes into the defrosting process (suction side)

Figure 5-20 presents a graphical display of the defrost efficiency for all three scenarios. As can be seen, the defrost efficiency increases when a partially-dampened

coil is used relative to an undamped coil. Also, the highest defrost efficiency is obtained when a fully-damped coil is used. This means that the use of dampers helps increase the amount of melt collected and thus the defrost efficiency. Visual observations made inside the freezer for the undamped coil indicated that, the sublimated frost was visibly diffusing into the freezer space, resulting in a significant alteration of the conditions of the freezer air. When damped coils were used, on the other hand, the freezer remained clear because most of the sublimated frost was trapped in the enclosure between the dampers and the coil.

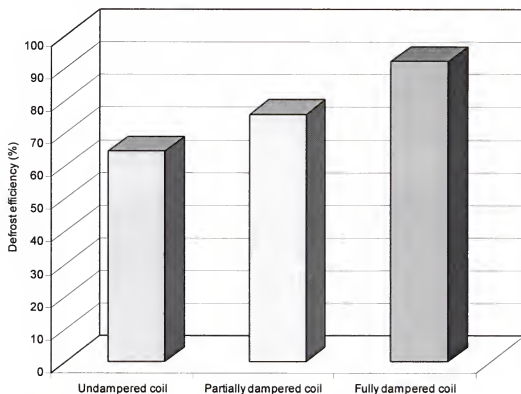


Figure 5-20. Defrost efficiency for the three scenarios analyzed

Visual observations made inside the freezer for the undamped coil indicated that, the sublimated frost was visibly diffusing into the freezer space, resulting in a significant alteration of the conditions of the freezer air. When damped coils were

used, on the other hand, the freezer remained clear because most of the sublimated frost was trapped in the enclosure between the dampers and the coil.

Operating Freezer Coils at High Face Velocities

In this section the effect of coil-face velocity is investigated for a coil operating under supersaturated conditions. In this study the amount of melt collected during defrosting and the defrost efficiency at several coil face velocities were determined. This study also examines the differences between the types of frost that forms at different coil-face velocities during the operation of freezers near saturated freezer air conditions. Some of the quantities analyzed include the defrost efficiency, the average coil performance load rate (*ACPLR*), and the fan defrost contribution (*FDC*). All these quantities were described in Chapter 4.

Results and discussion. In order to analyze the effect of the coil-face velocity for freezers operating under supersaturated conditions, two coil-face velocities were tried; 3.7 m/s and 6.5 m/s. Both scenarios were performed employing the same freezer initial conditions for five hours during refrigeration and fifteen minutes during defrosting. Initial freezer air conditions were $DBT=-14.6^{\circ}\text{C}$ and $RH=75\%$, with an apparatus dew-point of -22°C . During refrigeration, 0.38 kg/h of steam were injected into the freezer space. Supersaturated air existed throughout the refrigeration portion of the R/D cycle.

For the first scenario (case a), the coil-face velocity was 3.7 m/s. The freezer air temperature stayed between -12°C and -14°C for a period of four hours during the refrigeration portion of the cycle. Shortly afterward, air temperature in the freezer space started to rise due to frost deposition on the coil and the subsequent reduction in cooling capacity (complete cycle is graphically represented in Figure 5-21).

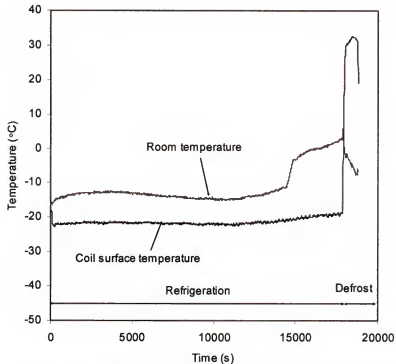


Figure 5-21. Freezer and coil temperatures during both refrigeration and defrosting (Case a)

For the second scenario (case b), the coil-face velocity was 6.5 m/s. Again, freezer air was supersaturated during the five hours of refrigeration. The complete R/D cycle for this case is shown in Figure 5-22. As can be observed, freezer air temperature stayed constant for about 3.8 hours, shortly after which it started to rise for the same reasons explained in the first case.

Successive images of the coil during the defrosting portion of the R/D cycle for both scenarios were taken and are presented in Figures 5-19 through 5-22. The effect of the coil-face velocity can be understood by comparing the corresponding images of the two cases. The initial frost thickness in Case a was 5 mm, while that for Case b was 4.5 mm. As can be seen in Figure 5-19, the frost in *Case a* looks more compact and dense than that of Case b.

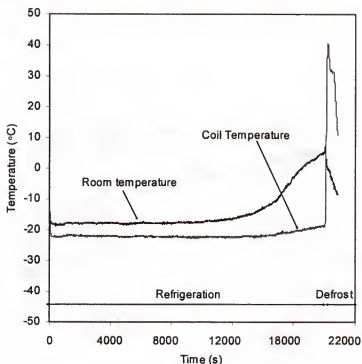


Figure 5-22. Freezer and coil temperatures during both refrigeration and defrosting (Case b)

Five minutes into defrosting, Figure 5-24 indicates that in Case a the frost at the top of the coil falls down instead of melting. This is contrary to what is observed for Case b, where the frost at the top of the coil was observed to melt instead of falling in chunks. This may say something about the degree of cohesiveness of the crystal structure of the two cases and the associated effect of a higher or lower coil-face velocity on the formation pattern.

Ten minutes into defrosting, Figure 5-25 indicates that in Case a the frost at the top of the coil continues to fall down instead of melting. For Case b, the frost at the top of the coil continues to melt, with only a small amount of frost falling in chunks. It can also be observed that the frost associated with Case a is thicker than that of Case b.

Fifteen minutes into defrosting, Figure 5-26 shows that in Case a the frost at the top of the coil continues to fall down in chunks instead of melting, with a significant

amount of frost still attached to the coil surface. At the higher coil-face velocity (Case b), the frost at the top of the coil continues to melt, with little frost falling down in chunks. Although in Case b the coil shows more frost than Case a, the frost layer in the latter case is thinner than that at the lower coil-face velocity (Case a). This is because a significant amount of the removed frost at the higher coil-face velocity has already melted instead of falling in chunks. Melted frost is drained outside the freezer, whereas frost falling in chunks eventually evaporates or sublimates into the freezer space and is recycled back into frost on coils operating in the vicinity of the coil being defrosted, thus increasing the frequency of defrosting these coils.

Results of this experiment are rather interesting as, in both cases; the fifteen minutes of defrosting were not sufficiently long to completely defrost the coil. The amount of melt collected at the conclusion of defrosting in Case a was 0.36 kg. The total heat input in the defrosting process was 649.5 kJ and the total heat used in the melting process was 141.7 kJ, thus yielding a defrost efficiency of 21.8%. For Case b, the amount of melt collected was 1.18 kg. The total heat input in the defrosting process was 661.6 kJ and the total heat used in the melting process was 465.3 kJ, thus yielding a defrost efficiency of 70.4%. Obviously, the defrost efficiency for Case b is higher than that for Case a. This necessarily implies that frost depositing at higher coil-face velocities is more likely to collect in the melt pan than to sublime into the freezer space.



A

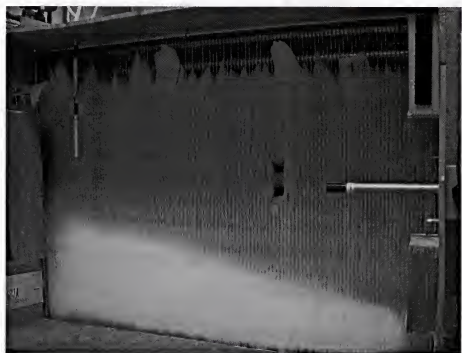


B

Figure 5-23. Comparison of the coil condition after 5 hours of refrigeration (same as the beginning of defrosting) for different coil-face velocities: A) Case a: 3.7 m/s and B) Case b: 6.5 m/s.

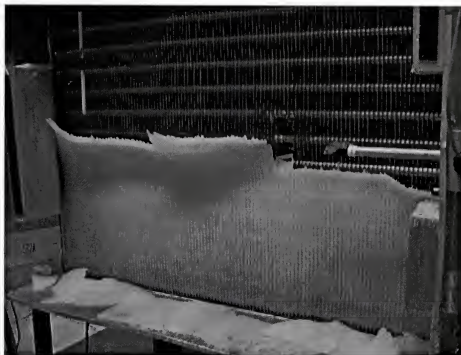


A

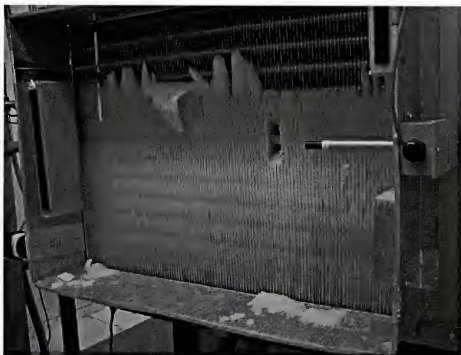


B

Figure 5-24. Comparison of coil condition 5 minutes into defrosting for different coil-face velocities: A) Case a: 3.7 m/s and B) Case b: 6.5 m/s.

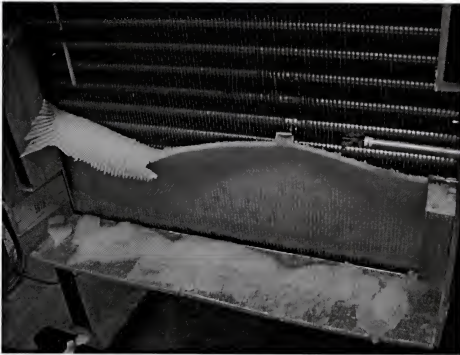


A

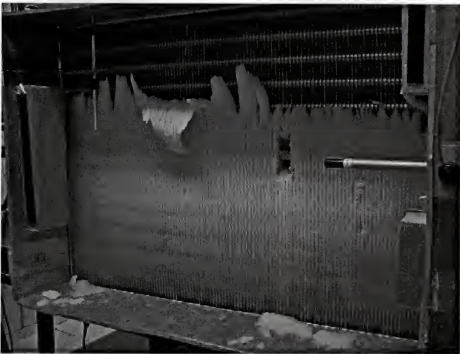


B

Figure 5-25. Comparison of coil condition 10 minutes into defrosting for different coil-face velocities: A) Case a: 3.7 m/s and b) Case b: 6.5 m/s.



A



B

Figure 5-26. Comparison of coil condition 15 minutes into defrosting for different coil-face velocities: (a) Case a: 3.7 m/s and (b) Case b: 6.5 m/s

In order to be able to create a meaningful plot of the defrost efficiency as a function of coil-face velocity, two more experiments were conducted. The coil-face velocities used in these experiments were 1.6 m/s and 5.23 m/s. Both experiments were performed under the same initial freezer conditions and the same rate of steam injection as the previous experiments. Results for these two coil-face velocities along with the previous ones are shown in Table 5-1. The corresponding graphical representation is shown in Figure 5-27.

Table 5-1. Defrost efficiency and melt collected in the defrosting process for different coil-face velocities

Coil-face velocity (m/s)	Heat input into defrosting (kJ)	Heat use in the melting process (kJ)	Melt collected (kg)	Defrost efficiency (%)
1.60	642.0	115.6	0.27	18.0
3.69	649.5	141.7	0.36	21.8
5.23	651.0	331.0	0.84	50.8
6.50	661.6	465.3	1.18	70.4

As can be seen in Figure 5-27, for coil-face velocities below 3.5 m/s, the defrost efficiency is almost constant. However, at higher coil-face velocities, the defrost efficiency can be seen to increase linearly with the velocity. This may be explained by attributing the higher amount of melted frost in the higher velocity case to a more coherent crystal structure that prevents frost falling in chunks in the higher velocity case. It may also cause frost to be more physically attached to the coil surface, thus making it more susceptible to the hot gas heat emanating from the inside of the coil.

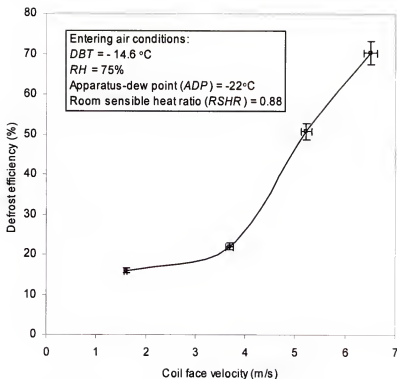


Figure 5-27. Defrost efficiency vs. coil-face velocity

It is important to note here, however, the potential implications of operating freezer coils at higher face velocities vis-à-vis the overall cost of the complete R/D cycle. While we may have a significantly larger defrost efficiency at higher face velocities, the additional fan power required at higher velocities may negate the advantages associated with the higher defrost efficiency. This may be particularly true since the duration of the refrigeration portion of the R/D cycle is typically several folds longer than that of the defrosting portion. For example, in the experiments performed here, the fan horsepower for the 3.7 m/s case was 1.12 kW smaller than that of the 6.5 m/s. Since the refrigeration portion of the cycle lasted five hours, the extra energy required for the 6.5 m/s case is 5.6 kWh.

On the other hand, operating at lower face velocities will result in a higher defrosting frequency because of the associated larger amount of moisture transfer into the freezer space. Thus, in a given 24-hour period, a coil operating at a lower face velocity will be defrosted several times more than one operating at a higher velocity. This is an additional source of energy expenditure that should be accounted for in deciding which face velocity to operate the coil at. Furthermore, defrosting coils employing the hot-gas refrigerant method frequently requires artificial generation of hot gas in order to have a sufficient amount of it to successfully perform the defrosting process. This hot-gas generation process may, for example, require the use of electric energy in the form of band heaters wrapped around the liquid-vapor separator in a liquid overfeed refrigeration system. A case-in-point is the system employed in this experimental investigation, whereby up to 10 kW of electric band heater power could be used to boil the refrigerant liquid in the liquid-vapor separator for the duration of at least part of the defrosting process. Obviously, more frequent defrosting cycles (as in the lower face velocity case) would make this option less attractive than the higher velocity scenario. This naturally needs to be factored into the decision making process.

Table 5-2 gives numerical values of the fan-defrost contribution, while the average coil performance load rate values are provided in Table 5-3. The values given in these tables are for coil-face velocities of 1.6 m/s, 3.7 m/s and 6.5 m/s.

Tabulated values of the fan-defrost contribution (*FDC*) are significantly larger than the values provided by ASHRAE (1998). ASHRAE suggests that the theoretical contribution of the fan and defrost heat loads to the net refrigeration load is approximately 15% or more. This suggests that a larger contribution should be

considered in cases involving a significant latent load. Also, the average coil performance load rate for all three coil-face velocities is remarkably similar. This latter result gives confidence in the accuracy of the experimental data collected.

Table 5-2. Fan-defrost contribution for coil-face velocities of 1.6 m/s, 3.7 m/s, and 6.5 m/s

Coil-face velocity	1.6 m/s	3.7 m/s	6.5 m/s
$Q_{total,s}$ (kJ)	39703.1	40388.9	41654.9
$Q_{total,l}$ (kJ)	5719.4	5719.4	5719.4
Q_{total} (kJ)	45422.6	46108.3	47374.3
Q_{fan} (kJ)	9495.0	10180.8	11446.8
Q_{net} (kJ)	35927.6	35927.6	35927.6
$Q_{def,in}$ (kJ)	642.0	649.5	661.6
Q_{melt} (kJ)	115.6	141.7	465.3
$Q_{def,load}$ (kJ)	526.4	507.8	196.3
FDC (%)	27.9	29.8	32.4

Table 5-3. Average coil performance load rate for coil-face velocities of 1.6 m/s, 3.7 m/s, and 6.5 m/s

Coil-face velocity	1.6 m/s	3.7 m/s	6.5 m/s
τ_{ref} (s)	18000	18000	18000
τ_{def} (s)	900	900	900
τ_{total} (s)	18900	18900	18900
Q_{total} (kJ)	45422.6	46108.3	47374.3
$\dot{Q}_{total,av}$ (kW)	2.40	2.44	2.51
$Q_{def,load}$ (kJ)	526.4	507.8	196.3
$\dot{Q}_{def,load,av}$ (kW)	0.03	0.03	0.03
ACPLR (kW)	2.43	2.47	2.52

Conclusions

In this chapter three alternative energy conservation technologies in industrial freezers and refrigerated facilities have been presented. The use of heat pipes is advantageous for freezer operation, because the energy required for the cooling and

dehumidification process decreases. This reduction in energy can be translated into financial savings. The use of partially-dampened coils was shown to increase the defrost efficiency by 18%, while the use of fully-dampened coils increases the efficiency by 43%. These dampers prevent evaporated water and sublimated frost from going back into the freezer space, thus helping reduce the defrosting frequency of other coils. Frost deposited at higher coil-face velocities is more cohesive and thus more likely to collect in the melt pan during defrosting than to sublimate back into the freezer space. At lower coil face velocities, the relative lack of cohesiveness of the frost is likely to result in a significant amount of moisture transfer to the freezer space and/or a structural collapse of chunks of frost on the freezer floor. This necessarily results in a smaller amount of collected melt and a correspondingly smaller defrost efficiency. It appears that a significant departure to a cohesive enough layer (that significantly affects the defrost efficiency) occurs at a coil face velocity of 3.5m/s. Frost deposited at face velocities of 6.5 m/s results in more than a four-fold increase in the defrost efficiency relative to that deposited at 1.6 m/s. Tabulated values of the fan-defrost contribution (*FDC*) also need to take into account the presence of latent loads in the freezer space. This represents a marked departure from the previous ASHRAE guidelines regarding the so-called fan-defrost contribution. Furthermore, the average coil performance load rate for all three coil-face velocities is remarkably similar. This latter result gives confidence in the accuracy of the experimental data collected.

CHAPTER 6

FORMULATIONS OF THERMODYNAMIC PROPERTIES OF SUPERSATURATED AIR

Objectives

The most exact formulations of thermodynamic properties of moist air in the temperature range of -100°C to 200°C are based on the study of Hyland and Wexler (1983a, b). More recent studies by Sauer et al. (2001) and Nelson et al. (2001) provide psychrometric data for moist air in the temperature range of 200°C to 320°C and humidity ratios from 0 to 1 kg/kg_a at pressures 0.07706, 0.101325, 0.2, 1.0, and 5 MPa. Both studies developed the psychrometric data using the most current values of the virial coefficients, enthalpy, and entropy of both air and water vapor. Other psychrometric data were generated by Stewart et al. (1983), who created psychrometric charts in SI units at low pressures. More psychrometric charts are available in the ASHRAE brochure on psychrometry (Olivieri et al. 1996).

While psychrometric tables and charts exist for subsaturated moist air for a relatively large temperature range, no such data is available under supersaturated conditions. This deficiency in the body of data has historically impeded our ability to analyze and study frost and ice formation processes on coils exposed to supersaturated air. These coils may exist in a variety of engineering situations such as industrial walk-in freezers and loading-docks, to name a few. While every attempt should be made to avoid operating coils under those conditions, developing this body of data should enable the refrigeration engineer and system designer to better predict the performance of the

system as well as design a more optimal system. The objective of this section is thus to provide a systematic way of calculating key air properties under supersaturated conditions for the purpose of improving our prediction capability under those conditions.

Properties of Supersaturated Moist Air

In this section, the development of psychrometric formulations as well as thermodynamic properties for supersaturated air from -40 to 40°C will be presented. Supersaturated air is a mixture of saturated air and suspended liquid water droplets or ice crystals depending on whether the prevailing air temperature is larger or smaller than the freezing point temperature, respectively. Therefore the properties of supersaturated air may be determined using the individual properties of those of saturated air and those of the suspended liquid droplets or ice crystals. These properties are developed employing the virial equation of state and other relevant methods. The virial equation can be written as

$$\frac{P \bar{v}_m}{\bar{R} T} = 1 + \frac{B_{ii}}{\bar{v}_m} + \frac{C_{iii}}{\bar{v}_m^2} \quad (6-1)$$

In Equation 6-1, B_{ii} is the second virial coefficient for gas “ i ”, C_{iii} is the third virial coefficient for gas “ i ”, \bar{v}_m is the molar specific volume, and \bar{R} is the universal gas constant (8.31441 kPa m³/(kmol K)). The subscripts “ i ” are equal to “ a ” for dry air and “ w ” for water vapor. The subscript “ m ” will replace the i ’s subscripts to indicate the air-water vapor mixture (Olivieri et al. 1996)

$$B_m = x_a^2 B_{aa} + 2x_a x_w B_{aw} + x_w^2 B_{ww} \quad (6-2)$$

$$C_m = x_a^3 C_{aaa} + 3x_a^2 x_w C_{aaw} + 3x_w^2 x_a C_{aww} + x_w^3 C_{www} \quad (6-3)$$

where x_a and x_w are the mole fractions of air and water vapor respectively, B_{aa} and B_{ww} are the second virial coefficients for dry air and water vapor, respectively, C_{aaa} and C_{www} are the third virial coefficients for dry air and water vapor, respectively, and B_{aw} , C_{aaw} , and C_{aww} are the cross virial coefficients for moist air.

The second and third virial coefficients for dry air, B_{aa} (cm^2/mol) and C_{aaa} (cm^6/mol^2), respectively, are given by Olivieri et al. (1996) according to the following:

$$B_{aa} = 34.9568 - \frac{6687.72}{T} - \frac{0.210141 \times 10^7}{T^2} + \frac{0.924746 \times 10^8}{T^3} \quad (6-4)$$

$$C_{aaa} = 1259.75 - \frac{0.190905 \times 10^6}{T} + \frac{0.632467 \times 10^8}{T^2} \quad (6-5)$$

The second and third virial coefficients for water vapor, B_{ww} (cm^2/mol) and C_{www} (cm^6/mol^2), respectively, are expressed as (Olivieri et al. 1996)

$$B_{ww} = \bar{R}T \left[0.70 \times 10^{-8} - 0.147184 \times 10^{-8} \exp\left(\frac{1734.29}{T}\right) \right] \quad (6-6)$$

$$C_{www} = (\bar{R}T)^2 \left\{ 0.104 \times 10^{-14} - 0.335297 \times 10^{-17} \exp\left(\frac{3645.09}{T}\right) + \left(0.70 \times 10^{-8} - 0.147184 \times 10^{-8} \exp\left(\frac{1734.29}{T}\right) \right)^2 \right\} \quad (6-7)$$

The cross virial coefficients for moist air, B_{aw} (cm^2/mol), C_{aaw} (cm^6/mol^2), and C_{aww} (cm^6/mol^2), are expressed as (Olivieri et al. 1996)

$$B_{aw} = 32.366097 - \frac{0.141138 \times 10^5}{T} - \frac{0.1244535 \times 10^7}{T^2} - \frac{0.2348789 \times 10^{10}}{T^3} \quad (6-8)$$

$$C_{aaw} = \left[482.737 + \frac{0.105678 \times 10^6}{T} - \frac{0.656394 \times 10^8}{T^2} + \frac{0.294442 \times 10^{11}}{T^3} - \frac{0.319327 \times 10^{13}}{T^4} \right] \quad (6-9)$$

$$C_{aww} = -1 \times 10^6 \exp \left[-10.728876 \times 10^2 + \frac{0.347802 \times 10^4}{T} - \frac{0.383383 \times 10^6}{T^2} + \frac{0.33406 \times 10^8}{T^3} \right] \quad (6-10)$$

The above coefficients have been calculated using Equations 6-4 through 6-10 and are summarized in Table 6-1. The temperature derivatives have also been calculated and are given in Table 6-2.

Table 6-1. Value of the virial coefficients

<i>t</i> (°C)	<i>B_{aa}</i> (cm ³ /mol)	<i>C_{aaa}</i> (cm ⁶ /mol ²)	<i>B_{ww}</i> (cm ³ /mol)	<i>C_{www}</i> (cm ⁶ /mol ²)	<i>B_{aw}</i> (cm ³ /mol)	<i>C_{aaw}</i> (cm ⁶ /mol ²)	<i>C_{aww}</i> (cm ⁶ /mol ²)
-40	-25.0889	1604.4441	-4837.4598	-54249456.48	-51.8588	971.079	-795863.7234
-30	-21.6586	1544.3847	-3711.5848	-30621660.01	-47.4018	941.8068	-556734.3014
-20	-18.5521	1492.552	-2911.788	-18137967.62	-43.3786	913.3703	-401252.0739
-10	-15.7288	1447.6264	-2329.5237	-11211706.74	-39.7299	886.3439	-296660.4159
0	-13.1543	1408.5352	-1896.2673	-7198239.87	-36.4067	861.0182	-224216.3255
10	-10.7993	1374.4001	-1567.5254	-4780658.789	-33.3679	837.5067	-172750.726
20	-8.6387	1344.497	-1313.6677	-3272857.046	-30.5792	815.815	-135368.5722
30	-6.6509	1318.225	-1114.5057	-2302551.893	-28.0114	795.8843	-107679.4618
40	-4.8173	1295.0824	-955.9962	-1660201.825	-25.6398	777.6198	-86810.3558

Table 6-2. Temperature derivatives of the virial coefficients

t (°C)	dB_{aa}/dT (cm ³ /mol K)	dC_{aaa}/dT (cm ⁶ /mol ² K)	dB_{ww}/dT (cm ³ /mol K)	dC_{www}/dT (cm ⁶ /mol ² K)	dB_{aw}/dT (cm ³ /mol K)	dC_{aaw}/dT (cm ⁶ /mol ² K)	dC_{aww}/dT (cm ⁶ /mol ² K)
-40	0.3608	-6.4687	134.0212	4741841.882	0.4697	-2.9396	29764.0056
-30	0.3261	-5.5702	94.0267	2485668.989	0.4229	-2.8981	19018.5847
-20	0.2959	-4.8182	67.6965	1370887.445	0.3827	-2.7799	12603.6273
-10	0.2694	-4.1847	49.8733	790868.1648	0.3479	-2.6207	8617.1634
0	0.246	-3.6481	37.5051	474898.199	0.3175	-2.4427	6052.6767
10	0.2254	-3.1909	28.7286	295559.8373	0.2908	-2.2596	4352.5921
20	0.2071	-2.7996	22.3742	189952.7577	0.2674	-2.0798	3195.4595
30	0.1908	-2.4631	17.6890	125666.3880	0.2466	-1.908	2389.3459
40	0.1762	-2.1724	14.1768	85341.8427	0.2281	-1.7468	1816.0418

Thermodynamic Properties

Specific volume: The following equations represent the specific volume for dry, moist, and supersaturated air, and for saturated ice and water:

- **Dry air:** The specific volume for dry air in m³/kmol can be determined from Equation 6-1 by changing the subscripts “i” by “a” and \bar{v}_m by \bar{v}_a

$$\bar{v}_a = \frac{\bar{R}T}{P} \left(\frac{B_{aa}}{\bar{v}_a} + \frac{C_{aaa}}{\bar{v}_a^2} \right) \quad (6-11)$$

- **Moist subsaturated air:** The specific volume for moist air in m³/kmol can be determined from Equation 6-1 by changing the subscripts “i” by “m”

$$\bar{v}_m = \frac{\bar{R}T}{P} \left(\frac{B_m}{\bar{v}_m} + \frac{C_m}{\bar{v}_m^2} \right) \quad (6-12)$$

The specific volume can be expressed per unit mass of dry air in m³/kg as

$$v_m = \frac{\bar{v}_m}{28.9645 x_a} \quad (6-13)$$

At saturation v_m becomes v_g , and x_a and x_w become $x_{a,s}$ and $x_{w,s}$, respectively.

- Saturated ice: The specific volume of saturated ice in m^3/kg ($173.15\text{K} \leq T \leq 273.15$) is obtained from (Olivieri et al. 1996)

$$v_{ice} = 0.1070003 \times 10^{-2} - 0.249936 \times 10^{-7} T + 0.371611 \times 10^{-9} T^2 \quad (6-14)$$

- Saturated water: The specific volume of saturated water in m^3/kg is obtained from (Olivieri et al. 1996)

$$v_{liquid} = \frac{a_6 + a_7 T}{\sum_{i=0}^5 a_i T_i} \quad (6-15)$$

$$\begin{aligned} \text{where} \quad a_0 &= -2403.360201 & a_4 &= 0.373497936 \times 10^{-6} \\ a_1 &= -1.40758895 & a_5 &= -2.1203787 \times 10^{-10} \\ a_2 &= 0.1068287657 & a_6 &= -3.424442728 \\ a_3 &= -0.2914492351 \times 10^{-3} & a_7 &= 0.01619785 \end{aligned}$$

- Moist supersaturated air: In order to determine the specific volume of supersaturated air, it is necessary first to introduce the definition of the humidity ratio of supersaturated air (W_{super}). This can be thought of as the humidity ratio of air at saturation (W_s) plus the mass of excess moisture beyond saturation (either liquid or ice) per unit mass of dry air (m_{drop}/m_a). This can be expressed by

$$W_{super} = \frac{m_{ws} + m_{drop}}{m_a} = W_s + \frac{m_{drop}}{m_a} \quad (6-16)$$

The specific volume of supersaturated air can be expressed per unit mass of mixture as follows:

$$\tilde{v}_{super} = \frac{m_a v_a + m_{ws} v_{ws} + m_{drop} v_{drop}}{m_{super}} \quad (6-17)$$

where m_{super} is the total mass of the mixture and it can be expressed as

$$m_{\text{super}} = m_a + m_{\text{ws}} + m_{\text{drop}} \quad (6-18)$$

where m_a is the mass of dry air, m_{ws} is the mass of saturated water vapor, and m_{drop} is the mass of excess moisture beyond saturation.

Introducing Equation 6-18 into Equation 6-17 gives

$$\tilde{v}_{\text{super}} = \frac{m_a}{m_a + m_{\text{ws}} + m_{\text{drop}}} v_a + \frac{m_{\text{ws}}}{m_a + m_{\text{ws}} + m_{\text{drop}}} v_{\text{ws}} + \frac{m_{\text{drop}}}{m_a + m_{\text{ws}} + m_{\text{drop}}} v_{\text{drop}} \quad (6-19)$$

Equation 6-19 can be written as:

$$\tilde{v}_{\text{super}} = \frac{1}{1 + W_s + \frac{m_{\text{drop}}}{m_a}} v_a + \frac{W_s}{1 + W_s + \frac{m_{\text{drop}}}{m_a}} v_{\text{ws}} + \frac{m_{\text{drop}}/m_a}{1 + W_s + \frac{m_{\text{drop}}}{m_a}} v_{\text{drop}} \quad (6-20)$$

Using the relation for the supersaturated humidity ratio (Equation 6-16) Equation 6-20 can be expressed as follows:

$$\tilde{v}_{\text{super}} = \frac{1}{1 + W_{\text{super}}} [v_s + v_{\text{drop}} (W_{\text{super}} - W_s)] \quad (6-21)$$

The specific volume of supersaturated air can be also expressed per unit mass of dry air as follows:

$$v_{\text{super}} = \tilde{v}_{\text{super}} \frac{m_{\text{super}}}{m_a} = \tilde{v}_{\text{super}} (1 + W_{\text{super}}) \quad (6-22)$$

Using Equations 6-30 and 6-31 the specific volume of supersaturated air can be expressed as

$$v_{\text{super}} = v_s + v_{\text{drop}} (W_{\text{super}} - W_s) \quad (6-23)$$

where v_{drop} can either be v_{liquid} or v_{ice} depending on the air temperature.

Specific enthalpy: The following virial equations represent the specific enthalpy for dry and moist air, and for saturated ice and water.

- **Dry air:** The specific enthalpy of dry air can be expressed in kJ/kmol by

$$\bar{i}_a = \sum_{i=0}^5 b_i T^i + \bar{R} T \left[\left(B_{aa} - T \frac{dB_{aa}}{dT} \right) \bar{v}_a^{-1} + \left(C_{aaa} - 0.5T \frac{dC_{aaa}}{dT} \right) \bar{v}_a^{-2} \right] \quad (6-24)$$

where

$b_0 = -7907.8691$	$b_3 = -0.10405863 \times 10^{-4}$
$b_1 = 28.709015$	$b_4 = 0.1866041 \times 10^{-7}$
$b_2 = 0.0026431805$	$b_5 = -9.7843331 \times 10^{-12}$

- **Moist subsaturated air:** The specific enthalpy of moist subsaturated air can be expressed in kJ/kmol by

$$\begin{aligned} \bar{i}_m = x_a \left(\sum_{i=0}^5 e_i T^i + i_{a,0} \right) + x_w \left(\sum_{i=0}^5 f_i T^i + i_{w,0} \right) \\ + \bar{R} T \left[\left(B_m - T \frac{dB_m}{dT} \right) \bar{v}_m^{-1} + \left(C_m - 0.5T \frac{dC_m}{dT} \right) \bar{v}_m^{-2} \right] \end{aligned} \quad (6-25)$$

where

$e_0 = -6.3290874$	$f_0 = -0.005008$
$e_1 = 28.709015$	$f_1 = 32.491829$
$e_2 = 0.0026431805$	$f_2 = 0.0065576345$
$e_3 = -0.000010405863$	$f_3 = -0.000026442147$
$e_4 = 0.00000001866041$	$f_4 = 0.000000051751789$
$e_5 = -9.7843331 \times 10^{-12}$	$f_5 = -3.1541624 \times 10^{-11}$
$i_{a,0} = -7.9141982 \text{ kJ/kmol}$	$i_{w,0} = 35.99417 \text{ kJ/kmol}$

The enthalpy of moist air per unit mass kJ/kg is given by

$$i_m = \frac{\bar{i}_m}{28.9645 x_a} \quad (6-26)$$

At saturation i_m becomes i_s , and x_a, x_w , and v_m become x_{as}, x_{ws} , and v_s , respectively.

- **Saturated ice:** The enthalpy of saturated ice water in kJ/kg is given by

$$i_{ice} = \sum_{i=0}^3 g_i T^i + g_4 P_s \quad (6-27)$$

where

$$\begin{aligned} g_0 &= -647.595 & g_3 &= 0.1083437 \times 10^{-5} \\ g_1 &= 0.274292 & g_4 &= 0.107 \times 10^{-5} \\ g_2 &= 0.002910583 \end{aligned}$$

- **Saturated water:** The enthalpy of saturated liquid water in (kJ/kg) is given by

$$i_{liquid} = \alpha - 0.01214 + T v_{liquid} \frac{dP_s}{dT} \times 10^{-3} \quad (6-28)$$

where α is given by Equation 6-29 for the range of $273.15 \text{ K} \leq T \leq 373.15 \text{ K}$ (Olivieri et al., 1996)

$$\alpha = \sum_{i=0}^4 j_i T^i - 0.563473 \times 10^{-0.036(T-273.15)} \quad (6-29)$$

where

$$\begin{aligned} j_0 &= -0.1141138 \times 10^4 & j_3 &= 0.1451133 \times 10^{-6} \\ j_1 &= 4.1930463 & j_4 &= -0.100523 \times 10^{-9} \\ j_2 &= -0.8134865 \times 10^{-4} \end{aligned}$$

In order to determine the enthalpy of saturated water, the derivative of the saturation pressure with temperature is needed. The saturation pressure over ice for the temperature range of $173.15 \text{ K} \leq T \leq 273.15 \text{ K}$ is given by (ASHRAE 2001)

$$\log_e(P_s) = \frac{l_0}{T} + l_1 + l_2 T + l_3 T^2 + l_4 T^3 + l_5 T^4 + l_6 \log_e(T) \quad (6-30)$$

where: $l_0 = -0.56745359 \times 10^4$ $l_4 = 0.20747825 \times 10^{-8}$
 $l_1 = -5.152305 \times 10^{-1}$ $l_5 = -0.9484024 \times 10^{-12}$
 $l_2 = -0.9677843 \times 10^{-2}$ $l_6 = 0.41635019 \times 10^1$
 $l_3 = -0.62215701 \times 10^{-6}$

The saturation pressure over liquid water for the temperature range of $273.15\text{K} \leq T \leq 473.15\text{K}$ can be written as (ASHRAE 2001)

$$\log_e(P_s) = \frac{n_0}{T} + n_1 + n_2 T + n_3 T^2 + n_4 T^3 + n_5 \log_e(T) \quad (6-31)$$

where $n_0 = -0.58002206 \times 10^4$ $n_3 = 0.41764768 \times 10^{-4}$
 $n_1 = -0.5516256 \times 10^1$ $n_4 = -0.14452093 \times 10^{-7}$
 $n_2 = -0.48640239 \times 10^{-1}$ $n_5 = 0.65459673 \times 10^1$

In both Equations 6-30 and 6-31, P_s is in Pa.

- Moist supersaturated air: The enthalpy of supersaturated air can be expressed per unit mass of mixture as follows:

$$\tilde{i}_{\text{super}} = \frac{m_a i_a + m_{ws} i_w + m_{\text{drop}} i_{\text{drop}}}{m_{\text{super}}} \quad (6-32)$$

where m_{super} is the total mass of the mixture (Equation 6-18)

With the use of Equation 6-18 Equation 6-32 can be written as

$$\tilde{i}_{\text{super}} = \frac{m_a}{m_a + m_{ws} + m_{\text{drop}}} i_a + \frac{m_{ws}}{m_a + m_{ws} + m_{\text{drop}}} i_w + \frac{m_{\text{drop}}}{m_a + m_{ws} + m_{\text{drop}}} i_{\text{drop}} \quad (6-33)$$

or

$$\tilde{i}_{sup\ er} = \frac{1}{1 + W_s + \frac{m_{drop}}{m_a}} i_a + \frac{W_s}{1 + W_s + \frac{m_{drop}}{m_a}} i_w + \frac{m_{drop}/m_a}{1 + W_s + \frac{m_{drop}}{m_a}} i_{drop} \quad (6-34)$$

Using the relation for the supersaturated humidity ratio (Equation 6-16) Equation 6-34 can be expressed as follows:

$$\tilde{i}_{sup\ er} = \frac{1}{1 + W_{sup\ er}} \left[i_s + i_{drop} (W_{sup\ er} - W_s) \right] \quad (6-35)$$

The enthalpy of supersaturated air can be also expressed per unit mass of dry air as follows:

$$i_{sup\ er} = \tilde{i}_{sup\ er} \frac{m_{sup\ er}}{m_a} = \tilde{i}_{sup\ er} (1 + W_{sup\ er}) \quad (6-36)$$

Using Equations 6-35 and 6-36 the enthalpy of supersaturated air per unit mass of dry air can be expressed as:

$$i_{sup\ er} = i_s + i_{drop} (W_{sup\ er} - W_s) \quad (6-37)$$

where i_{drop} can either be i_{liquid} or i_{ice} depending on the air temperature.

Specific entropy: The following equations represent the specific entropy for dry and moist air:

- **Dry air:** The specific entropy of dry air in kJ/kmol K can be determined from Olivieri et al. (1996)

$$\begin{aligned} \bar{s}_a = \sum_{i=0}^4 o_i T^i + o_s \log_e T + \bar{R} \left\{ \left(-\log_e \left(\frac{P}{P_{atm}} \right) + \log_e \left(\frac{P \bar{v}_a}{\bar{R} T} \right) \right) \right. \\ \left. - \left[\left(B_{aa} + \frac{dB_{aa}}{dT} \right) \frac{1}{\bar{v}_a} + \frac{1}{2} \left(C_{aaa} + T \frac{dC_{aaa}}{dT} \right) \frac{1}{\bar{v}_a^2} \right] \right\} \end{aligned} \quad (6-38)$$

where

$$\begin{aligned} o_0 &= -0.16175159 \times 10^3 & o_3 &= 0.24880547 \times 10^{-7} \\ o_1 &= 0.52863609 \times 10^{-2} & o_4 &= -0.12230416 \times 10^{-10} \\ o_2 &= -0.15608795 \times 10^{-4} & o_5 &= 0.287091015 \times 10^2 \end{aligned}$$

- Moist subsaturated air: The specific entropy of moist air in kJ/kmol K can be determined from

$$\begin{aligned} \bar{s}_m &= x_a \left(\sum_{i=0}^4 u_i T^i + u_5 \log_e T + s_{a,0} \right) + x_w \left(\sum_{i=0}^5 w_i T^i + w_5 \log_e T + s_{w,0} \right) + \\ &\bar{R} \left\{ -\log_e \left(\frac{P}{P_{atm}} \right) + x_a \log_e \left(\frac{P \bar{v}_m}{x_a \bar{R} T} \right) - x_w \log_e \left(\frac{P \bar{v}_m}{x_w \bar{R} T} \right) \right\} \\ &- \left[\left(B_m + \frac{dB_m}{dT} \right) \frac{1}{\bar{v}_m} + \left(C_m + T \frac{dC_m}{dT} \right) \frac{1}{2\bar{v}_m^2} \right] \end{aligned} \quad (6-39)$$

where

$$\begin{aligned} u_0 &= -0.34373874 \times 10^2 & w_0 &= 0.21966034 \times 10^1 \\ u_1 &= 0.52863609 \times 10^{-2} & w_1 &= 0.19743819 \times 10^{-1} \\ u_2 &= -0.15608795 \times 10^{-4} & w_2 &= -0.70128225 \times 10^{-4} \\ u_3 &= 0.24880547 \times 10^{-7} & w_3 &= 0.14866252 \times 10^{-6} \\ u_4 &= -0.12230416 \times 10^{-10} & w_4 &= -0.14524437 \times 10^{-9} \\ u_5 &= 0.28709015 \times 10^2 & w_5 &= 0.55663583 \times 10^{-13} \\ s_{a,0} &= -0.196125465 \text{ kJ/kmol K} & w_6 &= 0.32284652 \times 10^2 \\ s_{w,0} &= -0.06331449 \text{ kJ/kmol K} \end{aligned}$$

The specific entropy per unit mass of dry can be expressed air in kJ/kg K as

$$s_m = \frac{\bar{s}_m}{28.9645 x_a} \quad (6-40)$$

At saturation s_m becomes s_g , and x_a and x_w become x_{at} and x_{ws} , respectively.

- Saturated ice: The specific volume of saturated ice in kJ/kg K in the range $(173.15\text{K} \leq T \leq 273.15)$ is obtained from

$$s_{ice} = -4.470727 + 0.502109 \times 10^{-2} T + 0.5624155 \times 10^{-5} T^2 - 0.274292 \log_e T \quad (6-41)$$

$$+ (-0.249936 \times 10^{-7} + 0.743288 \times 10^{-9} T)(101325 - P_{ws}) \times 10^{-3}$$

- Saturated water: The specific volume of saturated water in kJ/kg K in the range $(273.15\text{K} \leq T \leq 373.15)$ is obtained from

$$s_{liquid} = \sum_{i=0}^3 z_i T^i + z_4 \log_e T + z_5 \exp[z_6 (T - 273.15)] + v_{liquid} \frac{dP_{ws}}{dT} \times 10^{-3} \quad (6-42)$$

where $z_0 = -234.707325$ $z_4 = 2.4188095$

$z_1 = -0.1177858 \times 10^{-3}$ $z_5 = -0.1976361 \times 10^{-2}$

$z_2 = 0.1501808 \times 10^{-6}$ $z_6 = -0.0865209$

$z_3 = -0.8946646 \times 10^{-10}$

- Moist supersaturated air: The specific entropy per unit mass of mixture of supersaturated air can be expressed as follows:

$$\tilde{s}_{super} = \frac{m_a s_a + m_{ws} s_w + m_{drop} s_{drop}}{m_{super}} \quad (6-43)$$

where m_{super} is the total mass of the mixture. Using a procedure similar to the one employed to determine the specific volume and specific enthalpy; it can be shown that the specific entropy of supersaturated air per unit mass of dry air can be expressed as follows:

$$s_{super} = s_a + s_{drop} (W_{super} - W_s) \quad (6-44)$$

where s_{drop} can either be s_{liquid} or s_{ice} depending on the air temperature.

Specific heat:

▪ Moist subsaturated air:

$$C_{pm} = C_{pa} + W_m C_{pw} \quad (6-45)$$

where C_{pa} and C_{pw} are the specific heat of dry air and water vapor, respectively, and W_m is the humidity ratio of moist air. At saturation C_{pm} becomes C_{ps} and W_m becomes W_s .

▪ Moist supersaturated air:

$$C_{p\ super} = C_{ps} + C_{pdrop}(W_{super} - W_s) \quad (6-46)$$

where C_{ps} is the specific heat of air at saturated conditions, and C_{pdrop} is the specific heat of saturated water, which can either be C_{liquid} or C_{pice} depending on the air temperature.

Psychrometric Formulations

Mole fraction of air and water vapor. Moist air is considered to be saturated when its relative humidity has a value of 100%. In this state the mole fraction of air is given by x_{as} , while that of water vapor is given by x_{ws} . These can be expressed as

$$x_{as} = \frac{P - \varepsilon P_{ws}}{P} \quad (6-47)$$

$$x_{ws} = \frac{\varepsilon P_{ws}}{P} \quad (6-48)$$

where ε is the enhancement factor expressed by Equation 6-49, P_{ws} is the partial pressure of water vapor at saturation and P is the total pressure. The enhancement factor (ε) is a correction parameter that takes into account the effect of dissolved gases and pressure on

the properties of the condensed phase, as well as the effect of intermolecular forces on the properties of moisture itself (ASHRAE 2001). Olivieri et al. (1996) proposed the following equation to determine this factor:

$$\begin{aligned} \log_e(\varepsilon) = & \left[\frac{(1 + \gamma P_{ws})(P - P_{ws}) - \beta(P^2 - P_{ws}^2)/2}{RT} \right] \bar{v}_c + \ln(1 - \beta x_{as} P) + \left[\frac{x_{as}^2 P}{RT} \right] B_{aa} \\ & - \left[\frac{2x_{as}^2 P}{RT} \right] B_{aw} - \left[\frac{(P - P_s - x_{ws}^2 P)}{RT} \right] B_{ww} + \left[\frac{3x_{as}^2(1 - x_{as})^2 P^2 - P_{ws}^2}{2(\bar{RT})^2} \right] C_{aaw} \\ & + \left[\frac{x_{as}^3 P^2}{\bar{R}^2 T^2} \right] C_{aaa} - \left[\frac{(1 + 2x_{as})(1 - x_{as})^2 P^2 - P_{ws}^2}{2(\bar{RT})^2} \right] C_{www} \\ & - \left[\frac{x_{as}^2(1 - 3x_{as})(1 - x_{as})P^2}{(\bar{RT})^2} \right] B_{aa} B_{ww} - \left[\frac{2x_{as}^3(2 - 3x_{as})P^2}{(\bar{RT})^2} \right] B_{aa} B_{ww} \\ & + \left[\frac{6x_{as}^2(1 - x_{as})^2 P^2}{(\bar{RT})^2} \right] B_{ww} B_{aw} - \left[\frac{3x_{as}^4 P^2}{2\bar{R}^2 T^2} \right] B_{aa}^2 - \left[\frac{3x_{as}^2(1 - x_{as})P^2}{(\bar{RT})^2} \right] C_{aaw} \\ & - \left[\frac{2x_{as}^2(1 - x_{as})(1 - 3x_{as})P^2}{(\bar{RT})^2} \right] B_{aw}^2 - \left[\frac{P_{ws}^2(1 + 3x_{as})(1 - x_{as})^3 P^2}{2(\bar{RT})^2} \right] B_{ww}^2 \end{aligned} \quad (6-49)$$

where \bar{v}_c is the specific molar volume of liquid water in m^3/kmol , x_{as} and x_{ws} are the mole fractions of air and water vapor at saturation, respectively.

Equation 6.49 must be solved using a numerical method because x_{as} and x_{ws} are both functions of ε . The term β is the Henry's Law constant, and it accounts for air dissolved in liquid water. This term can be expressed in (1/Pa) as

$$\beta = 1 \times 10^{-4} \frac{\beta_a^{-1}}{101325} \quad (6-50)$$

where β_a is the Henry's law constant for air. This term can be determined from

$$\frac{1}{\beta_a} = \frac{x_{O_2}}{\beta_{O_2}} + \frac{x_{N_2}}{\beta_{N_2}} \quad (6-51)$$

where $x_{O_2} = 0.22$ and $x_{N_2} = 0.78$ are the mole fractions of oxygen and nitrogen in the air. Himmelblau (1960) gives a set of equations to compute β_{O_2} and β_{N_2}

$$\beta_{O_2} = \exp(-19.786773 + 23.293048T - 9.8984983T^2 + 2.2363172T^3 - 0.29618434T^4 + 0.01708493T^5) \quad (6-52)$$

and

$$\begin{aligned} \beta_{N_2} = & -288743.088 + 111167.594T + \frac{491323.518}{T} - 27988.2964T^2 \\ & - \frac{529382.752}{T^2} + 4444.4453T^3 + \frac{328398.259}{T^3} - 404.940980T^4 \\ & - \frac{89505.6879}{T^4} + 16.1931127T^5 \end{aligned} \quad (6-53)$$

The term γ is the isothermal compressibility of liquid water and it can be determined from (Nelson et al. 2001) in (1/Pa)

$$\gamma = \frac{7.1201893 \times 10^{-7} + 5.2000728 \times 10^{-9} T}{\left(1 + 0.0109329T - 0.3305 \times 10^{-4} T^2\right)^2} \quad (6-54)$$

where $T \leq 450$ K and where the pressures are less than 1MPa.

Equation 6-49 has been numerically solved for a temperature ranging from -60°C to 60°C and the results are presented in Table 6-3. In order to propose a new simplified equation for the enhancement factor the data presented in Table 6-3 are fitted into a polynomial represented by Equation 6-55.

$$\begin{aligned} \varepsilon = & 1.00391723 - 7.8220553 \times 10^{-6} t + 6.94681594 \times 10^{-7} t^2 \\ & + 3.040587 \times 10^{-9} t^3 - 2.7852 \times 10^{-11} t^4 - 5.656 \times 10^{-13} t^5 \end{aligned} \quad (6-55)$$

where t is the temperature in °C.

Table 6-3. Enhancement factor obtained numerically solving Equation 6-49

Temperature (°C)	Enhancement factor (ϵ)
-60	1.0063
-50	1.0057
-40	1.0051
-30	1.0047
-20	1.0043
-10	1.0041
0	1.0039
10	1.0039
20	1.0041
30	1.0044
40	1.0048
50	1.0053
60	1.0058

Air humidity ratio:

- Moist subsaturated air: This can be expressed by

$$W_m = 0.62198 \frac{\epsilon P_w}{P - \epsilon P_w} \quad (6-56)$$

where P_w is the partial pressure of water vapor and P is the total pressure. At saturation W_m becomes W_s , and P_w becomes P_s .

- Moist supersaturated air: This can be determined from Equation 6-16.

Degree of saturation:

- Moist subsaturated air: The degree of saturation (μ_d) for subsaturated air is given by

$$\mu_d = \frac{W_m}{W_s} \quad (6-57)$$

where W_m is the humidity ratio of the given moist air sample and W_s is the humidity ratio of saturated air at the same temperature and pressure. The degree of saturation may have a value between 0 and 1 for air in the subsaturated zone.

- **Moist supersaturated air:** The degree of saturation ($\mu_{d,super}$) for supersaturated can be expressed as

$$\mu_{d,super} = \frac{W_{super}}{W_s} \quad (6-58)$$

The degree of saturation for supersaturated air has a value larger than 1.

Results

A sample collection of property data under supersaturated conditions in the temperature range -40°C to 40°C and humidity ratios between 0 and 0.1 kg/kg_a is shown in Table 6-4. The data presented include the specific volume, specific enthalpy, specific entropy, and humidity ratio for degrees of saturation from 100% to 200%. These properties are determined at atmospheric pressure and are presented in two psychrometric charts: one for temperatures from -40°C to 0°C , and the other from 0°C to 40°C (Figures 6-1 and 6-2). Properties of saturated air determined in this chapter have a maximum deviation of $\pm 0.1\%$ compared to the data developed by Hyland and Wexler (1983a, b).

Figure 6-1 shows the psychrometric chart for temperatures from -40°C to 0°C and for humidity ratios between 0 and $0.0076 \text{ kg}_w/\text{kg}_a$, while Figure 6-2 shows the psychrometric chart for temperatures from 0°C to 40°C and for humidity ratios between 0 to $0.1 \text{ kg}_w/\text{kg}_a$. In these figures, lines of constant enthalpy, degree of saturation, humidity ratio, dry-bulb temperature, and specific volume are represented in the supersaturated zone of the psychrometric chart.

Figures 6-3 and 6-4 show examples of state points placed on the psychrometric chart. For example, if the dry-bulb temperature is 16°C and the degree of saturation is 150% for Point 1, the specific enthalpy, humidity ratio, and the specific volume can be determined using Figure 6-1. This yields a specific enthalpy of -13.963 kJ/kg , a humidity ratio of $0.001396 \text{ kg}_w/\text{kg}_a$, and specific volume of $0.729 \text{ m}^3/\text{kg}$. In a similar manner, for a dry-bulb temperature of -4°C and a humidity ratio of $0.002979 \text{ kg}_w/\text{kg}_a$ for Point 2, the other properties can be determined from the same chart. This yields a degree of saturation of 110%, a specific enthalpy of -2.635 kJ/kg , and a specific volume of $0.7653 \text{ m}^3/\text{kg}$. These two points are represented in Figure 6-3.

Similarly, using Figure 6-2, if the dry-bulb temperature is 8°C and the degree of saturation is 120% for Point 3, the specific enthalpy, humidity ratio, and the specific volume can be determined. This gives a specific enthalpy of -24.897 kJ/kg , a humidity ratio of $0.00802 \text{ kg}_w/\text{kg}_a$, and a specific volume of $0.8046 \text{ m}^3/\text{kg}$. An example at higher temperatures is represented by Point 4, which has a dry-bulb temperature of 22°C and a humidity ratio of $0.02679 \text{ kg}_w/\text{kg}_a$. After locating this point on the chart, the properties can be read as degree of saturation of 160%, specific enthalpy of -65.587 kJ/kg , and specific volume of $0.8531 \text{ m}^3/\text{kg}$.

Conclusions

Psychrometric data for supersaturated air have been developed and presented in the form of psychrometric charts for degrees of saturation from 100% to 200%. This method extends the current psychrometric data, which are presently only available in the subsaturated zone of the psychrometric chart. The properties developed in this

investigation should enable the refrigeration engineer and system designer to better predict the performance of the system as well as design a more optimal system.

Table 6-4. Thermodynamic properties of moist supersaturated air (standard atmospheric pressure, 101325 Pa)

t (°C)	$\mu_d = 100\%$				$\mu_{d, \text{super}} = 120\%$			
	W_s (kg _w /kg _a)	v_s (m ³ /kg)	i_s (kJ/kg)	s_s (kJ/kg K)	W_{super} (kg _w /kg _a)	v_{super} (m ³ /kg)	i_{super} (kJ/kg)	s_{super} (kJ/kg K)
-40	0.0000793	0.659700	-40.229	-0.1584	0.0000952	0.659700	-40.236	-0.1584
-38	0.0000992	0.665400	-37.976	-0.1496	0.0001190	0.665400	-37.984	-0.1496
-36	0.0001237	0.671200	-35.905	-0.1408	0.0001484	0.671200	-35.915	-0.1408
-34	0.0001536	0.676900	-33.820	-0.1320	0.0001843	0.676900	-33.832	-0.1320
-32	0.0001902	0.682600	-31.718	-0.1233	0.0002282	0.682600	-31.733	-0.1234
-30	0.0002346	0.688400	-29.597	-0.1145	0.0002815	0.688400	-29.615	-0.1146
-28	0.0002883	0.694100	-27.454	-0.1057	0.0003460	0.694100	-27.476	-0.1058
-26	0.0003533	0.699900	-25.282	-0.0969	0.0004240	0.699900	-25.309	-0.0970
-24	0.0004314	0.705700	-23.078	-0.0880	0.0005177	0.705700	-23.111	-0.0881
-22	0.0005251	0.711500	-20.834	-0.0790	0.0006301	0.711500	-20.874	-0.0791
-20	0.0006373	0.717300	-18.545	-0.0699	0.0007648	0.717300	-18.593	-0.0701
-18	0.0007711	0.723100	-16.201	-0.0607	0.0009253	0.723100	-16.258	-0.0609
-16	0.0009303	0.729000	-13.793	-0.0513	0.0011164	0.729000	-13.861	-0.0516
-14	0.0011191	0.734900	-11.311	-0.0416	0.0013429	0.734900	-11.392	-0.0419
-12	0.0013425	0.740900	-8.742	-0.0318	0.0016110	0.740900	-8.838	-0.0322
-10	0.0016062	0.746900	-6.072	-0.0215	0.0019274	0.746900	-6.186	-0.0219
-8	0.0019166	0.753000	-3.283	-0.0100	0.0022999	0.753000	-3.417	-0.0105
-6	0.0022811	0.759100	-0.357	0.0000	0.0027373	0.759100	-0.515	-0.0006
-4	0.0027081	0.765300	2.728	0.0115	0.0032487	0.765301	2.543	0.0108
-2	0.0032074	0.771700	5.995	0.0236	0.0038499	0.771701	5.778	0.0228
0	0.0037895	0.778100	9.473	0.0364	0.0045474	0.778101	9.220	0.0355
0	0.0037895	0.778100	9.473	0.0364	0.0045474	0.778101	9.479	0.0364
2	0.0043810	0.784500	12.982	0.0492	0.0052572	0.784501	12.989	0.0492
4	0.0050540	0.791100	16.696	0.0627	0.0060648	0.791101	16.713	0.0628
6	0.0058180	0.797800	20.644	0.0769	0.0069816	0.797801	20.673	0.0770
8	0.0066830	0.804600	24.852	0.0919	0.0080196	0.804601	24.897	0.0921
10	0.0076610	0.811600	29.352	0.1078	0.0091932	0.811602	29.416	0.1080
12	0.0087660	0.818800	34.179	0.1248	0.0105192	0.818802	34.267	0.1251
14	0.0100120	0.826200	39.370	0.1430	0.0120144	0.826202	39.488	0.1434
16	0.0114130	0.833800	44.963	0.1620	0.0136956	0.833802	45.116	0.1625
18	0.0129890	0.841700	51.008	0.1830	0.0155868	0.841703	51.204	0.1837
20	0.0147580	0.849800	57.555	0.2060	0.0177096	0.849803	57.803	0.2069
22	0.0167410	0.858300	64.660	0.2300	0.0200892	0.858303	64.969	0.2311
24	0.0189630	0.867100	72.385	0.2560	0.0227556	0.867104	72.767	0.2573
26	0.0214480	0.876400	80.798	0.2840	0.0257376	0.876404	81.266	0.2856
28	0.0242260	0.886000	89.976	0.3150	0.0290712	0.886005	90.545	0.3170
30	0.0273290	0.896200	100.006	0.3480	0.0327948	0.896205	100.694	0.3504
32	0.0307930	0.906900	110.979	0.3840	0.0369516	0.906906	111.805	0.3869
34	0.0346600	0.918300	123.011	0.4240	0.0415920	0.918307	123.999	0.4274
36	0.0389710	0.930300	136.209	0.4670	0.0467652	0.930308	137.384	0.4710
38	0.0437780	0.943100	150.713	0.5140	0.0525336	0.943109	152.107	0.5188
40	0.0491410	0.956800	166.683	0.5650	0.0589692	0.956810	168.329	0.5706

Table 6-4. Continued.

t (°C)	$\mu_{d,super} = 140\%$				$\mu_{d,super} = 160\%$			
	W_{super} (kg _w /kg _a)	v_{super} (m ³ /kg)	i_{super} (kJ/kg)	s_{super} (kJ/kg K)	W_{super} (kg _w /kg _a)	v_{super} (m ³ /kg)	i_{super} (kJ/kg)	s_{super} (kJ/kg K)
-40	0.0001110	0.659700	-40.242	-0.1584	0.0001269	0.659700	-40.249	-0.1585
-38	0.0001389	0.665400	-37.992	-0.1497	0.0001587	0.665400	-38.000	-0.1497
-36	0.0001732	0.671200	-35.925	-0.1409	0.0001979	0.671200	-35.935	-0.1409
-34	0.0002150	0.676900	-33.845	-0.1321	0.0002458	0.676900	-33.857	-0.1321
-32	0.0002663	0.682600	-31.748	-0.1234	0.0003043	0.682600	-31.763	-0.1235
-30	0.0003284	0.688400	-29.634	-0.1146	0.0003754	0.688400	-29.652	-0.1147
-28	0.0004036	0.694100	-27.499	-0.1059	0.0004613	0.694100	-27.521	-0.1059
-26	0.0004946	0.699900	-25.336	-0.0971	0.0005653	0.699900	-25.364	-0.0972
-24	0.0006040	0.705700	-23.144	-0.0882	0.0006902	0.705700	-23.177	-0.0884
-22	0.0007351	0.711500	-20.913	-0.0793	0.0008402	0.711500	-20.953	-0.0794
-20	0.0008922	0.717300	-18.640	-0.0703	0.0010197	0.717300	-18.688	-0.0704
-18	0.0010795	0.723100	-16.315	-0.0611	0.0012338	0.723101	-16.372	-0.0613
-16	0.0013024	0.729000	-13.929	-0.0518	0.0014885	0.729001	-13.997	-0.0521
-14	0.0015667	0.734900	-11.473	-0.0422	0.0017906	0.734901	-11.554	-0.0425
-12	0.0018795	0.740901	-8.934	-0.0325	0.0021480	0.740901	-9.030	-0.0329
-10	0.0022487	0.746901	-6.300	-0.0223	0.0025699	0.746901	-6.413	-0.0228
-8	0.0026832	0.753001	-3.551	-0.0110	0.0030666	0.753001	-3.685	-0.0115
-6	0.0031935	0.759101	-0.673	-0.0012	0.0036498	0.759101	-0.830	-0.0017
-4	0.0037913	0.765301	2.358	0.0101	0.0043330	0.765302	2.173	0.0095
-2	0.0044904	0.771701	5.562	0.0220	0.0051318	0.771702	5.345	0.0212
0	0.0053053	0.778102	8.968	0.0345	0.0060632	0.778102	8.715	0.0336
0	0.0053053	0.778102	9.486	0.0364	0.0060632	0.778102	9.492	0.0364
2	0.0061334	0.784502	12.997	0.0493	0.0070096	0.784503	13.004	0.0493
4	0.0070756	0.791102	16.730	0.0628	0.0080864	0.791103	16.747	0.0629
6	0.0081452	0.797802	20.703	0.0771	0.0093088	0.797803	20.732	0.0772
8	0.0093562	0.804603	24.942	0.0922	0.0106928	0.804604	24.987	0.0924
10	0.0107254	0.811603	29.481	0.1083	0.0122576	0.811605	29.545	0.1085
12	0.0122724	0.818804	34.356	0.1254	0.0140256	0.818805	34.444	0.1257
14	0.0140168	0.826204	39.605	0.1438	0.0160192	0.826206	39.723	0.1443
16	0.0159782	0.833805	45.270	0.1631	0.0182608	0.833807	45.423	0.1636
18	0.0181846	0.841705	51.401	0.1844	0.0207824	0.841708	51.597	0.1851
20	0.0206612	0.849806	58.051	0.2077	0.0236128	0.849809	58.298	0.2086
22	0.0234374	0.858307	65.278	0.2322	0.0267856	0.858310	65.587	0.2333
24	0.0265482	0.867108	73.149	0.2587	0.0303408	0.867111	73.531	0.2600
26	0.0300272	0.876409	81.733	0.2873	0.0343168	0.876413	82.201	0.2889
28	0.0339164	0.886010	91.114	0.3190	0.0387616	0.886015	91.682	0.3209
30	0.0382606	0.896211	101.381	0.3528	0.0437264	0.896216	102.069	0.3552
32	0.0431102	0.906112	112.631	0.3897	0.0492688	0.906119	113.457	0.3926
34	0.0485240	0.918314	124.987	0.4308	0.0554560	0.918321	125.974	0.4342
36	0.0545594	0.930316	138.560	0.4751	0.0623536	0.930324	139.735	0.4791
38	0.0612892	0.943118	153.501	0.5236	0.0700448	0.943126	154.895	0.5283
40	0.0687974	0.956820	169.975	0.5763	0.0786256	0.956830	171.622	0.5819

Table 6-4. Continued.

t (°C)	$\mu_{d,super} = 180\%$				$\mu_{d,super} = 200\%$			
	W_{super} (kg _m /kg _a)	v_{super} (m ³ /kg)	i_{super} (kJ/kg)	s_{super} (kJ/kg K)	W_{super} (kg _m /kg _a)	v_{super} (m ³ /kg)	i_{super} (kJ/kg)	s_{super} (kJ/kg K)
-40	0.0001427	0.659700	-40.255	-0.1585	0.0001586	0.659700	-40.262	-0.1585
-38	0.0001786	0.665400	-38.008	-0.1497	0.0001984	0.665400	-38.016	-0.1498
-36	0.0002227	0.671200	-35.945	-0.1409	0.0002474	0.671200	-35.955	-0.1410
-34	0.0002765	0.676900	-33.869	-0.1322	0.0003072	0.676900	-33.882	-0.1322
-32	0.0003424	0.682600	-31.778	-0.1235	0.0003804	0.682600	-31.794	-0.1236
-30	0.0004223	0.688400	-29.671	-0.1148	0.0004692	0.688400	-29.689	-0.1148
-28	0.0005189	0.694100	-27.544	-0.1060	0.0005766	0.694100	-27.566	-0.1061
-26	0.0006359	0.699900	-25.391	-0.0973	0.0007066	0.699900	-25.418	-0.0974
-24	0.0007765	0.705700	-23.210	-0.0885	0.0008628	0.705700	-23.243	-0.0886
-22	0.0009452	0.711500	-20.993	-0.0796	0.0010502	0.711501	-21.032	-0.0797
-20	0.0011471	0.717301	-18.736	-0.0706	0.0012746	0.717301	-18.783	-0.0708
-18	0.0013880	0.723101	-16.429	-0.0615	0.0015422	0.723101	-16.486	-0.0617
-16	0.0016745	0.729001	-14.065	-0.0523	0.0018606	0.729001	-14.134	-0.0526
-14	0.0020144	0.734901	-11.635	-0.0428	0.0022382	0.734901	-11.716	-0.0431
-12	0.0024165	0.740901	-9.127	-0.0332	0.0026850	0.740901	-9.223	-0.0336
-10	0.0028912	0.746901	-6.527	-0.0232	0.0032124	0.746902	-6.641	-0.0236
-8	0.0034499	0.753002	-3.820	-0.0120	0.0038332	0.753002	-3.954	-0.0125
-6	0.0041060	0.759102	-0.988	-0.0023	0.0045622	0.759102	-1.146	-0.0029
-4	0.0048746	0.765302	1.987	0.0088	0.0054162	0.765303	1.802	0.0081
-2	0.0057733	0.771703	5.129	0.0204	0.0064148	0.771703	4.912	0.0196
0	0.0068211	0.778103	8.462	0.0327	0.0075790	0.778104	8.210	0.0318
0	0.0068211	0.778103	9.498	0.0364	0.0075790	0.778104	9.505	0.0364
2	0.0078858	0.784504	13.011	0.0493	0.0087620	0.784504	13.019	0.0493
4	0.0090972	0.791104	16.764	0.0629	0.0101080	0.791105	16.781	0.0630
6	0.0104724	0.797805	20.761	0.0773	0.0116360	0.797806	20.790	0.0774
8	0.0120294	0.804605	25.032	0.0925	0.0133660	0.804607	25.076	0.0927
10	0.0137898	0.811606	29.609	0.1087	0.0153220	0.811608	29.674	0.1090
12	0.0157788	0.818807	34.532	0.1261	0.0175320	0.818809	34.621	0.1264
14	0.0180216	0.826208	39.841	0.1447	0.0200240	0.826210	39.959	0.1451
16	0.0205434	0.833809	45.576	0.1642	0.0228260	0.833811	45.730	0.1647
18	0.0233802	0.841710	51.793	0.1858	0.0259780	0.841713	51.989	0.1865
20	0.0265644	0.849812	58.546	0.2095	0.0295160	0.849815	58.794	0.2104
22	0.0301338	0.858313	65.896	0.2344	0.0334820	0.858317	66.205	0.2354
24	0.0341334	0.867115	73.913	0.2614	0.0379260	0.867119	74.295	0.2627
26	0.0386064	0.876417	82.668	0.2905	0.0428960	0.876422	83.136	0.2922
28	0.0436068	0.886019	92.251	0.3229	0.0484520	0.886024	92.820	0.3249
30	0.0491922	0.896222	102.756	0.3575	0.0546580	0.896227	103.444	0.3599
32	0.0554274	0.909625	114.282	0.3954	0.0615860	0.909631	115.108	0.3983
34	0.0623880	0.918328	126.962	0.4376	0.0693200	0.918335	127.950	0.4410
36	0.0701478	0.930331	140.910	0.4832	0.0779420	0.930339	142.086	0.4872
38	0.0788004	0.943135	156.289	0.5331	0.0875560	0.943144	157.682	0.5379
40	0.0884538	0.956840	173.268	0.5875	0.0982820	0.956850	174.914	0.5931

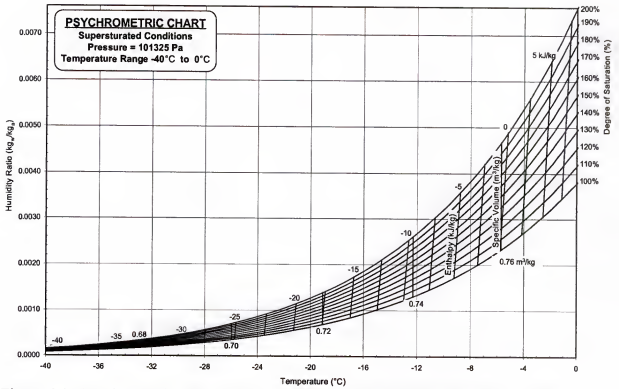


Figure 6-1. Psychrometric chart in the supersaturated zone for a temperature range from -40 to 0 $^{\circ}\text{C}$

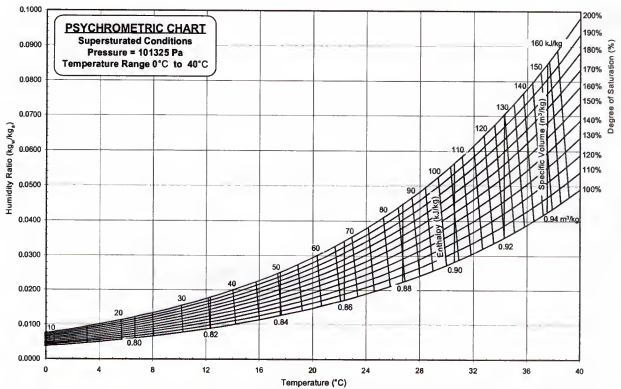


Figure 6-2. Psychrometric chart in the supersaturated zone for a temperature range from 0 to 40 $^{\circ}\text{C}$

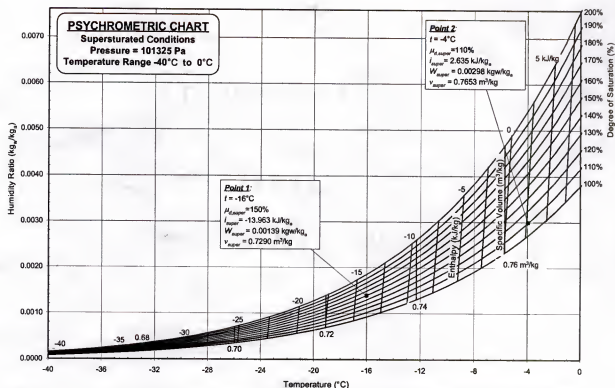


Figure 6-3. Psychrometric chart in the supersaturated zone for a temperature range from -40 to 0 $^\circ\text{C}$, showing two sample points

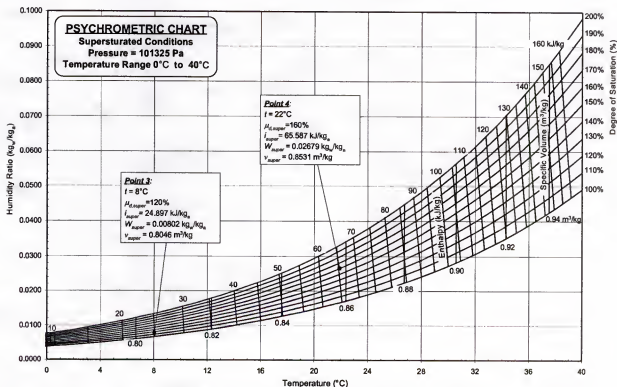


Figure 6-4. Psychrometric chart in the supersaturated zone for a temperature range from 0 to 40 $^\circ\text{C}$, showing two sample points

CHAPTER 7

HEAT AND MASS TRANSFER ON A CYLINDER SURFACE IN CROSS FLOW UNDER SUPERSATURATED FROSTING CONDITIONS

Objectives

This chapter presents a calculation procedure for a cylinder surface exposed to supersaturated air. In this procedure the psychrometric formulations for supersaturated moist air will be used to predict frost formation and heat transfer rates on the cylinder surface in question. The cylinder surface was selected because it could represent the tube in a freezer coil. While this is not identical to a finned-tube freezer coil per se, it serves as an illustration of how the techniques developed here can be utilized to predict the performance of a real freezer coil in the supersaturated zone of the psychrometric chart. This geometry has also been selected so that results of the supersaturated model could be compared to other published works in the subsaturated zone of the psychrometric chart, such as Andrichak (1962), Chung and Algren (1958a, b), and Parish and Sepsy (1972), among others. This comparison is crucial, as the characteristics of the frost-formation process under supersaturated conditions should be referenced to those of a frosted surface with a predictable performance (e.g., under subsaturated conditions).

The calculation procedure developed here simulates the frost-formation process as a quasi-steady-state one. In a quasi-steady-state approach, time-dependent phenomena are treated as steady-state ones for sufficiently small time intervals. In other words, the overall solution is treated as a collection of a series of steady-state solutions at different time increments. So, while only steady-state equations are employed, the overall solution

is time-dependent. The accuracy of this approach can be almost as high as the real-time solution of the time-dependent problem provided that the time increment chosen is sufficiently small. The size of the time step is experimented with and sensitivity of the solution to the step size will be established and checked.

The problem of frost formation on cylinders in cross flow is a complicated one because of the following factors:

- The boundary layer solution is transient. The thermal resistance of the frost layer changes with both time and position when the frost layer is growing in thickness. Therefore the frost surface temperature also changes with time and position. The thermal and diffusion boundary layers also change, resulting in a change in the heat and mass transfer coefficients with time.
- The frost density and thermal conductivity (parameters needed in the modeling) vary continuously during the development of the frost layer, although eventually a quasi-steady state is achieved.
- The frost-formation process involves simultaneous heat and mass transfer. The model presented in this chapter employs empirical correlations for heat and mass transfer for flow past a circular cylinder. The frost layer is not uniform around the cylinder during the formation process, which complicates the situation due to the fact that the geometry is no longer a cylindrical one.
- There is no unique behavior for the heat and mass transfer coefficients past the separation point (Giedt 1949). Thus the complexity of the modeling effort is expected to be significantly higher in that region.

For the reasons mentioned above, modeling of this problem will be carried out using two methods. First, the frost will be assumed to grow uniformly around the cylinder, thus neglecting the angular dependency of the variables. This allows the employment of empirical correlations for the average heat and mass transfer coefficients. The second method accounts for the angular dependency using local properties as well as the local heat and mass transfer coefficients. This part of the analysis will be performed only from the stagnation point to the separation point. This would allow the prediction of the spatial and temporal variations of the frost thickness and temperature.

Analysis

As was mentioned earlier, the analysis presented here is a quasi-steady state one, whereby steady state conditions are allowed to exist for sufficiently small intervals of time. The analysis presented will illustrate a mechanism for computing the frost formation and heat transfer rates as functions of both time and angular position on the cylinder surface. Use is made of empirical correlations for the heat transfer coefficient and for frost properties. A section of the cylinder used is shown in Figure 7-1.

The energy balance at any angular position on a small area segment on the cylinder surface (Figure 7-1) in the vicinity of the angular position (θ), can be written as follows:

$$\delta\dot{Q}_{conv,\theta} + \delta\dot{Q}_{diff,\theta} - \delta\dot{Q}_{cond,\theta} = 0 \quad (7-1)$$

where $\delta\dot{Q}_{conv,\theta}$, $\delta\dot{Q}_{diff,\theta}$, and $\delta\dot{Q}_{cond,\theta}$ are the heat transfer rates by convection, due to mass diffusion, and by conduction, respectively, to the finite segment of the cylinder surface in the vicinity of the angular position θ .

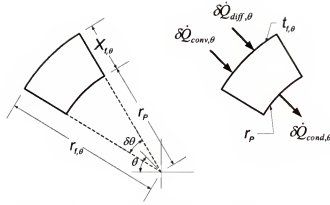


Figure 7-1. Small area segment on the cylinder surface in the vicinity of the angular position (θ)

The rate of heat convected can be determined from

$$\delta \dot{Q}_{conv,\theta} = h_{c,o,\theta} \lambda r_{f\theta} (t_m - t_{f\theta}) \delta \theta \quad (7-2)$$

where $h_{c,o,\theta}$, $t_{f\theta}$, and $r_{f\theta}$ are the heat transfer coefficient, the frost surface temperature, and frosted cylinder radius at angular position θ , respectively, and where λ and t_m are the cylinder length and the temperature of the free stream moist air, respectively. The quantity $\delta \theta$ represents a small but finite angular deviation around θ .

The local Nusselt number (Nu_θ) and heat transfer coefficient ($h_{c,o,\theta}$) over the forward portion of the cylinder ($0 < \theta < 80^\circ$) can be determined employing the equation proposed by Martinelli et al. (1943)

$$Nu_\theta = \frac{h_{c,o,\theta} (2r_{f\theta})}{k_{super}} = 1.14 Re_{Df,super}^{0.5} Pr_{super}^{0.4} \left[1 - \left(\frac{\theta}{90} \right)^3 \right] \quad (7-3)$$

where k_{super} is the thermal conductivity of supersaturated air, while $Re_{Df,super}$ and Pr_{super} are the Reynolds and Prandtl numbers evaluated under supersaturated conditions, respectively.

The heat transfer rate due to mass diffusion is given by

$$\delta \dot{Q}_{diff,\theta} = \lambda r_{f\theta} L_{s,\theta} h_{mass,\theta} (W_m - W_{f\theta}) \delta \theta \quad (7-4)$$

where $h_{mass,\theta}$ and $W_{f\theta}$ are the local mass transfer coefficient and the humidity ratio of air evaluated at $t_{f\theta}$ (assuming saturation conditions in the vicinity of the air-frost interface), respectively, and where $L_{s,\theta}$ and W_m are the latent heat of sublimation of the frost and the humidity ratio of the free stream moist air.

The humidity ratio of the free stream moist air (W_m) can be determined from (ASHRAE 2001)

$$W_m = \frac{m_w}{m_a} = 0.62198 \frac{\varepsilon(P_s \phi)}{P - \varepsilon(P_s \phi)} \quad (7-5)$$

where m_w and m_a are the mass of water vapor in air and the mass of dry air, respectively, P_s is the saturation pressure of the water vapor, P is the total pressure, ϕ is the relative humidity of the air, and ε is the enhancement factor, which can be determined from Equation 6-52.

Equation 7-4 can be modified to determine the diffusion-driven heat transfer rate under supersaturated conditions replacing W_m with the humidity ratio of supersaturated air (W_{super}), which can be expressed as follows:

$$W_{super} = \frac{m_{ws} + m_{drop}}{m_a} = W_s + \frac{m_{drop}}{m_a} \quad (7-6)$$

where (W_s) is the humidity ratio of air at saturation and m_{drop} is the mass of excess moisture beyond saturation (either liquid or ice, depending on whether the dry bulb temperature of the air is above or below the water freezing point, respectively).

The local latent heat of sublimation for frost can be determined from (modified from Parish 1970)

$$L_{s,\theta} = [-0.1083(1.8t_{f\theta} + 32) + 2833] \quad (7-7)$$

where $L_{s,\theta}$ in Equation 7-7 is expressed in J/kg.

The local mass transfer coefficient at any angular position θ can be determined as follows:

$$h_{mass,\theta} = \frac{h_{c,o,\theta}}{C_{p,sup er} Le^{2/3}} \quad (7-8)$$

The Lewis number is a relevant parameter to situations involving simultaneous heat and mass transfer. It is defined as

$$Le = \frac{\alpha_{sup er}}{D_{diff}} \quad (7-9)$$

The mass diffusion coefficient can be determined in terms of the molecular weights and molar volumes of the dry air and water vapor (Holman 1997)

$$D_{diff} = 0.04357 (T_a)^{3/2} \frac{[(1/M_a) + (1/M_v)]}{P_{atm} (\forall_a^{1/3} + \forall_v^{1/3})^2} \quad (7-10)$$

where D_{diff} is in m^2/s , P_{atm} is in Pa, M_a and M_v are the molecular weights of dry air (28.9) and water vapor (18), respectively, and, \forall_a and \forall_v are the molar volumes of dry air (29.9) and water vapor (18.8), respectively.

The rate of heat transfer by conduction is determined using the Fourier's heat conduction equation

$$\dot{Q}_{cond,\theta} = \frac{k_{f\theta} \lambda (t_{f\theta} - t_p)}{Log_e(r_{f\theta}/r_p)} \delta\theta \quad (7-11)$$

where $k_{f\theta}$ is the local thermal conductivity of frost.

There are several equations to determine the frost density and thermal conductivity, but for the purpose of this analysis only two of them are used. For the frost density ($\rho_{f\theta}$) an empirical expression proposed by Hayashi et al. (1977) is applied. This expression is a sole function of the frost surface temperature as follows:

$$\rho_{f\theta} = 650 \exp(0.227 t_{f\theta}) \quad (7-12)$$

where $\rho_{f\theta}$ is in kg/m^3 . This equation should be applied under the following conditions: frost surface temperature between -25°C and 0°C ; airstream velocities between 2m/s and 6 m/s, and airstream humidity ratio equal to $0.0075 \text{ kg}_w/\text{kg}_a$. While these conditions are a bit restrictive for supersaturated air, it was felt that the error resulting from using the correlation at slightly higher humidity ratios than the ones suggested by Hayashi et al. (1977) may be partially compensated for by the fact that the frost surface temperature in a supersaturated air scenario would necessarily be higher than the corresponding frost surface temperature in a subsaturated air scenario, assuming everything else being unchanged. Higher frost surface temperatures produce higher frost densities, a fact consistent with experimental observations made by Sherif et al. (2002) for snow-like frost resulting from a supersaturated air scenario. It is thus argued that the manner with which the density is made dependent on the frost surface temperature in Equation 7-12 should make the use of the equation justified.

For the frost thermal conductivity ($k_{f\theta}$), an empirical correlation proposed by Yonko and Sepsy (1967) is applied. This correlation is given by the following equation:

$$k_{f\theta} = 0.024248 + (0.00072311 \rho_{f\theta}) + (0.000001183 \rho_{f\theta}^2) \quad (7-13)$$

where $\rho_{f\theta}$ is in kg/m^3 and $k_{f\theta}$ is expressed in W/(m-K) . The above equation is only valid for frost densities less than 573 kg/m^3 . This limiting value of the frost density is likely to be a good upper bound for some of the most severe scenarios observed in a parallel experimental investigation performed by the authors when supersaturated frost deposition was taking place. Thus, it was felt that the use of Equation 7-13 is justified.

The local frost deposition rate per unit area can now be computed using

$$\dot{m}_{f,\theta} = h_{\text{mass},\theta} (W_m - W_{f\theta}) \quad (7-14)$$

While the local increase in frost thickness can be computed from

$$\Delta X_{f,\theta} = \frac{\dot{m}_{f,\theta} \Delta \tau}{\rho_{f\theta}} \quad (7-15)$$

where $\Delta \tau$ is the time increment during which steady state conditions were assumed to exist to make the quasi-steady state assumption valid.

The new frost thickness at the new time is related to that at the previous time according to the equation

$$X_{f,\theta} = X_{f,\theta} + \Delta X_{f,\theta} \quad (7-16)$$

The frost surface temperature can now be obtained by substituting Equations 7-2, 7-4, and 7-11 into Equation 7-1 to yield

$$t_{f\theta} = \frac{h_{c,\rho,\theta} r_{f\theta} \text{Log}_e(r_{f\theta}/r_p) + k_{f\theta} t_p + L_{i,\theta} r_{f\theta} h_{\text{mass},\theta} (W_m - W_{f\theta}) \text{Log}_e(r_{f\theta}/r_p)}{h_{c,\rho,\theta} r_{f\theta} \text{Log}_e(r_{f\theta}/r_p) + k_{f\theta}} \quad (7-17)$$

The calculation procedure can proceed as follows: the time and the frost thickness ($X_{f\theta}$) are first initialized to zero, and the frost surface temperature ($t_{f\theta}$) is set equal to that of the cylinder surface (t_p). Air properties are evaluated at the air-frost boundary layer film temperature. Using Equations 7-3 and 7-8 the local heat and mass

transfer coefficients are computed. Equations 7-12, 7-13, and 7-14 are then used to determine the frost density, frost thermal conductivity, and the mass deposition rate per unit area, respectively. The increase in frost thickness and the new frost thickness can then be computed using Equations 7-15 and 7-16, respectively. Using the parameters determined above, a first approximation for the frost surface temperature is determined employing Equation 7-17. This approximate value of t_{f0} , is then used to determine the new boundary layer film temperature in order to re-compute the local heat and mass transfer coefficients, the local frost density and thermal conductivity, as well as a new approximate value for the frost surface temperature. This calculation procedure is repeated until the value of the new frost surface temperature computed is within a difference of 0.0001°C of the previous value. A numerical procedure describing the flow of calculations is illustrated in Figure 7-2.

A more simplified set of equations, whereby the angular dependency of the variables is neglected (implying that the frost is uniformly building up on the surface), can be employed if the average heat and mass transfer coefficients are used in lieu of the local coefficients. For example, Churchill and Bernstein (1977) proposed the following formula for the average Nusselt number:

$$Nu_o = 0.3 + \frac{0.62 Re_{Df,super}^{1/2} Pr_{super}^{1/3}}{\left(1 + (0.4/Pr_{super})^{2/3}\right)^{1/4}} \left(1 + \left(\frac{Re_{Df,super}}{282000}\right)^{5/8}\right)^{4/5} = \frac{h_{c,o} D_f}{k_{super}} \quad (7-18)$$

This equation is recommended for $(Re_{Df,super} Pr_{super}) > 0.2$, where all the properties are evaluated at the film temperature between the air and the frost surface. All other equations remain the same provided that variables with angle dependency are replaced with their average values integrated over the whole cylinder.

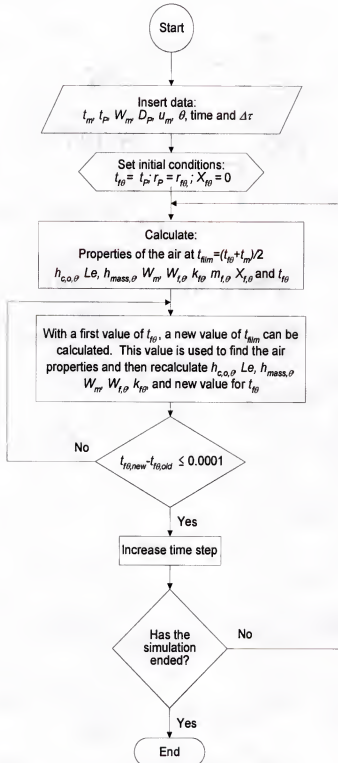


Figure 7-2. Flow chart of the numerical procedure used

Results and Discussion

The procedure described in the previous section was applied to cylinders under forced convection for both subsaturated and supersaturated air, and comparisons with experimental data were made whenever possible. However, before generating results from the model, the stability of the solution was checked in terms of its dependence on the time step. This check is important as we do not want the results to depend on the size of the time step. That dependence is shown in Figure 7-3, which shows the variation of the frost thickness with time for three values of the time step. As can be seen, there are no discernable differences among the three cases.

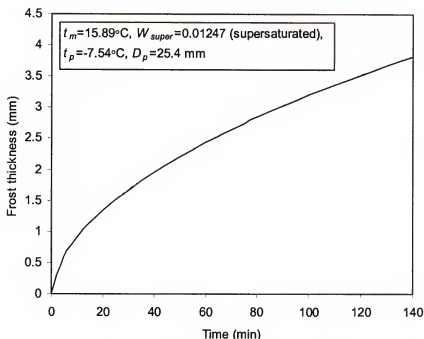


Figure 7-3. Effect of the time step on the stability of the solution: — $\Delta\tau=1s$, $\Delta\tau=3s$, and ---- $\Delta\tau=5s$

For all further results shown in this chapter, the time step used is one second. This means that steady state conditions were assumed to exist for periods of one second at a time. Once the solution converged at a particular point in time, the generated results were used as initial conditions for the subsequent point in time.

Figures 7-4 and 7-5 show the variation of the frost thickness with time for both subsaturated and supersaturated air at the stagnation point and at the separation point (corresponding to angular position of 80°), respectively. Results of the present model are compared with those of Andrichak (1962) and Parish and Sepsy (1972) for the subsaturated cases. As can be seen, results from the present model agree well with those of other researchers. The difference in thickness for supersaturated and subsaturated conditions is notable, considering the small span of time during which frost thickness is computed. Comparing Figures 7-4 and 7-5, it is easy to observe that the frost thickness at the stagnation point is higher than that at the separation point, with all other variables remaining unchanged.

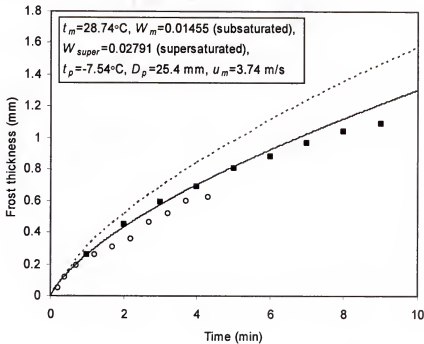


Figure 7-4. Variation of the frost thickness with time at the stagnation point: — present work (subsaturated conditions), ■ Andrichak (1962), ○ Parish and Sepsy (1972), ---- present work (supersaturated conditions)

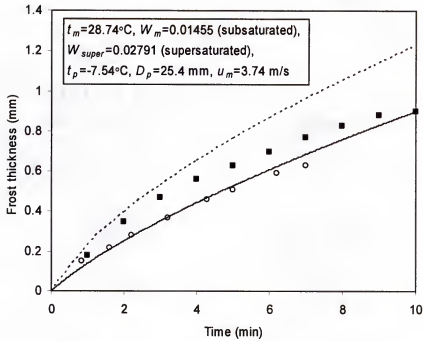


Figure 7-5. Variation of the frost thickness with time at the separation point: — present work (subsaturated conditions), ■ Adrichack (1962), ○ Parish and Sepsy (1972), ---- present work (supersaturated conditions)

Figures 7-6 and 7-7 show the variation of the frost surface temperature and frost thickness with angular position from the stagnation point to the separation point, respectively, for two different times. Results of the present model are compared with those of Raju and Sherif (1993) for times of 3 and 6 minutes. As can be seen, results from the present model agree well with those of Raju and Sherif (1993). Other researchers have shown that the heat and mass transfer rates decrease as the angular position changes from the stagnation point to the separation point (Schmidt and Wenner 1941 and Giedt 1949).

This study also includes results where the angular dependency of the variables is neglected (implying that the frost is uniformly building up on the surface). Figure 7-8 shows the effect of the Reynolds number on the frost thickness for subsaturated and supersaturated air scenarios.

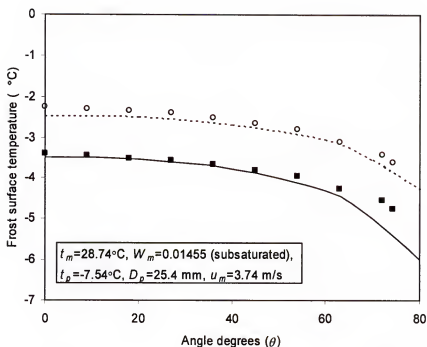


Figure 7-6. Variation of the frost surface temperature with the angle (θ) for different times: a) 3 min: — present work and ■ Raju and Sherif (1993), b) 6 min: ---- present work and ○ Raju and Sherif (1993)

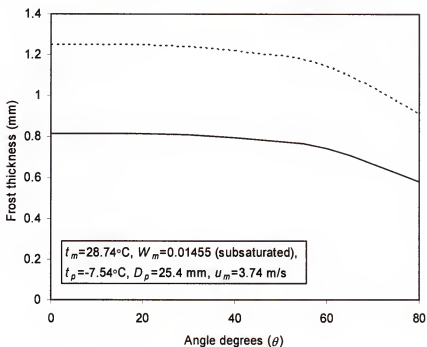


Figure 7-7. Variation of the frost thickness with the angle (θ) for different times: a) 3 min: — present work and b) 6 min: ---- present work

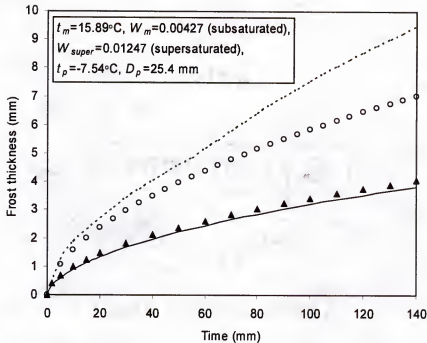


Figure 7-8. Effect of the Reynolds number on the frost thickness: a) $Re=2592$: — subsaturated conditions, \circ supersaturated conditions, and b) $Re=9965$: \blacktriangle subsaturated conditions and ---- supersaturated conditions

A close examination of the figure reveals the significant differences between the frost thickness at a certain point in time for subsaturated air versus supersaturated air. It is natural to expect that there would be more frost when the air is supersaturated. It is also natural to expect a larger thickness for higher Reynolds numbers. Observations made earlier in this investigation confirm these results. Sherif et al. (1993) made some interesting observations regarding the Reynolds number dependency. They argued that there are two opposing mechanisms at play vis-à-vis the Reynolds number. While a higher Reynolds number is associated with a higher free stream velocity and a correspondingly higher film heat transfer coefficient, higher Reynolds numbers also result in a higher frost-air interface temperature (see Figure 7-9). For a constant free-stream air temperature, the temperature driving force between the free stream air and the cylinder surface is reduced as the Reynolds number is increased, resulting in a lower heat

transfer rate. This seems to reduce the overall positive effect of a higher Reynolds number from a heat transfer rate vantage point. Sherif et al. (1993) also argued that the reduced temperature difference driving force is associated with a reduced humidity ratio difference driving force, which results in a reduction in the frost deposition rate. This contributes to the tapering off of the frost thickness-time curves shown in Figure 7-8 as time increases. An examination of this phenomenon for supersaturated air cases indicates that the effect in question is less pronounced than in subsaturated air cases. This may be an intuitive result given the fact that frost formation in supersaturated air is driven by both diffusion and convection and is thus less susceptible to being affected by a single variable such as the Reynolds number.

In order to verify the validity of the model described here, results from Padki et al. (1989) and Chung and Algren (1958a, b) for cylinders in humid air cross flow under subsaturated conditions are utilized. The cylinder employed in both studies was 25.4 mm in outside diameter. Variation of the frost surface temperature with time for two Reynolds numbers is given in Figure 7-9 for both subsaturated and supersaturated air. Results of the present model are compared with those of Padki et al. (1989) for the subsaturated cases. From the figure, one can easily see that results of both models agree very well. For the same Reynolds number, the frost surface temperature is significantly higher when supersaturated air is used. This can be explained using the results of Figure 7-8. A larger frost thickness necessarily contributes to increasing the frost surface temperature.

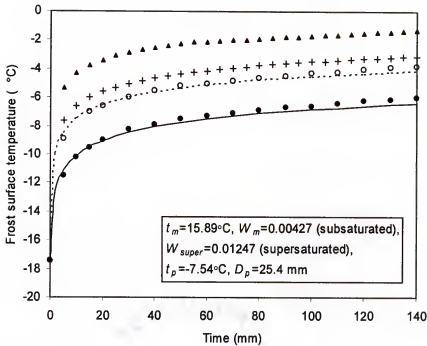


Figure 7-9. Variation of the frost surface temperature with time for different Reynolds numbers: a) $Re=2592$: — present work (subsaturated conditions), ● Padki et al. (1989), and + present work (supersaturated conditions), b) $Re=9965$: ---- present work (subsaturated conditions), ○ Padki et al. (1989), and x (supersaturated conditions)

A similar comparison with the data of Padki et al. (1989) and Chung and Algren (1958a, b) can be performed employing the total frost mass accumulated on the cylinder surface. Figure 7-10 shows how the total mass changes for two Reynolds numbers under both subsaturated and supersaturated air. In this figure, results from Padki et al. (1989) and Chung and Algren (1958a, b) were included for the subsaturated case. From the figure, one can see that the frost mass computed based on the present model is slightly larger than those of Chung and Algren (1958a, b), but smaller than those of Padki et al. (1989) for the subsaturated case. For the same Reynolds number, the amount of frost deposited on the cylinder increases when supersaturated air exists. The gap between the subsaturated and supersaturated cases widens in so far as the frost mass at higher Reynolds numbers is concerned.

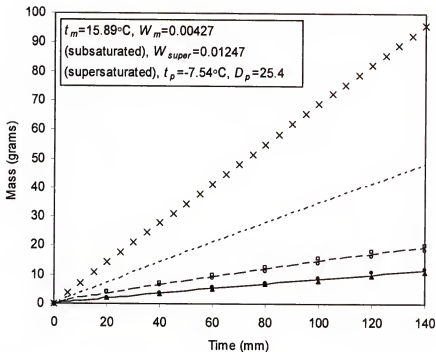


Figure 7-10. Variation of the mass of frost with time for different Reynolds numbers: a) $Re=2592$: — present work (subsaturated conditions), \blacktriangle Chung and Algren (1958), \bullet Padki et al. (1989), and --- present work (supersaturated conditions), b) $Re=9965$: - - - present work (subsaturated conditions), \square Padki et al. (1989), \circ Chung and Algren (1958), and \times (supersaturated conditions)

Conclusions

A semi-empirical, quasi-steady state calculation procedure capable of computing the frost thickness and surface temperature along with the mass of frost deposited on surfaces in the vicinity of supersaturated air was presented. Model results were compared with existing experimental data for the subsaturated cases and were found to agree very well. This model intended to illustrate a relatively simple but accurate methodology to predict frost formation and heat transfer rates on cold surfaces. It should open doors for studying coil frosting problems in the supersaturated zone of the psychrometric chart for more complex geometries.

CHAPTER 8 THEORY OF FROST-FORMATION MECHANISMS

Formation Mechanism in the Subsaturated Zone

While the mechanism of frost formation remains essentially the same in both the subsaturated and supersaturated zones, the formation mechanism under the latter condition is much more complex. The additional complication arises mainly due the presence of supersaturated air with airborne ice crystals that tend to directly deposit on neighboring surfaces, including the freezer walls and the coils. The traditional frost-formation problem is complicated in its own right beyond the traditional moving boundary problem with the simultaneous transfer of heat and mass. This is primarily due to the fact that the formation process cannot solely be described by determining the location of the boundary. Other complicating factors include the fact that frost properties as well as the frost-air interface temperature are both spatially and temporally dependent. The change in the frost-air interface temperature is primarily attributed to the change in the frost thermal resistance. As the interface temperature changes, the partial pressure of water vapor in the vicinity of the frost surface also changes, thus causing a change in the structure of the thermal and diffusion boundary layers. Such changes eventually affect both the heat transfer and frost deposition rates. In cases where the surface temperature of the frost is in the vicinity of the freezing temperature, additional complications may arise due to the occurrence of repeated cycles of melting and re-freezing which tend to change the structure of the frost layer and consequently change the frost density and thermal conductivity with both time and position without appreciably increasing the frost

thickness (Sherif 1991). This is more likely to occur in high-humidity and/or high-temperature environments and is likely to result in an uneven distribution of the frost density, at least in the initial phases of the melting and re-freezing processes. The unevenness in the frost density profile is primarily attributed to the fact that the frost deposited will partially melt and seep through the pores of the porous frost layer, eventually reaching the metal surface where it freezes into ice, and partially stays as frost, thus contributing to an increase in the frost thickness (Sherif et al. 1993). Repeated occurrence of this phenomenon will cause the frost density to be larger near the metal surface relative to that near the upper frost layers and can eventually transform the whole layer into an ice block after very long deposition times. The transformation into a block of ice can usually be attributed to the fact that the frost layer loses most of its porosity as the melt continues to freeze while seeping downward through the porous layer. With the pores mostly closed, the melt will be forced to collect at layers that are successively closer to the frost-air interface and away from the metal surface, thus causing the would-be ice layer to form near the frost-air interface. This trend, if continued, would contribute to creating a more uniform density distribution in the evolving ice layer after a significant amount of time has elapsed since the start of the melting and re-freezing phenomenon.

While the above issues seem to be somewhat intuitive, other issues remain partially unresolved and perhaps somewhat ambiguous. One of these issues has to do with the mechanism that determines how much of the water vapor transforming into frost actually deposits on the upper frost layers and how much of it diffuses inward into the pores of the porous frost layer. White and Cremers (1974) report that approximately half the amount of water vapor transferred into the frost layer diffuses inward, condenses, and

increases the density of the layer, while the other half deposits at the surface and contributes directly to increasing the thickness without appreciably increasing the density. This diffusion would normally take place long before any melting and re-freezing had started. While this theory seems to be a viable one, the exact fraction of water vapor depositing onto versus that diffusing into the frost layer is perhaps a bit more contentious.

One of the issues that may need further investigation has to do with the nature of the structure of the frost layer. In the case of snowflakes, for example, recent studies such as that of Besant (1999) report that there are 80 different crystal configurations each of which start and grow at dust particle nucleation sites in air under slightly different temperature and humidity conditions. Besant (1999) explains that frost growth is similar to that of snow and is thus initiated at nucleation sites as well. When water surface tension forces are relatively small such as the case on aluminum or copper surfaces, Besant (1999) argues that microscopic droplets of water would form first at nucleation points on the surfaces. Those droplets would grow in size, which differ depending on temperature, before the water would freeze. Water freezing would cause frost crystals to form in the vicinity of the location where freezing took place last on the water droplet surface farthest from the solid surface. This issue seems not to have been researched to a significant enough degree and some research should prove useful in providing additional insight into the mechanisms at play as far as frost crystal formation patterns are concerned. These formation patterns are necessarily more mysterious when the conditions prevailing in the freezer correspond to the supersaturated regime.

Other unresolved issues have to do with the mechanism that causes the heat transfer performance degradation in frosted coils. It was believed all along that this degradation is caused by the ever-increasing thermal resistance of the frost layer (Stoecker 1960). While this may be the main reason in the case of plain surfaces, it may not be the ultimate cause when it comes to finned surfaces according to Barrow (1985) who argued that the decrease in the air-side coefficient of heat transfer is a result of geometrical blockage by the frost layer as opposed to an increase in the frost resistance.

While the above observations represent a reasonable description of the current state of knowledge in so far as the frost-formation mechanism in the subsaturated zone is concerned, a significant amount of research is needed in order to provide a comparable amount of knowledge concerning the mechanism of formation in the supersaturated zone. Prior to the conduct of this research program, information pertaining to the frost-formation mechanism in the supersaturated zone was sketchy. Here we attempt to devise a viable theory based on experimental evidence in the laboratory as well as field observations (Smith 1992). This will be the subject of the following section.

Formation Mechanism in the Supersaturated Zone

Frost formation in the supersaturated zone was probably first reported by Smith (1992) who presented some psychrometric calculations for freezer coils to avoid coil operation in the supersaturated zone (Smith 1992) and discussed issues pertaining to latent heat, equipment-related loads and applied psychrometrics in typical industrial freezers (Smith 1992). Supersaturated conditions in freezers usually exist under two most common scenarios. The first scenario pertains to mixing of warm humid air from outside the freezer with cold dry air from within the freezer. This scenario is likely to

take place when the freezer door is opened and will result in the mixing process line between the two conditions crossing the saturation curve on the psychrometric chart into the supersaturated zone. This scenario was investigated by Sherif et al. (1997) and Al-Mutawa (1997). This scenario is very common in walk-in freezers where air mixing is likely near the freezer door.

In a typical interaction between the freezer and the anteroom, an air exchange takes place such that the cold air from the freezer leaves at the bottom and mixes with the anteroom air creating supersaturated conditions outside the freezer (Sherif et al. 1997). This causes suspended liquid water droplets to exist in the air, which result in fog formation at the lower anteroom air layers. Concurrently, the anteroom air at the upper layers rushes inside the freezer to replace the exfiltrated air and mixes with the freezer air in the upper layers of the freezer. This creates supersaturated conditions inside the freezer with airborne ice crystals and an accelerated formation of snow-like frost on the freezer walls and coils. Snow-like frost is different than the traditional frost that forms under subsaturated conditions in that it has less favorable heat transfer characteristics and is denser. The latter characteristic causes snow-like frost to require a larger amount of energy to defrost since the process takes longer to complete as reported by Sherif et al. (1997), Al-Mutawa (1997), Al-Mutawa et al. (1998a, 1998b, 1998c, 1998d) , and Al-Mutawa and Sherif (1998). This makes the formation of snow-like frost even more undesirable because of the double energy penalty associated with its presence and removal.

The second scenario under which supersaturated air exists is associated with air-cooling processes inside the freezer. If the difference between the air entering

temperature (or temperature upstream of the coil) and the coil refrigerant temperature inside the freezer is large enough and if a significant latent load exists in the freezer, the cooling process line is likely to cross into the supersaturated zone on the psychrometric chart. The temperature difference mentioned above is referred to as the coil TD in industrial refrigeration circles and is frequently used as a measure of how well the coil is operating. As mentioned above, the crossing of the cooling process line into the supersaturated zone is frequently accompanied by the presence of a significant latent load in the freezer.

As reported earlier, the frost-formation process in the supersaturated zone is probably driven by two distinct mechanisms. The first mechanism is the traditional diffusion mechanism as is the case in the subsaturated zone. In this case, the water vapor concentration (or the humidity ratio) driving force between the free stream and the air in the vicinity of the cold surface acts as the main driving mechanism for the transfer of water vapor from the free stream to the cold surface in the form of solid frost (bypassing the liquid phase). The water vapor difference is predominantly the result of the temperature difference that exists between the free stream and the cold surface. Since the cold surface is often cooler than the free stream, the mass transfer driving force is often towards the cold surface. However, the mass transfer driving force is not solely a function of the temperature difference. Frost will form if the free stream air in the freezer has a larger humidity ratio than the air present in the vicinity of the cold surface provided that the temperature of the latter is less than the dew-point temperature of water vapor in air and also below the freezing point. In supersaturated conditions, the above mechanisms are still applicable but with a greater intensity since the moisture content in

the free stream is significantly larger than in cases involving subsaturated air. Since the excess moisture (beyond saturation) in supersaturated air is incapable of existing in the vapor phase, it would have to exist in one of two possible formations; either as suspended liquid droplets if the air temperature is above freezing or as airborne ice crystals if the air temperature is below freezing. The presence of airborne ice crystals contributes to an additional amount of frost accumulation by merely depositing on any cold surface they encounter, including the coil surface and the freezer walls and ceiling. Thus, while one of the frost-formation mechanisms in the supersaturated zone is identical to that in the subsaturated zone, a second mechanism driven by direct precipitation of airborne ice crystals on the cold surface kicks in. This mechanism is driven by convection currents inside the freezer. Airborne ice crystals originate as frozen suspended liquid water droplets and, as a consequence, are fundamentally different in their crystalline structure than the more traditional frost crystals. Frozen liquid water droplets have a larger specific heat and are denser and thus require a larger amount of time to defrost relative to the more traditional frost crystals. Also, because those airborne ice crystals are bigger in size than the traditional frost crystals, they tend to clog the passages of the freezer coil much faster and with a greater intensity.

CHAPTER 9

SOFTWARE FOR THE DESIGN AND OPERATIONAL PHASES OF REFRIGERATED FACILITIES

Objective

The objective of this chapter is to develop two pieces of software that can be utilized in both the design and operational phases of refrigerated facilities.

Software for Predicting the Onset of Frost Formation

This software will be based on the analytical model described in Chapter 7. It will be used to determine the frost formation and heat transfer on a cylinder surface under forced convection. Once more it is important to point out that although the results obtained using the software are for a cylinder, they are a good approximation for tubes in a freezer coil. This software performs analysis under both subsaturated and supersaturated freezer conditions.

User manual. In this section the functionality of the simulation software will be described. This will be done by presenting the different possible screens that will appear during the operation of the software. When the software is started it will show the Main Menu screen (Figure 9-1). This is the screen that will allow the users to operate the software. Here the user can perform several tasks such as: input simulation data, see simulation results (numerical and graphical), and save and print data and results of the simulation.



Figure 9-1. Main Menu of the software

- ① If the “Data” command is chosen, the software will show a screen where the user can input all the data required for the simulation (Figure 9-2). Here, the user can select the type of simulation to be performed: a) considering average properties around the cylinder, and b) at any specific angle along the circumference of the cylinder. After the user inputs the data of the simulation, the results can be obtained in two ways: numerically or graphically by selecting the command “Results” or “Graphical Results,” respectively.
- ② If the command “Results” is selected a new screen showing the results will appear (Figure 9-3). The results that are displayed on this screen include: frost surface temperature, mass of frost, frost thickness, Reynolds number, and the convective heat and mass transfer coefficients.
- ③ If the command “Graphical Results” is selected, a new screen showing a sub-menu (Figure 9-4) will appear. In this screen several simulation scenarios can be selected. This

includes frost thickness vs. time, frost surface temperature vs. time, mass of frost deposited vs. time, and the convective heat and mass transfer coefficients vs. time.

Figure 9-5 shows some of these scenarios on the screen.

The screenshot shows a 'Data' dialog box with the following sections and controls:

- Type of Simulation:**
 - ☒ Considering Average Conditions Around the Cylinder's Surface
 - ☐ At Any Specific Point on the Cylinder Surface
- Data for the Simulation:**
 - Entering Air Temperature (C): 15.89
 - Relative Humidity (%): 38.28
 - Coil Face Velocity (m/s): 1.522
 - Tube Diameter (m): 0.0254
 - Tube Length (m): 0.6096
 - Coil Surface Temperature (C): -17.44
 - Total Time (s): 1000
 - Time increment (s): 1
 - Angle on the Cylinder Surface (degrees): 60
- Buttons:**
 - OK
 - Cancel
 - Clear the Data
 - Help

Figure 9-2. Screen to input the simulation data

- ④ If the command “Air Properties” is selected, a new screen (Figure 9-6) will appear. This screen displays air properties such as thermal conductivity, viscosity, thermal diffusivity, Prandtl number, and the specific heat for any temperature that the user inputs.
- ⑤ If the command “Data and Results File” is selected, a file with all the simulation information such as data and results will be saved under the name “Results.”
- ⑥ This command can be used to print the data and results of the simulation. This is the

print version of the file created with the command “Data and Results File.”

- ⑦ This command is used to exit the software.
- ⑧ If this command is selected a new screen showing the information about the software as well as the information about the authors will be displayed.

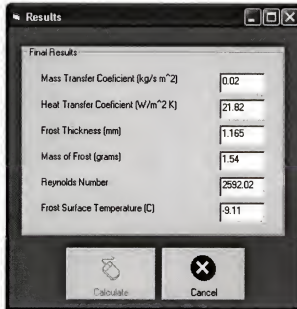


Figure 9-3. Screen showing the numerical results

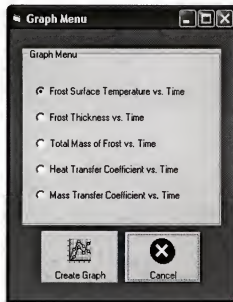
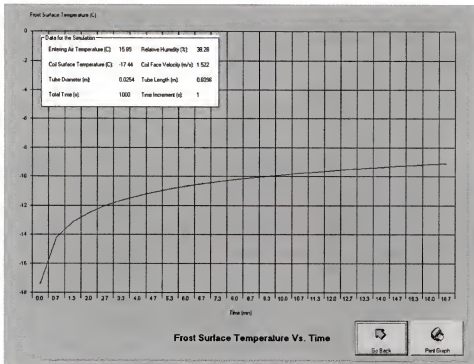
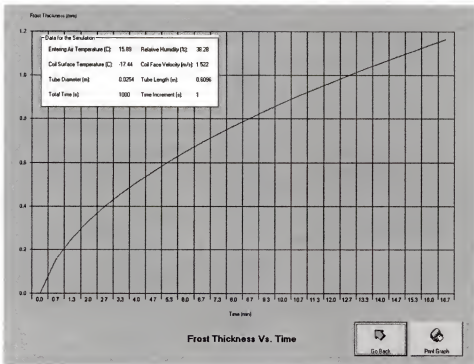


Figure 9-4. Graph menu to see the graphical results



A



B

Figure 9-5. Screen showing graphical results: A) frost surface temperature vs. time B) frost thickness vs. time

In Figure 9-5 (a) and (b) if the command “Go Back” is selected the Graph Menu screen will be displayed again. Also, the graphs show in Figure 9-5 can be printed if the “Print” command is selected.

Air Temperature	
<input checked="" type="radio"/> K	300
<input type="radio"/> C	26.85

Air Properties	
Thermal Conductivity (W/m. K)	0.0263
Kinematic Viscosity (m ² /s)	0.00001589
Thermal Diffusivity (m ² /s)	0.0000225
Prandtl Number	0.707
Specific Heat (kJ/kg. K)	1.007

Figure 9-6. Screen showing air properties

Software for Simulating Freezer Operation

The second software will be used to guide freezer operators in avoiding supersaturated operating conditions. The idea is for the operators to input the system data and let the software provide them with information as to where the system's operating point is on the psychrometric chart.

User manual. In this section the functionality of the simulation software will be described. This will be done by presenting the different screens that appear during the execution of the software. When the software is started it will show the Main Menu screen (Figure 9-7).

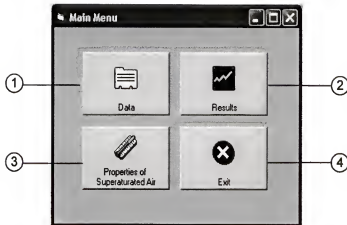


Figure 9-7. Main Menu of the software

- ① If the command “Data” is chosen, the software will display a screen where the user can input the required data for the simulation (Figure 9-8).
- ② If the command “Results” is selected, the software will display a screen with the results (Figure 9-9). As can be seen from the figure, the user will obtain results numerically and graphically. In this screen the solid straight-line represents the cooling and dehumidification process, while the curved line represents the saturation curve, the dotted straight-line being a reference line. The interception between the solid and dotted straight-lines represents the air leaving conditions. From Figure 9-9(a) it can be observed that the system is operating under subsaturated conditions. This is shown in the box named “Note” where a message is presented. In Figure 9-9(b) we can see how the software displays a warning message in the box named “Note,” indicating that the system is operating under supersaturated conditions. The critical conditions where the cooling and dehumidification straight-line process crosses the saturation curve are shown in the box named “Critical Conditions.”

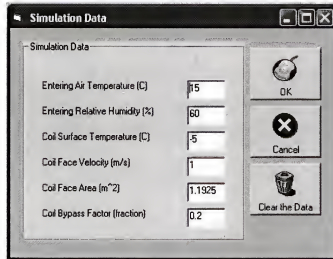
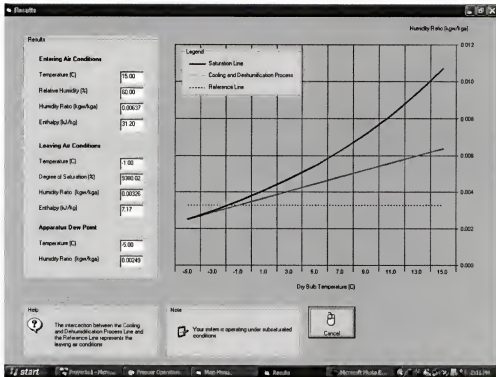
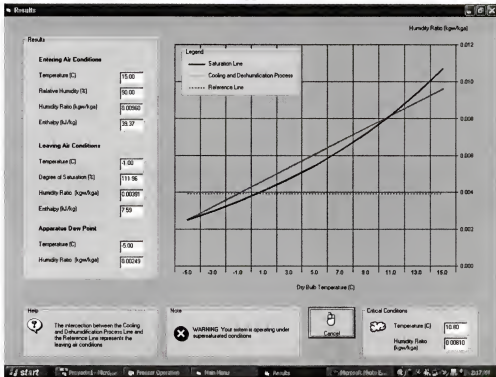


Figure 9-8. Simulation data screen

- ③ If the command "Properties of Supersaturated Air" is selected a screen where the properties of supersaturated air (specific enthalpy, specific volume, degree of supersaturation, and supersaturated humidity ratio) can be computed is displayed.
- ④ This command is used to exit the software.



A



B

Figure 9-9. Some results screen of the software: A) showing operation under subsaturated conditions, and B) showing operation under supersaturated conditions

CHAPTER 10 CONCLUSIONS

Here is a summary of some the conclusions of this investigation:

- The aforementioned discussions and observations underline the importance of applying psychrometric theory in the design and operation of freezers. Without proper understanding of the theory, one can easily see how freezer operation can be dominated by the presence of unwanted ice crystal formation, snow-like frost accumulation, and severe degradation in the coil heat transfer performance.
- In this investigation the existence of a demarcation line between the type of frost that forms under subsaturated conditions and that frost that forms under supersaturated conditions was established. With the use of a mathematical model, the location where the transition from one condition to the other occurs was also established.
- Operating freezers under supersaturated conditions is most costly because it increases the frequency and duration of defrosting and the amount of defrosting heat input required.
- The use of heat pipes is advantageous for freezer operation as the burden of cooling and dehumidifying the air is redistributed such that the heat-pipe coil performs the sensible cooling, while the dehumidifying process is carried out by the freezer coil.

- The use of partially-dampered coils was shown to increase the defrost efficiency by 18%, while the use of fully-dampered coils increases the efficiency by 43%.
- The use of dampered coils prevents evaporated water and sublimated frost from going back into the freezer space, thus helping reduce the defrosting frequency of other coils that may be operating in the refrigeration mode in the vicinity of the coil being defrosted.
- Increasing the coil-face velocity during refrigeration increases the defrost efficiency. This may be partially explained by the more cohesive nature of the frost forming at higher face velocities and the subsequent improvements in melt collection and the corresponding reduction in evaporated water and/or sublimated frost into the freezer space.
- A semi-empirical, quasi-steady state calculation procedure capable of computing the frost thickness and surface temperature along with the mass of frost deposited on surfaces in the vicinity of supersaturated air was presented. Model results were compared with existing experimental data for the subsaturated cases and were found to agree very well. This model should open doors for studying coil frosting problems in the supersaturated zone of the psychrometric chart for more complex geometries.
- Psychrometric data for supersaturated air have been developed and presented in the form of psychrometric charts for degrees of saturation from 100% to 200%. This method extends the current psychrometric data, which are presently only available in the subsaturated zone of the psychrometric chart. The properties

developed in this investigation should enable the refrigeration engineer and system designer to better predict the performance of the system as well as design a more optimal system.

- Two pieces of software whose primary purpose is to guide refrigeration system design engineers and freezer operators in their mission were developed.

APPENDIX UNCERTAINTY ANALYSIS

The method used for the uncertainty calculations is the one described by Kline and McClintock (1953). Suppose that a result “R” is a function of a number of independent variables $X_1, X_2, X_3, \dots, X_n$.

$$R = R(X_1, X_2, X_3, \dots, X_n) \quad (\text{A-1})$$

And each of those variables has an uncertainty $(\xi_{X_1}, \xi_{X_2}, \dots, \xi_{X_n})$. The total uncertainty in the result, “ ξ_R ”, is found through the following equation:

$$\xi_R = \left[\left(\frac{\partial R}{\partial X_1} \xi_{X_1} \right)^2 + \left(\frac{\partial R}{\partial X_2} \xi_{X_2} \right)^2 + \dots + \left(\frac{\partial R}{\partial X_n} \xi_{X_n} \right)^2 \right]^{1/2} \quad (\text{A-2})$$

In this investigation properties of R-22 were determined using software developed by Gallagher et al. (1993). The properties of the water were determined using software developed by Intellipro (1998). The uncertainties of these properties were calculated using the same method describe above. For example, the enthalpy is a function of temperature and pressure; $i = i(t, P)$, therefore the uncertainties of the enthalpy were determined using Equation A-2.

$$\xi_i = \left[\left(\frac{\partial i}{\partial t} \xi_t \right)^2 + \left(\frac{\partial i}{\partial P} \xi_P \right)^2 \right]^{1/2} \quad (\text{A-3})$$

In this equation the terms $\partial i / \partial t$ and $\partial i / \partial P$ were determined numerically using the software, while the uncertainty of the temperature (ξ_t) and pressure (ξ_P) were taken from Table A-1. The uncertainties of these properties are shown in Table A-2.

Table A-1. Uncertainty of experimental measurements

Quantity	Instrumentation Method	Uncertainty
Temperature	Copper-constantan (Type T) thermocouples	$\xi_T = \pm 0.2^\circ\text{C}$
Frost surface temperature	FLIR Systems thermacam PM 695 infrared camera	$\xi_{t,i} = \pm 2^\circ\text{C}$
Relative humidity	Mamac HU-224 humidity transducer.	$\xi_{RH} = \pm 2\%$
Pressure	Mamac PR-274 and PR-264 pressure transducers	$\xi_P = \pm 1\%$ of the measured pressure
Coil-face velocity	System controls and instrumentation M4000E digital HVAC analyzer	$\xi_u = \pm 2\%$ of the measured velocity
Mass of the melt	Arlyne scale Co. 610L precision digital scale	$\xi_{m_{melt}} = \pm 0.005 \text{ kg}$

Table A-2. Uncertainty of the refrigerant and water properties

Quantity	Uncertainty
Enthalpy of refrigerant, i_R	$\xi_{i_R} = \pm 2\%$
Density of refrigerant, ρ_R	$\xi_{\rho_R} = \pm 2\%$
Dynamic viscosity of refrigerant, μ_R	$\xi_{\mu_R} = \pm 2\%$
Enthalpy of liquid water, i_{liquid}	$\xi_{i_{liquid}} = \pm 2\%$
Enthalpy of ice, i_{ice}	$\xi_{i_{ice}} = \pm 2\%$

Table A-3. Uncertainty of the results

Quantity	Uncertainty
Refrigerant volumetric flow rate, \dot{V}_R	$\xi_{\dot{V}_R} = \pm 2\%$
Refrigerant mean velocity, $u_{m,R}$	$\xi_{u_{m,R}} = \pm 2\%$
Reynolds number, Re	$\xi_{Re} = \pm 3.5\%$
Discharge coefficient, C_d	$\xi_{C_d} = \pm 1\%$
Flow coefficient of the orifice meter, $K_{orifice}$	$\xi_{K_{orifice}} = \pm 1\%$
Refrigerant vapor mass flow rate, $\dot{m}_{R,vap}$	$\xi_{\dot{m}_{R,vap}} = \pm 2.5\%$
Defrosting heat input rate, $\dot{Q}_{def,in}$	$\xi_{\dot{Q}_{def,in}} = \pm 4\%$
Defrosting heat input, $Q_{def,in}$	$\xi_{Q_{def,in}} = \pm 4\%$
Rate of heat remove with the FCU-T melt, \dot{Q}_{melt}	$\xi_{\dot{Q}_{melt}} = \pm 4\%$
Heat remove with the FCU-T melt, Q_{melt}	$\xi_{Q_{melt}} = \pm 4\%$
Defrost efficiency, η_{def}	$\xi_{\eta_{def}} = \pm 4\%$
Average coil performance load rate, $ACPLR$	$\xi_{ACPLR} = \pm 4\%$
Fan defrost contribution, FDC	$\xi_{FDC} = \pm 4\%$

Table A-3. Continued

Quantity	Uncertainty
Air volumetric flow rate, \dot{V}_a	$\xi_{\dot{V}_a} = \pm 2\%$
Air velocity, u_a	$\xi_{u_a} = \pm 2\%$
Air density, ρ_a	$\xi_{\rho_a} = \pm 2\%$
Saturation pressure, P_s	$\xi_{P_s} = \pm 2\%$
Partial pressure of water vapor, P_w	$\xi_{P_w} = \pm 3\%$
Air humidity ratio, W_a	$\xi_{W_a} = \pm 3\%$
Air enthalpy, i_a	$\xi_{i_a} = \pm 3\%$

Table A-4. Function and partial derivative for the calculated quantities

	Function	Partial derivative
\dot{V}_R (m ³ /s)	$\dot{V}_R = 4.187657 \times 10^{-5} + (6.37861 \times 10^{-4} \Delta P)$ $- (2.65091 \times 10^{-4} \Delta P^2)$ $+ (7.27778 \times 10^{-5} \Delta P^3)$ $- (1.0033 \times 10^{-5} \Delta P^4)$ $+ (5.3196 \times 10^{-7} \Delta P^5)$	$\frac{\partial \dot{V}_R}{\partial \Delta P} = [6.37861 \times 10^{-4} - (5.30182 \times 10^{-4} \Delta P)$ $+ (21.8333 \times 10^{-5} \Delta P^2)$ $+ (4.0132 \times 10^{-5} \Delta P^3)$ $+ (26.598 \times 10^{-7} \Delta P^4)]$
$u_{m,R}$ (m/s)	$u_{m,R} = \frac{\dot{V}_R}{A_{orifice}}; A_{orifice} = 0.0001393 \text{ m}^2$	$\frac{\partial u_{m,R}}{\partial \dot{V}_R} = \frac{1}{A_{orifice}}$
Re	$Re = \frac{\rho_R u_{m,R} D_1}{\mu_R}, D_1 = 13.386 \text{ mm}$	$\frac{\partial Re}{\partial \rho_R} = \frac{u_{m,R} D_1}{\mu_R}; \frac{\partial Re}{\partial u_{m,R}} = \frac{D_1 \rho_R}{\mu_R}; \frac{\partial Re}{\partial \mu_R} = -\frac{D_1 \rho_R u_{m,R}}{\mu_R^2}$
C_d	$C_d = [0.5959 + 0.0312\psi^{2.1} - 0.184\psi^8$ $+ 0.039 \frac{\psi^4}{1-\psi^4} - 0.0158\psi^3 + \frac{91.71\psi^{2.5}}{Re^{0.75}}]$ $\psi = 0.5$	$\frac{\partial C_d}{\partial Re} = -\frac{68.7825\psi^{2.5}}{Re^{1.75}}$
$K_{orifice}$	$K_{orifice} = \frac{C_d}{\sqrt{1-\psi^4}}; \psi = 0.5$	$\frac{\partial K_{orifice}}{\partial C_d} = \frac{1}{\sqrt{1-\psi^4}}$
\dot{V}_a (m ³ /s)	$\dot{V}_a = u_a A$	$\frac{\partial \dot{V}_a}{\partial u_a} = A; \frac{\partial \dot{V}_a}{\partial A} = u_a$
\dot{m}_a (kg/s)	$\dot{m}_a = \rho_a \dot{V}_a$	$\frac{\partial \dot{m}_a}{\partial \rho_a} = \dot{V}_a; \frac{\partial \dot{m}_a}{\partial \dot{V}_a} = \rho_a$

Table A-4. Continued

	Function	Partial derivative
$\dot{m}_{R,vap}$ (kg/s)	$\dot{m}_{R,vap} = K_{orifice} A_{orifice} \psi^2 \sqrt{2g\rho_R \rho_{water} \Delta P}$ $g = 9.81 \text{ m/s}^2$ $\rho_{water} = 1000 \text{ kg/m}^3$	$\frac{\partial \dot{m}_{R,vap}}{\partial \rho_R} = 0.7071 \frac{K_{orifice} A_{orifice} \psi^2 g \rho_{water} \Delta P}{\sqrt{g \rho_R \rho_{water} \Delta P}}$ $\frac{\partial \dot{m}_{R,vap}}{\partial \Delta P} = 0.7071 \frac{K_{orifice} A_{orifice} \psi^2 g \rho_{water} \rho_R}{\sqrt{g \rho_R \rho_{water} \Delta P}}$ $\frac{\partial \dot{m}_{R,vap}}{\partial K_{orifice}} = A_{orifice} \psi^2 \sqrt{2g \rho_R \rho_{water} \Delta P}$
$\dot{Q}_{def,in}$ (kW)	$\dot{Q}_{def,in} = \dot{m}_{R,vap} (i_{in} - i_{out})$	$\frac{\partial \dot{Q}_{def,in}}{\partial \dot{m}_{R,vap}} = (i_{in} - i_{out});$ $\frac{\partial \dot{Q}_{def,in}}{\partial i_{in}} = -\frac{\partial \dot{Q}_{def,in}}{\partial i_{out}} = \dot{m}_{R,vap}$
$Q_{def,in}$ (kJ)	$Q_{def,in} = \dot{m}_{R,vap} (i_{in} - i_{out}) \tau_{def}$	$\frac{\partial Q_{def,in}}{\partial \dot{m}_{R,vap}} = (i_{in} - i_{out}) \tau_{def};$ $\frac{\partial Q_{def,in}}{\partial \tau_{def}} = \dot{m}_{R,vap} (i_{in} - i_{out})$ $\frac{\partial Q_{def,in}}{\partial i_{in}} = -\frac{\partial Q_{def,in}}{\partial i_{out}} = \dot{m}_{R,vap} \tau_{def}$
\dot{Q}_{melt} (kW)	$\dot{Q}_{melt} = \frac{m_{melt} (i_{liq} - i_{ice})}{\tau_{def}}$	$\frac{\partial \dot{Q}_{melt}}{\partial m_{melt}} = \frac{(i_{liq} - i_{ice})}{\tau_{def}}; \frac{\partial \dot{Q}_{melt}}{\partial \tau_{def}} = -\frac{m_{melt} (i_{liq} - i_{ice})}{\tau_{def}^2}$ $\frac{\partial \dot{Q}_{melt}}{\partial i_{liq}} = -\frac{\partial \dot{Q}_{melt}}{\partial i_{ice}} = \frac{m_{melt}}{\tau_{def}}$
Q_{melt} (kJ)	$Q_{melt} = m_{melt} (i_{liq} - i_{ice})$	$\frac{\partial Q_{melt}}{\partial m_{melt}} = (i_{liq} - i_{ice}); \frac{\partial Q_{melt}}{\partial i_{liq}} = \frac{\partial Q_{melt}}{\partial i_{ice}} = m_{melt}$
η_{def}	$\eta_{def} = \frac{\dot{Q}_{melt}}{\dot{Q}_{def,in}}$	$\frac{\partial \eta_{def}}{\partial \dot{Q}_{melt}} = \frac{1}{\dot{Q}_{def,in}}; \frac{\partial \eta_{def}}{\partial \dot{Q}_{def,in}} = -\frac{\dot{Q}_{melt}}{\dot{Q}_{def,in}^2}$
$ACPLR$ (kW)	$ACPLR = \frac{(Q_{total} + Q_{def,in} - Q_{melt})}{\tau_{total}}$	$\frac{\partial ACPLR}{\partial Q_{def,in}} = -\frac{\partial ACPLR}{\partial Q_{melt}} = \frac{1}{\tau_{total}}$
FDC (%)	$FDC = \frac{(Q_{fan} + Q_{def,in} - Q_{melt})}{Q_{net}} (100)$	$\frac{\partial FDC}{\partial Q_{def,in}} = \frac{\partial FDC}{\partial Q_{melt}} = \frac{100}{Q_{net}}$

Table A-4. Continued

	Function	Partial derivative
ρ_a (m ³ /kg)	$\rho_a = \frac{P}{R_a T_a (1 + 1.6078 W_a)}$	$\frac{\partial \rho_a}{\partial T_a} = -\frac{1.6078 P}{R_a T_a^2 (1 + 1.6078 W_a)}$ $\frac{\partial \rho_a}{\partial W_a} = -\frac{1.6078 P}{R_a T_a (1 + 1.6078 W_a)^2}$
P_s (kPa)	$P_s = \exp \left[\sum_0^5 a_i (T)^{i-1} + a_6 \log_e (T) \right]$ for $[263.15 \text{ K} \leq T \leq 273.15 \text{ K}]$ $P_s = \exp \left[\sum_0^4 b_i (T)^{i-1} + b_5 \log_e (T) \right]$ for $[273.15 \text{ K} \leq T \leq 473.15 \text{ K}]$	$\frac{\partial P_s}{\partial T} = P_s \left(-\frac{a_0}{T^2} + a_2 = 2a_3 T + 3a_4 T^2 + 4a_5 T^3 + \frac{a_6}{T} \right)$ $\frac{\partial P_s}{\partial T} = P_s \left(-\frac{b_0}{T^2} + b_2 + 2b_3 T + 3b_4 T^2 + \frac{b_5}{T} \right)$
P_w (kPa)	$P_w = \frac{P_s RH}{100}$	$\frac{\partial P_w}{\partial P_s} = \frac{RH}{100}; \quad \frac{\partial P_w}{\partial RH} = \frac{P_s}{100}$
W_a (kgw/kg _a)	$W_a = 0.622 \frac{P_w}{P - P_w}$	$\frac{\partial W_a}{\partial P_w} = 0.622 \left[\frac{1}{P - P_w} + \frac{P_w}{(P - P_w)^2} \right]$
i_a (kJ/kg)	$i_a = 1.006 t_a + (2501 + 1.805 t_a) W_a$	$\frac{\partial i_a}{\partial t_a} = 1.006 + 1.805 W_a$ $\frac{\partial i_a}{\partial W_a} = 2501 + 1.805 t_a$

LIST OF REFERENCES

- Al-Mutawa, N.K., 1997, "Experimental Investigations of Frosting and Defrosting of Evaporator Coils at Freezer Temperatures," Ph.D. Dissertation, University of Florida, Gainesville, Florida.
- Al-Mutawa, N.K. and Sherif, S.A., 1998, "Determination of Coil Defrosting Loads: Part V - Analysis of Loads (RP-622)," *ASHRAE Transactions*, Vol. 104, Part 1A, Paper No. 4124, January, pp. 344-355.
- Al-Mutawa, N.K., Sherif, S.A., and Mathur, G.D., 1998a, "Determination of Coil Defrosting Loads: Part III - Testing Procedures and Data Reduction (RP-622)," *ASHRAE Transactions*, Vol. 104, Part 1A, Paper No. 4122, January, pp. 303-312.
- Al-Mutawa, N.K., Sherif, S.A., Mathur, G.D., Steadham, J.M., West, J., Harker, R.A., and Tiedeman, J.S., 1998b, "Determination of Coil Defrosting Loads: Part II - Instrumentation and Data Acquisition Systems (RP-622)," *ASHRAE Transactions*, Vol. 104, Part 1A, Paper No. 4121, January, pp. 289-302.
- Al-Mutawa, N.K., Sherif, S.A., Mathur, G.D., West, J., Tiedeman, J.S., and Urlaub, J., 1998c, "Determination of Coil Defrosting Loads: Part I - Experimental Facility Description (RP-622)," *ASHRAE Transactions*, Vol. 104, Part 1A, Paper No. 4120, January, pp. 268-288.
- Al-Mutawa, N.K., Sherif, S.A., and Steadham, J.M., 1998d, "Determination of Coil Defrosting Loads: Part IV - Refrigeration/Defrost Cycle Dynamics (RP-622)," *ASHRAE Transactions*, Vol. 104, Part 1A, Paper No. 4123, January, pp. 313-343.
- Andrichak, S.M., 1962, "Formation of a Layer of Frost on a Cylinder in Crossflow of Air," M.S. Thesis, The Ohio State University, Columbus, Ohio.
- ASHRAE, 1998, *1998 ASHRAE Handbook – Refrigeration*, The American Society of Heating, Refrigerating and Air-Conditioning Engineers, Inc., Atlanta, Georgia.
- ASHRAE, 2001, *2001 ASHRAE Handbook – Fundamentals*, The American Society of Heating, Refrigerating and Air-Conditioning Engineers, Inc., Atlanta, Georgia.
- ASME Fluid Meters Research Committee, 1991, The ISO-ASME Orifice Coefficient Equation, *Mechanical Engineering*, Vol. 103, July, pp. 44-45.
- Barrow, H., 1985, "A Note on the Frosting of Heat Pump Evaporator Surfaces," *Journal of Heat Recovery Systems*, Vol. 5, No. 3, pp. 195-201.

- Besant, R.W., 1999, "Characterization of Frost Growth and Heat Transfer at Low Temperatures," Final Report, ASHRAE RP-824, The American Society of Heating, Refrigerating and Air-Conditioning Engineers, Atlanta, Georgia, January.
- Biguria, G.O. and Wenzel, L.A., 1970, "Measurements and Correlation of Water Frost Thermal Conductivity and Density," *Industrial and Engineering Chemistry Fundamentals*, Vol. 9, No. 1, pp. 129-138.
- Brian, P.L.T., Reid, R.C., and Brazinsky, I., 1969, "Cryogenic Frost Properties," *Cryogenic Technology*, Vol. 5, No. 5, pp. 205-212.
- Chen, H., Thomas, L., and Besant, R.W., 2000a, "Modeling Frost Characteristics on Heat Exchanger Fins: Part I. Numerical Model," *ASHRAE Transactions*, Vol. 106, Part 2, pp. 357-367.
- Chen, H., Thomas, L., and Besant, R.W., 2000b, "Modeling Frost Characteristics on Heat Exchanger Fins: Part II. Model Validation and Limitations," *ASHRAE Transactions*, Vol. 106, Part 2, pp. 368-376.
- Chung, P.M. and Algren, A.B., 1958a, "Frost Formation and Heat Transfer on a Cylinder Surface in Humid Air Cross Flow: Part I," *Heating, Piping and Air Conditioning*, September, pp. 171-178.
- Chung, P.M. and Algren, A.B., 1958b, "Frost Formation and Heat Transfer on a Cylinder Surface in Humid Air Cross Flow: Part II," *Heating, Piping and Air Conditioning*, October, pp. 115-122.
- Churchill, S.W. and Bernstein, M., 1977, "Correlating Equation for Forced Convection from Gases and Liquids to a Circular Cylinder in Crossflow," *Journal of Heat Transfer*, Vol. 99, pp.300-306
- Coley, M.B., 1983, "The Cost of Frost," *ASHRAE Journal*, Vol. 82, No. 9, pp. 29-31.
- Dittus, F.W. and Boelter, L.M.K, 1930, *Heat Transfer in Automobile Radiations of Tubular Type*, Publications on Engineering, University of California, Berkeley, Vol. 2, p. 443-461.
- Fox, R.W. and McDonald, A.T., 1992, *Introduction to Fluid Mechanics*, Fourth Edition, John Wiley and Sons, Inc., New York, NY.
- Gallagher, J., Mc Linden, M., Morrison, G., and Huber, M., 1993, *Thermodynamic Properties of Refrigerants and Refrigerant Mixture, Version 4.0*, Thermophysics Division, Chemical Science and Technology Laboratory of the National Institute of Standard and Technology, Gaithersburg, MD.
- Giedt, W. H., 1949, "Investigation of Variation of Point Unit Heat Transfer Coefficient Around a Cylinder Normal to an Air Stream," *ASME Transactions*, Vol. 71, pp. 375-381.

- Grimison, E.D., 1937, "Correlation and Utilization of New Data on Flow Resistance and Heat Transfer for Cross Flow of Gases Over Tube Bank," *Transactions of the ASME*, Vol. 59, pp. 583-589.
- Hayashi, Y., Aoki, A., Adachi, S., and Hori, K., 1977a, "Study of Frost Properties Correlating with Frost Formation Types," *ASME Journal of Heat Transfer*, Vol. 99, No. 2, pp. 239-245.
- Hayashi, Y., Aoki, K., and Yuhara, H., 1977b, "Study of Frost Formation Based on a Theoretical Model of the Frost layer," *Heat Transfer-Japanese Research*, Vol. 6, No. 3, July-September, pp. 79-94.
- Himmelblau, D. M., 1960, "Solubility of Inert Gases in Water," *Journal of Chemical and Engineering Data*, Vol. 5, No. 1, pp. 10-15.
- Holman, J.P., 1997, *Heat Transfer*, Eighth Edition, McGraw-Hill, Inc., New York, NY.
- Hyland, R. W. and Wexler, A., 1983a, "Formulation of the Thermodynamic Properties of Dry Air from 173.15K to 473.15K, and of Saturated Moist Air from 173.15K to 372.15K, at Pressures to 5MPa," *ASHRAE Transactions*, Vol. 89, Part 2(A), pp. 520-535.
- Hyland, R. W. and Wexler, A., 1983b, "Formulation for the Thermodynamic Properties of the Saturated Phases of H₂O from 173.15K to 473.15K," *ASHRAE Transactions*, Vol. 89, Part 2(A), pp. 500-519.
- Incropera, F.P. and DeWitt, D.P., 1996, *Fundamentals of Heat and Mass Transfer*. Fourth Edition, John Wiley & Sons, Inc., New York.
- Intellipro, Inc., 1998, *CATT2: Computer-Aided Thermodynamic-Tables 2*, Version 1.0a, [Computer program], Wiley College Software, Published by John Wiley & Sons, Inc.
- Kerschbauner, H.G., 1971, "Analysis of the Influence of Frost Formation on Evaporators and of the Defrost Cycles on Performance and Power Consumption of Refrigeration Systems," *XIII International Congress of Refrigeration*, Washington, D.C., Paper #3.11, pp. 719-730.
- Kline, S. J., and McClintock, F. A., 1953, "Describing Uncertainties in Single-Sample Experiments," *Mechanical Engineering*, Vol. 75, pp. 3-8.
- Kondepudi, S.N. and O'Neal, D.L., 1988, "Performance of Triangular Spine Fins Under Frosting Conditions," *Heat Recovery systems & CHP*, Vol. 8, No. 1, pp. 1-7.
- Kondepudi, S.N. and O'Neal, D.L., 1989, "Effect of Frost Growth on the Performance of Louvered Finned Tube Heat Exchangers," *International Journal of Refrigeration*, Vol. 12, No. 3, pp. 151-158.

- Kondepudi, S.N. and O'Neal, D.L., 1991, "Frosting Performance of Tube Heat Exchangers with Wavy and Corrugated Fins," *Experimental Thermal and Fluid Science*, Vol. 4, No. 5, September, pp. 613-618.
- Kuehn, T.H., Ramsey, J.W., and Threlkeld, J.L., 1998, *Thermal Environmental Engineering*, Third Edition, Prentice Hall, Upper Saddle River, New Jersey.
- Marinyuk, B.T., 1980, "Heat and Mass Transfer Under Frosting Conditions," *International Journal of Refrigeration*, Vol. 3, No. 6, pp. 366-368.
- Martinelli, R.C., Guibert, A.C., Morin, E.H., and Boelter, L.M.K., 1943, "An Investigation of Aircraft Heaters VIII – a Simplified Method for Calculating the Unit-Surface Conductance over Wings," NACA ARR, March.
- Miller, R.W., 1981, *Flow Measurement Engineering Handbook*, Second Edition, McGraw-Hill Publishing Company, New York.
- Nelson, H.F., Sauer, H.J., and Huang, X., 2001, "High Temperature Properties of Moist Air," *ASHRAE Transactions*, Vol. 107, Part 2, June.
- Niederer, D.H., 1976, "Frosting and Defrosting Effects on Coil Heat Transfer," *ASHRAE Transactions*, Vol. 82, Part 1, January, pp. 467-473.
- Olivieri, J., Singh, T., and Lovodocky, S., 1996, *Psychrometrics: Theory and Practice*, The American Society of Heating, Refrigerating and Air-Conditioning Engineers, Inc., Atlanta, Georgia.
- Padki, M.M., Sherif, S.A., and Nelson, R.M., 1989, "A Simple Method for Modeling Frost Formation in Different Geometries," *ASHRAE Transactions*, Vol. 95, part 2, June, pp. 1127-1137.
- Parish, H.C., 1970, "A Numerical Analysis of Frost Formation Under Forced Convection," M.S. Thesis, The Ohio State University, Columbus, Ohio.
- Parish, H.C. and Sepsy, C.F., 1972, "A Numerical Analysis of Frost Formation Under Forced Convection," *ASHRAE Transactions*, Vol. 78, part 1, Paper No. 2231, January, pp. 236-251.
- Raju, S.P. and Sherif, S.A., 1993, "Frost Formation and Heat Transfer on Circular Cylinders in Cross Flow," *International Journal of Refrigeration*, Vol. 16, No. 6, November, pp. 390-402.
- Sauer, H.J., Nelson, H.F., and Huang, X., 2001, "The Search for High Temperature Experimental Psychrometric Data," *ASHRAE Transactions*, Vol. 107, Part 2, pp. 768-779.
- Schmidt, E., and Wenner, K., 1941, "Wärmeabgabe über den Umfang eines angeblasenen geheizten Zylinders," *Forsch. Arb. Ing.-Wes.*, Vol 12, pp. 63-75

- Sengupta, S., Sherif, S.A., and Wong, K.V., 1998, "Empirical Heat Transfer and Frost Thickness Correlations During Frost Deposition on a Cylinder in Cross Flow in the Transient Regime," *International Journal of Energy Research*, Vol. 22, No. 7, June, pp. 615-624.
- Sherif, S.A., 1991, "Theory of Frost Formation," *Proceedings of the 32nd Heat Transfer and Fluid Mechanics Institute*, F.H. Reardon and N.D. Thinh (editors), School of Engineering and Computer Science, California State University Press, Sacramento, California, pp. 239-252.
- Sherif, S.A., Al-Mutawa, N.K., Mathur, G.D., Steadham, J.M., Tiedeman, J.S., MacFarlane, S., Urlaub, J., West, J., and Harker, R.A., 1997, "A Study to Determine Heat Loads Due to Coil Defrosting," Final Technical Report No. UFME/SEECL-9701, Contract No. ASHRAE-622-RP, the American Society of Heating, Refrigerating and Air-Conditioning Engineers, Atlanta, Georgia, January.
- Sherif, S.A., Mago, P.J., Al-Mutawa, N.K., Theen, R.S., and Bilen, K., 2001, "Psychrometrics in the Supersaturated Frost Zone," *ASHRAE Transactions*, Vol. 107, Part 2, June, pp. 753-767.
- Sherif, S.A., Mago, P.J., and Theen, R.S., 2002, "A Study to Determine Heat Loads Due to Coil Defrosting – Phase II," Final Technical Report No. UFME/SEECL-200201, Contract No. ASHRAE-1094-RP, the American Society of Heating, Refrigerating and Air-Conditioning Engineers, Atlanta, Georgia, February.
- Sherif, S.A., Raju, S.P., Padki, M.M., and Chan, A.B., 1993, "A Semi-Empirical Transient Method for Modelling Frost Formation on a Flat Plate," *International Journal of Refrigeration*, Vol. 16, No. 5, September, pp. 321-329.
- Smith, G.R., 1989, "Theoretical Cooling Coil Calculations at Freezer Temperatures to Avoid Unfavorable Coil-Frost," *ASHRAE Transactions*, Vol. 95, Part 2, June, pp. 1138-1148.
- Smith, G.R., 1992, "Latent Heat, Equipment-Related Load, and Applied Psychrometrics at Freezer Temperatures," *ASHRAE Transactions*, Vol. 98, Part 2, Paper No. BA-92-11-1, June, pp. 649-657.
- Stewart, R.B., Jacobsen, R.T., and Becker, J.H., 1983, "Formulations for Thermodynamic Properties of Moist Air at Low Pressures as Used for Construction of New ASHRAE SI Unit Psychrometric Charts," *ASHRAE Transactions*, Vol. 89, Part 2A, pp. 536-548.
- Stoecker, W.F., 1960, "Frost Formation on Refrigeration Coils," *ASHRAE Transactions*, Vol. 66, Part 1, February, pp. 91-103.

- Stoecker, W.F., Lux, J.J., and Kooy, R.J., 1983, "Energy Considerations in Hot-Gas Defrosting of Industrial Refrigeration Coils," *ASHRAE Transactions*, Vol. 89, Part 2, pp. 549-573
- Tao, Y.X., Mao, Y., and Bessant, R.W., 1994, "Frost Growth Characteristics on Heat Exchanger Surfaces: Measurement and Simulation Studies," *Fundamentals of Phase Change: Sublimation and Solidification American Society of Mechanical Engineers*, Heat Transfer Division, (Publication) HTD v 286 1994, New York, NY, pp. 29-38
- White, J.E. and Cremers, C.J., 1974, "Predictions of Growth Parameters of Frost Deposits in Forced Convection," AIAA Paper 74-746.
- Yonko, J.D. and Sepsy, C.F., 1967, "An Investigation of the Thermal Conductivity of Frost While Forming on a Flat Horizontal Plate," *ASHRAE Transactions*, Vol. 73, Part 2, June, Paper No. 2043, pp. I.1.1- 11.

BIOGRAPHICAL SKETCH

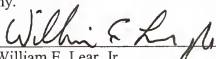
Pedro Mago was born on April 23, 1975, in Boston, Massachusetts. When he was a child, he and his family moved to Venezuela. He began his engineering studies at the Universidad de Oriente in Puerto La Cruz, Venezuela, in 1991, obtaining his bachelor's degree in mechanical engineering in June 1996. That same year, he accepted a full-time position as faculty at the Universidad de Oriente (UDO) in the Department of Mechanical Engineering. In January 1999, Pedro moved to Gainesville and started his master's degree at the University of Florida. In May 2000, he completed his Master of Science degree in mechanical engineering, specializing in thermal science; and began his Ph.D. program in the same department. In August 2003, he completed his graduate studies at the University of Florida.

I certify that I have read this study and that in my opinion it conforms to acceptable standards of scholarly presentation and is fully adequate, in scope and quality, as a dissertation for the degree of Doctor of Philosophy.



S. A. Sherif, Chairman
Professor of Mechanical and
Aerospace Engineering

I certify that I have read this study and that in my opinion it conforms to acceptable standards of scholarly presentation and is fully adequate, in scope and quality, as a dissertation for the degree of Doctor of Philosophy.



William E. Lear, Jr.
Associate Professor of Mechanical
and Aerospace Engineering

I certify that I have read this study and that in my opinion it conforms to acceptable standards of scholarly presentation and is fully adequate, in scope and quality, as a dissertation for the degree of Doctor of Philosophy.



Jacob N. Chung
Eminent Scholar of Mechanical and
Aerospace Engineering

I certify that I have read this study and that in my opinion it conforms to acceptable standards of scholarly presentation and is fully adequate, in scope and quality, as a dissertation for the degree of Doctor of Philosophy.



Herbert A. Ingley, III
Associate Professor of Mechanical
and Aerospace Engineering


I certify that I have read this study and that in my opinion it conforms to acceptable standards of scholarly presentation and is fully adequate, in scope and quality, as a dissertation for the degree of Doctor of Philosophy.



C. Direlle Baird
Professor of Agricultural and
Biological Engineering

This dissertation was submitted to the Graduate Faculty of the College of Engineering and to the Graduate School and was accepted as partial fulfillment of the requirements for the degree of Doctor of Philosophy.

August 2003



Pramod P. Khargonekar
Dean, College of Engineering

Winfred M. Phillips
Dean, Graduate School